Effects of Grain Boundary Structure on Diffusion Along [001] Tilt Boundaries in the Au/Ag System

by

Qing Ma

Submitted to the Department of Physics
in partial fulfillment of the requirements for the degree of

Doctor of Philosophy

at the

MASSACHUSETTS INSTITUTE OF TECHNOLOGY

September 1991

Author ....
Department of Physics
August 9, 1991

Certified by ....
Robert W. Balluffi
Professor of Physical Metallurgy
Thesis Supervisor

Accepted by ....
George F. Koster
Chairman, Departmental Committee on Graduate Students

Effects of Grain Boundary Structure on Diffusion Along [001] Tilt Boundaries in the Au/Ag System

by

Qing Ma

Submitted to the Department of Physics
on August 9, 1991, in partial fulfillment of the
requirements for the degree of
Doctor of Philosophy

Abstract

The effects of grain boundary structure on grain boundary diffusion in the Au/Ag system were investigated both experimentally and theoretically.

A new experimental method, called multi-crystal surface accumulation method was developed for this study. In this method, lattice diffusion was frozen out, and during the diffusion annealing the Ag atoms diffused through thin film specimens along transverse grain boundaries from the source surface to the accumulation surface. All transverse boundaries were of the same type. This method enabled measurements of grain boundary diffusivities with a high degree of consistency at low temperatures ($T < \frac{1}{3}T_m$), and therefore made it possible, for the first time, to study structural effects in the type-C kinetics regime. The method was also capable of eliminating possible chemical effects on diffusion due to grain boundary segregation and diffusion induced grain boundary migration.

Grain boundary diffusivities were measured for a series of symmetric [001] tilt boundaries with 16 different structures including CSL boundaries of low-Σ (i.e., 5, 13, 17, 25) and more general boundaries with tilt angles between the low-Σ misorientations. The diffusivities were found to vary monotonically with tilt angle and could be rather satisfactorily fitted with a Structural Unit model description with delimiting boundaries: $\Sigma 1\,(100)$, $\Sigma 17\,(410)$, $\Sigma 5\,(310)$, $\Sigma 5\,(210)$, $\Sigma 13\,(320)$ and $\Sigma 1\,(110)$. The absence of cusps at the low-Σ misorientations suggests that the effect of the elastic field produced by the secondary dislocations on the grain boundary core structure is weak. It was also suggested that previous observations of deep cusps in $s_b\delta_b D_b$ curves at low-Σ misorientations may have been due to grain boundary segregation or DIGM effects. The temperature dependence of measured grain boundary diffusivities gave well defined activation energies of $\sim 0.7-0.85$ eV, which were smaller than the average value of ~ 1.0 eV, obtained at high temperatures in previous studies. Correspondingly, the measured pre-exponential factors (i.e., $\delta_b D_b^0$ values) were ~ 3 orders of magnitude smaller than those obtained at high temperatures. Both Arrhenius parameters were found to be smooth functions of tilt angle.

Four representative grain boundaries: $\Sigma 5\,(310)$, $\Sigma 13\,(510)$, $\Sigma 5\,(210)$ and $\Sigma 13\,(320)$

were selected for computer simulation study. The interstitialcy mechanism was found to be of considerably lower activation energy than the vacancy mechanism in all of the 4 boundaries. The agreement in activation energy between the calculated values for the interstitialcy mechanism and the measured values was excellent for 3 of the 4 boundaries: $\Sigma 5\,(310)$, $\Sigma 5\,(210)$ and $\Sigma 13\,(320)$. Calculated results also indicated that the low activation energy atomic jumping paths were of the same type for the 4 boundaries and were contained within the structural units associated with the Structural Unit model.

Studies of correlated diffusional walks by computer simulation in both idealized and realistic grain boundaries revealed that there exist several possible confinements for a correlated walk, corresponding to different effective dimensionalities of the diffusion paths. By using the calculated correlation factors and simple kinetic theory, the $\delta_b D_b^0$'s were estimated for the 4 representative boundaries. Excellent agreement was found between the measured $\delta_b D_b^0$'s and the estimates with respect to both the general magnitude and the trend of the structural dependence. The results also suggested that the effective grain boundary width for grain boundary diffusion at low temperatures is close to the average interatomic distance. To explain the large difference in magnitude between the $\delta_b D_b^0$'s measured at relatively low and high temperatures, and in fact, the overall upward curvature found in the Arrhenius diagram, possible effects due to anharmonicity of atomic interaction and additional diffusion mechanisms associated with multiple boundary defects were suggested as possible reasons.

Thesis Supervisor: Robert W. Balluffi
Title: Professor of Physical Metallurgy

Acknowledgments

I would like to express my deepest gratitude to Professor Robert W. Balluffi for his support, guidance and encouragement as my thesis supervisor. He has made the course of research a challenging and rewarding one, and has greatly influenced my intellectual development. I am also deeply moved by his kindness. He always had time to listen and discuss, with genuine interest and extraordinary patience.

I am thankful to Professor Mildred S. Dresselhaus and Professor Rainer Weiss for their enlightening suggestions and the special efforts they made when serving on my thesis committee.

Over the years, I have received numerous help, advice and encouragement from many people. Some of them are Professor Gretchen Kalonji, Dr. Paul Bristowe, Dr. Imtiaz Majid, Dr. T.E. Hsieh, Dr. Thomas Ferrence, Dr. Abbas Amiri-Hezaveh, Dr. Craig Counterman, Dr. L.Q. Chen, Barbara Rich, Sandy Ung, and technical staff members at CMSE Surface Analysis Center Facility and Submicron Structures Laboratory at MIT. To all of them, I am deeply indebted.

Great love and support have been provided by my family, especially my father who brought me up single-handedly. His expectation has been a continuous source of motivation. Thanks go to my brother for the countless help and constant encouragement, and for being a role model. To them, I am dedicating this thesis.

Finally, I would like to thank my wife, Wei, for her emotional support and understanding and many more. Without her love, it would have been much more difficult to endure the many frustrations encountered, and without her sharing the experience, it would have been much less enjoyable to reach the completion of this thesis.

Contents

List of Figures

List of Tables

Chapter 1

Introduction

In a polycrystalline material, solute atoms generally diffuse much more rapidly along the grain boundaries than through the crystal lattice at temperatures appreciably below the melting point. Consequently, grain boundary diffusion often plays key a role in a host of technologically important processes involving materials transport. For example, diffusional "short circuiting" of foreign solute atoms along transverse grain boundaries in layered electronic devices can destroy the performance of the devices, while the stress motivated diffusional transport of atoms along grain boundaries in fine-grained materials can produce substantial diffusional creep. A knowledge of the grain boundary diffusion characteristics is thus essential for understanding various grain boundary diffusion controlled physical processes as well as optimizing design parameters and processing conditions for various applications.

In the great majority of practical situations where grain boundary diffusion is important, there is a wide range of different types of grain boundaries involved, and hence the overall diffusion behavior is very complicated. It is necessary, therefore, to study the diffusion properties of geometrically well defined boundaries in order to establish a link between their diffusional and structural characteristics and to understand the basic mechanisms responsible for the diffusion process.

During the last few decades, a number of studies have been made of the effects of grain boundary structure on grain boundary diffusion properties [1]. Although the

$\sin \theta^1/2$-dependence of diffusivity stands more or less verified for low angle ($\theta \lesssim 15°$) tilt boundaries, whose structure can be described by an array of discrete lattice dislocations, the establishment of rules that govern high angle boundaries have yet to be achieved.

More recently, Balluffi and Brokman [2] proposed a model which provides a description of the dependence of the grain boundary diffusivity on the grain boundary core structure for a series of symmetric tilt boundaries. This model, called the Structural Unit model for grain boundary diffusion[2], reduces to the simple dislocation model at the low angle limit. One of the basic characteristics of grain boundary diffusion behavior, according to the Structural Unit model, is that the grain boundary diffusivity varies continuously as the structural parameters change gradually. As a result, by using this model, the diffusivity of all boundaries in a tilt boundary series can be estimated from a knowledge of the diffusivity of a few geometrically special boundaries (low-Σ[3] short-period boundaries) in the same series.

Experiments aimed at studying the structural dependence of grain boundary diffusion have not alway confirmed the Structural Unit model. One of the current issues is the possible existence of cusps in the grain boundary diffusion parameter, $\delta_b D_b$, versus misorientation angle, θ, curves for [001] tilt boundaries at special misorientations corresponding to low-Σ short-period boundaries[4]. Several measurements [6, 7] of the lumped chemical grain boundary diffusion parameter, $s_b \delta_b D_b$, versus misorientation angle have shown deep cusps at the special misorientations, which can not be satisfactorily explained by the Structural Unit model if these cusps result from the variation in $\delta_b D_b$. However, the grain boundary segregation factor s_b, which is known to depend on grain boundary structure [8], may have been responsible for the observed cusps.

Unfortunately, by using the traditional bicrystal profiling method in studying

---

[1] Here, θ is the misorientation angle of the grain boundary.

[2] It is so named because it is based on the Structural Unit model for grain boundary core structures [3, 4, 5].

[3] See Section 2.1.1.

[4] Here, D_b is the grain boundary diffusivity, and δ_b is the effective grain boundary width.

structural effects, it is impossible to eliminate or to take into account grain boundary segregation effects and other possible chemical effects. Besides this deficiency, the bicrystal method relies on the leakage of diffusant from the boundary into the lattice and therefore can only be employed in the high temperature region ($T > \frac{1}{3}T_m$).

Ideally, however, it is advantageous to study grain boundary diffusion at relatively low temperatures ($T < \frac{1}{3}T_m$), because the behavior of grain boundary diffusion at low temperatures is generally more amenable to simple physical interpretation. For example, multiple diffusion mechanisms may be operative at relatively high temperatures, which would be difficult to interpret at this stage of our knowledge.

Indeed, current knowledge of the grain boundary diffusion mechanism is still in its infancy. Within the limited number of studies on this subject [1], most of them seem to support the vacancy mechanism. However, the experimental evidence for the vacancy mechanism is not sufficient. The most direct evidence of a vacancy mechanism emerges from the computer simulation studies of Balluffi and co-workers [9, 10]. These studies, however, are limited to grain boundaries in BCC iron and therefore do not necessarily reflect the grain boundary diffusion mechanism in other systems, such as FCC metals.

This work is therefore motivated to improve the general understanding of grain boundary diffusion, especially the effects of grain boundary structure on grain boundary diffusion in the high-angle region, by performing measurements and calculations of the diffusivity for a series of geometrically well defined grain boundaries. The measured results will be used to assess the extent of validity of the Structural Unit model, and to determine whether or not the low-Σ short-period boundaries have any special diffusion properties. They will also be compared with the calculated results to provide us insights into the grain boundary diffusion mechanism and kinetics, and structural effects at the atomic level. These results should also allow us to clarify some related questions including the origin of observed cusps in chemical diffusion systems, the validity of some experimental methods used in grain boundary diffusion mechanism determinations, the magnitude of the effective grain boundary width, and the differences between measured diffusion results in different temperature regions.

The measurements are conducted at relatively low temperatures so that unique information regarding grain boundary diffusion can be obtained and interpreted using simple physics. Calculations are performed at $T = 0$ K to simulate the low temperature behavior.

Efforts are made to develop a new experimental method in order to incorporate the features of controllability of the grain boundary structure and sensitivity to grain boundary diffusion at low temperatures. This method should also be capable of eliminating any influential chemical effects, such as effects due to grain boundary segregation and diffusion induced grain boundary migration, and therefore improve the reliability of measurements so that more conclusive results can be obtained.

Chapter 2

Background

2.1 Grain Boundary Structure

A grain boundary is the transition region between two misoriented crystals of the same kind, and it is almost certain now that most (and probably all) grain boundaries possess ordered structures. To effectively describe these ordered structures, models have been developed, including the Coincidence Site Lattice (CSL) model [11, 12] and the Structural Unit (SU) model [13]. While the CSL model provides a geometrical framework in which some special CSL boundaries are of central importance and other more general boundaries are described as deviations from the special CSL boundaries by introducing grain boundary dislocations (GBDs), the SU model offers a continuous description of the atomistic core structures of a series of grain boundaries with intermediate misorientations between those of two special boundaries termed "delimiting" boundaries.

2.1.1 Coincidence Site Lattice Model

The CSL model can be illustrated through the following imaginary process for the construction of a bicrystal with a planar boundary. First, two rigid lattices made up of "black" and "white" atoms, respectively, are allowed to interpenetrate each other and are then aligned perfectly so that all sites of one lattice coincide with those of the other lattice. Then one lattice is rotated relative to the other around a common origin into the desired misorientation for the grain boundary to form the "dichromatic pattern (DCP)" as shown in Fig. 2-1a. For certain misorientations[1], a significant fraction of the lattice sites in the DCP may coincide again to define a superlattice, i.e., the Coincidence Site Lattice. In the next step, a bicrystal is produced by passing a plane with the desired inclination and position through the DCP and discarding all black atoms on one side of the plane and all white atoms on the other. The resulting grain boundary (Fig. 2-1b) has the period of the corresponding plane in the CSL. Finally, the bicrystal system is allowed to relax to a configuration of minimum energy. In this step, the atoms in the core will adjust their positions and the two lattices may translate relatively by a rigid body translation. This translation does not change the periodicity of the boundary.

A quantity Σ, often used to describe the CSL, is defined as the reciprocal of the fraction of lattice points in coincidence. For example, $\Sigma = 5$ for the CSL shown in Fig. 2-1a. Geometrically, Σ reflects the degree of match between the two lattices at the boundary. There is considerable evidence that boundaries corresponding to a short period (low-Σ) CSL and parallel to a relatively dense plane of the CSL are often of local minimum energy with respect to misorientation and inclination angles. (These special boundaries will be called "low-Σ " boundaries from now on.) Consequently, when there is any small deviation from the minimum energy geometry, the boundary minimizes its energy by preserving patches of the low-Σ boundary and introducing an array of grain boundary dislocations (GBDs), which accommodates the differences in misorientation or inclination between the exact low-Σ boundary and the actual boundary. Since the boundary structure on both sides of the dislocation is preserved, the Burgers vector of the GBDs has to be a translation that preserves the DCP. The collection of all such vectors forms a sublattice of the CSL, called the DSC[2]-Lattice (see Fig. 2-1b). In general, the boundary selects relatively small vectors of the DSC-

---

[1] It is always possible to find a CSL corresponding to a misorientation which is arbitrarily close to the actual misorientation of the two lattices. However, only those CSLs with reasonably short period have physical significance.

[2] The DSC-Lattice is so named because it is the lattice of pattern conserving displacements, i.e., a *displacement* of Lattice 2 with respect to Lattice 1 by a DSC-Lattice vector causes a pattern *shift* which is *complete*[14].

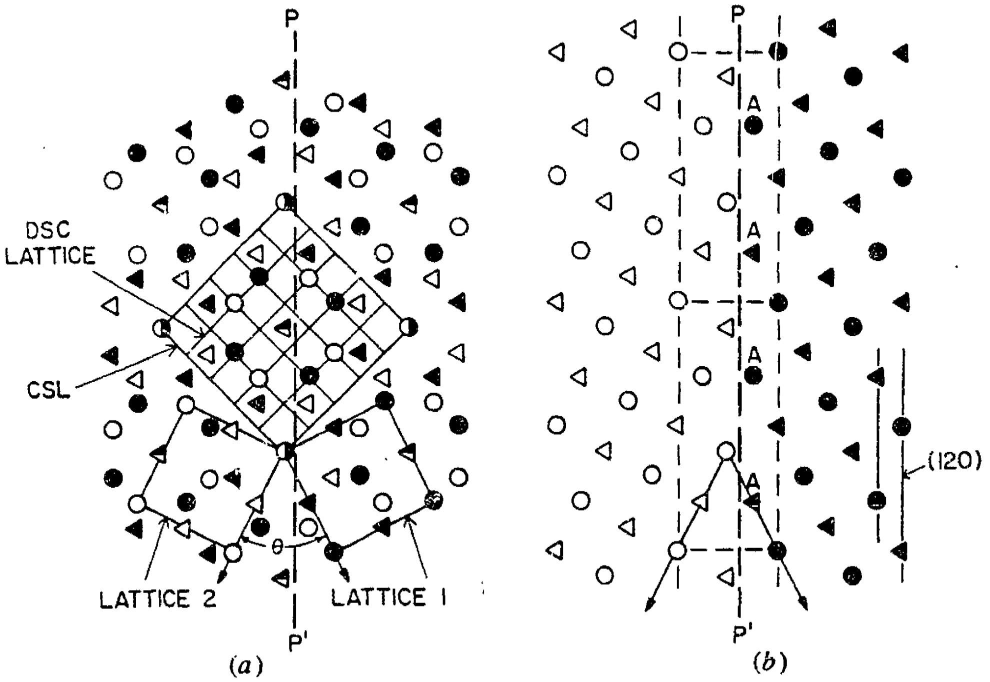

Figure 2-1: (a) DCP, CSL, and DSC-L formed by rotating one FCC crystal with respect to another around [001] by $\theta = 53.1°$. Structures are viewed along [001]. Different symbols indicate atoms in the two crystal lattices which possess ABAB... stacking along [001]. (b) Rigid bicrystal containing grain boundary along PP' obtained from structure in (a) by discarding appropriate atoms from both sides of PP'.

Lattice for Burgers vectors in order to reduce the strain energy of the elastic field produced by the GBD array.

As a special case, a low angle boundary, consisting of an array of dislocations with Burgers vector determined by the primitive crystal lattice translation vector, could also be described by the CSL model. For example, consider a low angle symmetric [001] tilt grain boundary in a FCC crystal. Start with the two perfectly aligned crystal lattices as usual, but let the rotation angle be zero. Then we have CSL = DSC-L = FCC-L and $\Sigma = 1$.

Now choose the (110) plane to be the grain boundary plane to produce an imaginary "grain boundary" in a single crystal. Then we introduce a small deviation which increases the misorientation from zero to a small angle. The boundary minimizes its energy by preserving patches of the low-Σ boundary which is the perfect lattice in this case, and introducing an array of grain boundary dislocations. Since the DSC-L is the same as the FCC crystal lattice, the Burgers vector equals the primitive translation vector:

$$b = \frac{a}{\sqrt{2}} \, ,$$

where a is the lattice constant. We now make a distinction and call these dislocations "primary" grain boundary dislocations (PGBDs), and those with Burgers vectors determined by DSC-L's of $\Sigma > 1$ "secondary" grain boundary dislocations (SGBDs). The spacing between the primary dislocations is given by Franks formula:

$$d_p = \frac{b}{2 \sin \theta/2} \, . \qquad (2.1)$$

Obviously, when the misorientation increases, the spacing decreases. Eventually, d_p becomes so small that the dislocation cores start to overlap and the primary dislocation model based on $\Sigma = 1$ CSL loses its validity.

Experimental measurements [15, 16] and computer simulation results [17, 18] of grain boundary energy show that the primary dislocation description is adequate for $\theta \lesssim 15°$. Therefore, boundaries with misorientation angles less than 15° are called "low angle" boundaries. Fortunately, low-Σ boundaries are more or less evenly distributed in the high angle regions, so that for a specific boundary, a SGBD model based on one of the low-Σ boundaries can usually be used. It is noticed that although the primary dislocations lose their identity physically when the misorientation becomes large, they still exist geometrically. With a [001] rotation axis, for a specific DCP consisting of two FCC lattices, the CSL and DSC-L vectors in the (001) plane are given by

$$x^{CSL} = \sqrt{\Sigma}\,\frac{a}{\sqrt{2}} ,$$

and

$$x^{DSC} = \frac{1}{\sqrt{\Sigma}}\,\frac{a}{\sqrt{2}} ,$$

respectively.

Similarly, the secondary dislocation spacing can be expressed as

$$d_s = \frac{b_s}{2\sin\Delta\theta/2} , \tag{2.2}$$

where $\Delta\theta$ is the deviation from the exact CSL misorientation. For the symmetric [001] tilt boundaries, the Burgers vectors of the SGBDs are

$$b_s = \begin{cases} \sqrt{2}x^{DSC} = \frac{a}{\sqrt{\Sigma}} & 0^\circ \le \theta \le 45^\circ \ ; \\ x^{DSC} = \frac{1}{\sqrt{\Sigma}}\frac{a}{\sqrt{2}} & 45^\circ < \theta \le 90^\circ \ . \end{cases}$$

Therefore, from Eq. 2.2, we have

$$d_s = \sim \frac{a}{\sqrt{\Sigma}}/\Delta\theta \ .$$

Since the spacing has to be large enough to avoid core overlapping, for a lower Σ value, the SGBD model covers a larger range of misorientation deviation.

The reason that low-Σ boundaries are of special significance is that they have relatively deep minima energies (energy cusps) so that a boundary with even an appreciable deviation can still relax to a SGBD configuration. With the above geometrical background, we can provide an approximate analysis of the energy cusps.

Assume that the elastic fields are restricted to cylinders of radius $d_s/2$ around each SGBD core and are the same as the field around an isolated dislocation. The elastic strain energy stored in a cylinder of radius $d_s/2$ around an edge dislocation is [19]

$$E = \frac{\mu b_s^2}{4\pi(1-\nu)} \ln\left(\frac{\alpha d_s}{2b_s}\right) , \tag{2.3}$$

where μ is the shear modulus, ν is the Poisson's ratio and $\alpha = b_s/r_0$, where r_0 is the dislocation core size.

So the extra grain boundary energy caused by the SGBDs is

$$\Delta\gamma_b = E/d_s \approx \frac{\mu b_s^2}{4\pi(1-\nu)} \left(\frac{\Delta\theta}{b_s}\right) \ln\left(\frac{\alpha}{2\Delta\theta}\right) , \tag{2.4}$$

which is cusped at $\Delta\theta = 0°$. We also see that $\Delta\gamma_b \sim b_s \sim 1/\sqrt{\Sigma}$, or the cusps are deeper for the boundaries of lower Σ values, which provides the physical basis for the CSL model and the following SU model.

2.1.2 Structural Unit Model

By using a molecular statics method, Sutton and Vitek [3, 4, 5] found that the core structures of certain low-Σ tilt boundaries can be considered to be composed of a uniform array of a single type of "structural unit"[3]. These boundaries, termed "favored" boundaries, are relatively uniform in structure and consist of a continuous sequence of primary dislocations whose long range elastic stress fields cancel almost exactly. All other boundaries in the series which possess misorientations that are intermediate between those of the favored boundaries have structures which can be considered to be mixtures of the units making up the two nearest favored boundaries. These two favored boundaries are called "delimiting" boundaries because they delimit the range of misorientations in which this particular structural unit decomposition occurs.

Although the SU model focuses on the grain boundary core atomic arrangement,

---

[3] A structural unit is defined as a small group of atoms arranged in a characteristic configuration.

it is completely consistent with the previously described CSL model. In the case of intermediate boundaries between two delimiting boundaries consisting of all A type units and all B type units, respectively, the structure of boundaries near an A type delimiting boundary consists of a minority of B type units embedded in an A type unit background. It can be proven geometrically that the minority units directly correspond to the cores of SGBDs in the CSL model, with a Burgers vector belonging to the DSC-lattice of the A type delimiting boundary. Further, at some particular intermediate misorientations, boundaries can be composed of a regular mixing of units, e.g., ...$ABABAB$.... These boundaries are also low-Σ boundaries with relatively low energy and relatively free of long range stress field. A boundary near such a misorientation consists mainly of the regular sequence of structural units with perturbation which can also be described as SGBDs. For example, the boundary ...$ABABBABABB$... can be considered as the boundary ...AB... perturbed by additional B units, which correspond to the cores of the SGBD with Burgers vector belonging to the DSC-L of boundary ...AB....

Fig. 2-2 shows an example of such a series of boundaries, in which the $\Sigma 1$ and $\Sigma 5$ boundaries are the delimiting boundaries consisting of single type of structural units A and B respectively, and $\Sigma 41$ and $\Sigma 17$ with intermediate misorientations are composed of mixtures of these units.

It is also found that the boundary structures vary continuously with misorientation in both the unit composition ratio and the sequential ordering. This result enables one to predict the core structure of any intermediate boundary given the structures of the delimiting boundaries. For example, the period vectors for $\Sigma 1\,(A)$ and $\Sigma 5\,(B)$ boundaries are (in the coordinates of crystal-1):

$$\lambda_A = \frac{1}{2}[\bar{1},1] \, ,$$

$$\lambda_B = \frac{1}{2}[\bar{1},2] \, ,$$

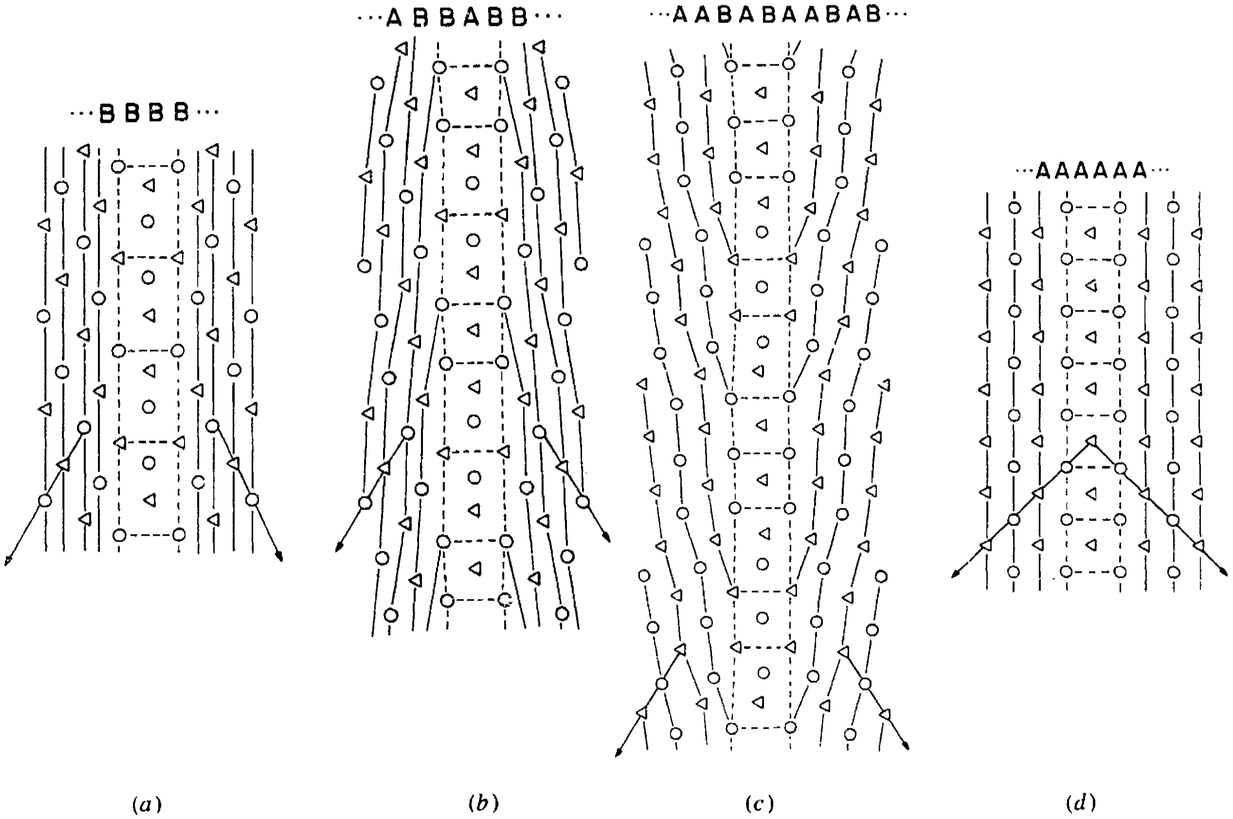

Figure 2-2: Relaxed structures of a series of symmetric [001] tilt boundaries, after Sutton and Vitek [3]. (a) $\Sigma = 5\,(53.1^\circ)$ boundary; (b) $\Sigma = 17\,(61.9^\circ)$ boundary; (c) $\Sigma = 37\,(71.1^\circ)$ boundary; (d) $\Sigma = 1\,(90^\circ)$ "boundary".

and that of $\Sigma 41$ is

$$\lambda_C = \frac{1}{2}[\bar{4}, 5] = 3\lambda_A + \lambda_B \ .$$

So the composition ratio is $A : B = 3 : 1$, and the sequential ordering can only be $...AAAB...$.

The continuity of composition ratio says that when the misorientation angle θ changes from 0° to 36.9°, the ratio $A : B$ changes continuously from 1 to 0, which is quite straight forward. However, the idea of the continuity of sequential ordering is more difficult to state explicitly, although it is apparent in specific situations. For instance, a boundary of ratio $A : B = 3 : 2$ is between two other boundaries having the ratio 2 : 1 and 1 : 1 according to the ratio continuity, for which the sequences are unique:

$$2:1 \qquad ...AAB... \ ;$$

$$1:1 \qquad ...AB... \ .$$

But for the 3 : 2 boundary, there are two possibilities:

$$...AABAB... \ ;$$

and

$$...AAABB... \ .$$

The requirement of sequential continuity selects the first one since it is the sequence that between $...AAB...$ and $...AB...$, and the second possibility $...AAABB...$ contains $...AAA...$ and $...BB...$ which should only appear on the other sides of $...AAB...$ or $...AB...$ respectively.

The SU model provides information about grain boundary core structures. Therefore, it should be useful in describing properties that are determined by the grain boundary cores, such as grain boundary diffusion. Balluffi and Brokman [2] suggested a simple model that predicts the diffusivity of intermediate boundaries providing that the diffusivities of the two delimiting boundaries $...A...$ and $...B...$ and of the intermediate boundary $...AB...$ are known.

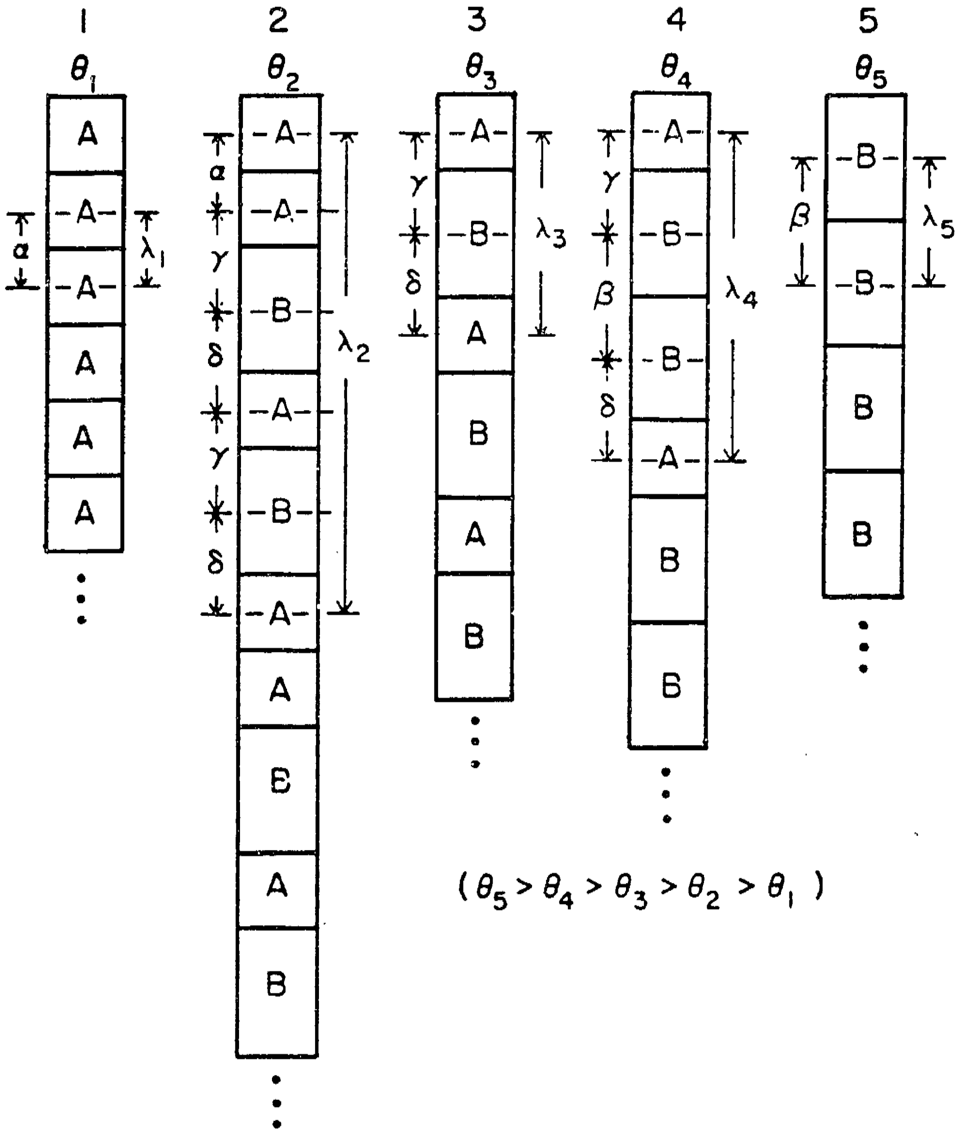

Figure 2-3: Schematic representation of the SU model of a series of symmetric tilt boundaries, after Balluffi and Brokman [2]. Boundaries 1 and 5 are the delimiting boundaries made up of all *A* units and *B* units, respectively. Boundaries 2, 3 and 4 are boundaries of intermediate misorientations and are composed of various mixtures of *A* and *B* units. Structures are viewed along the tilt axis.

Denote the grain boundary diffusion parameter $\delta_b D_b$ as P. For the boundaries in Fig. 2-3, we have

$$
\begin{aligned}
P_1 &= \frac{1}{\lambda_1}[D^\alpha A^\alpha] , \\
P_2 &= \frac{1}{\lambda_2}[D^\alpha A^\alpha + 2(D^\gamma A^\gamma + D^\delta A^\delta)] , \\
P_3 &= \frac{1}{\lambda_3}[D^\gamma A^\gamma + D^\delta A^\delta] , \\
P_4 &= \frac{1}{\lambda_4}[D^\gamma A^\gamma + D^\beta A^\beta + D^\delta A^\delta] , \\
P_5 &= \frac{1}{\lambda_5}[D^\beta A^\beta] ,
\end{aligned}
\tag{2.5}
$$

where D^j and A^j are the diffusivity and area of the j-type patch respectively. Note that it is necessary to employ four different types of patches in order to take into account the local regions where different structural units are joined together. Clearly, P_2 and P_4 can be expressed as linear combinations of P_1 and P_3, and P_3 and P_5 respectively:

$$P_2 = \frac{1}{\lambda_2}(\lambda_1 P_1 + 2\lambda_3 P_3) , \tag{2.6}$$

$$P_4 = \frac{1}{\lambda_4}(\lambda_3 P_3 + \lambda_5 P_5) . \tag{2.7}$$

More generally, following the continuity requirement discussed earlier, it can be proven that the diffusion parameters for all boundaries in the misorientation range between the 1 and 3 (or 3 and 5) boundaries can be expressed as linear combinations of P_1 and P_3 (or P_3 and P_5).

2.2 Grain Boundary Diffusion Basics

2.2.1 Slab Model

There are generally two approaches for the theoretical treatment of diffusion problems in a crystal lattice: the atomistic approach and the continuum approach. The former approach, considers the atomic nature of the diffusion substance explicitly and requires a full knowledge of the crystal structure, while the latter treats the diffusion substance as a continuous medium and the atomic nature of the diffusion is ignored. Since the grain boundary structures are very complicated and in most cases unknown, it is often practically impossible to provide an atomistic description for a given system. Consequently, experimental results in grain boundary studies are usually analyzed and presented utilizing a continuum approach.

It is generally accepted that the grain boundary diffusion occurs only in the boundary core region, which contains the "bad material" with a highly disturbed structure. As discussed in the Section 2.1.2, the different sites in the grain boundary are generally inequivalent, therefore the local atomic jumping frequency varies from site to site. However, in the vast majority of cases of interest, the diffusion distance is much larger than either the grain boundary width or the two dimensional periods in the grain boundary plane so that any measured diffusion results will be an average over all of the sites; thus, they can be described by using a continuum model.

Fisher [20] first established such a mathematical model in which the grain boundary is replaced by an isotropic slab of effective width δ_b possessing a high effective average diffusivity D_b, embedded in a semi-infinite perfect crystal of a low diffusivity D_l, normal to the surface that carries the diffusant. Let us take the y-axis normal to the grain boundary slab and the z-axis normal to the free surface, so that the yx-plane is a symmetry plane, the equations for diffusion inside and outside of the grain boundary slab are given by Fick's second law:

$$\frac{\partial C_b(y,z,t)}{\partial t} = D_b\left(\frac{\partial^2 C_b}{\partial y^2} + \frac{\partial^2 C_b}{\partial y^2}\right) \qquad |y| \leq \frac{\delta_b}{2}\,, \tag{2.8}$$

$$\frac{\partial C_l(y,z,t)}{\partial t} = D_l\left(\frac{\partial^2 C_l}{\partial y^2} + \frac{\partial^2 C_l}{\partial y^2}\right) \qquad |y| > \frac{\delta_b}{2}\,, \tag{2.9}$$

where C_b and C_l are the diffusant concentrations in the grain boundary and lattice respectively and t is the annealing time.

The requirement that both the diffusant concentration and flux are continuous at

$y = \pm\delta_b/2$ gives the boundary conditions:

$$C_b(\pm\delta_b/2, z, t) = C_l(\pm\delta_b/2, z, t) \; , \tag{2.10}$$

$$D_b \frac{\partial C_b}{\partial y}|_{|y|=\delta_b/2} = D_l \frac{\partial C_l}{\partial y}|_{|y|=\delta_b/2} \; . \tag{2.11}$$

The above equations form the mathematical basis of the slab model and their solutions for various situations have been obtained, some of which will be discussed in Section 2.2.3.

2.2.2 Diffusion Kinetics Regimes

In polycrystals, lattice and grain boundary diffusion occurs simultaneously. According to Harrison [21], there are generally three kinetics regimes A, B and C as shown in Fig. 2-4. Type-A kinetics, which include extensive lattice diffusion together with grain boundary diffusion, are generally important at relatively high temperatures ($T > 0.5T_m$). As shown in Fig. 2-4a, the diffusion kinetics resemble those of lattice diffusion with a nearly flat diffusion front.

When the temperature is lowered, lattice diffusion slows down much more rapidly than the boundary diffusion because the activation energy for lattice diffusion is much larger. In the type-B kinetics regime ($0.3T_m < T < 0.5T_m$), individual boundaries are isolated and fast diffusion along the grain boundaries is accompanied by leakage of the diffusant into the grains as illustrated in Fig. 2-4b. At even lower temperatures ($T < 0.3T_m$), type-C diffusion kinetics are operative (Fig. 2-4c). The lattice diffusion is now frozen out so that only grain boundary diffusion is significant.

It is noted that although the grain boundary diffusion kinetics are closely related to the temperature, the correspondence between a kinetics regime and a certain temperature range mentioned above is not always followed. As illustrated in Fig. 2-4, the

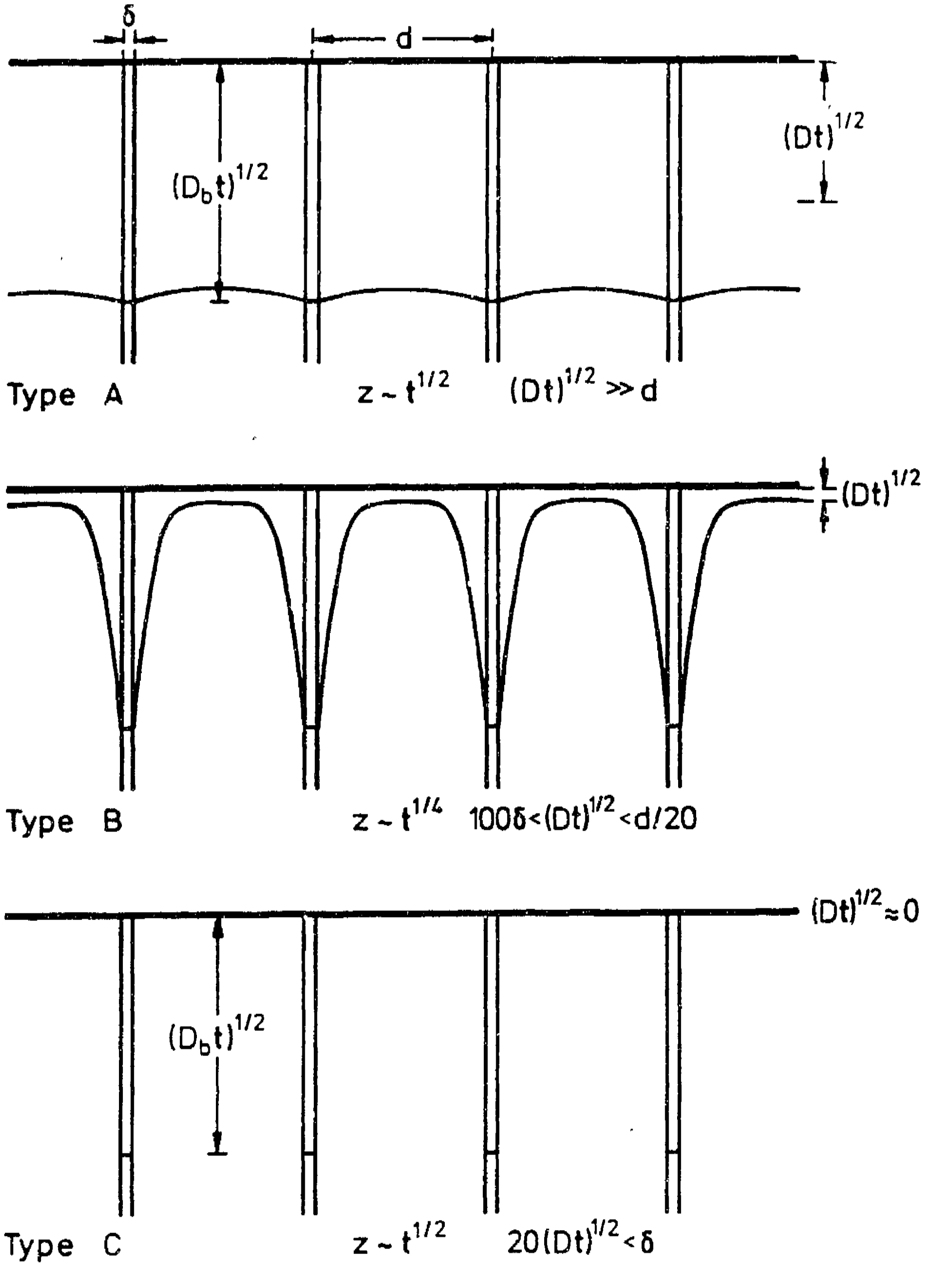

Figure 2-4: Schematic illustration of type-A, B and C diffusion kinetics regimes.

requirements for the three kinetics regimes are:

$$\begin{array}{ll} \text{A} & \sqrt{D_l t} \gg d \; ; \\ \text{B} & \delta_b \ll \sqrt{D_l t} \ll d \; ; \\ \text{C} & \sqrt{D_l t} \ll \delta_b \; . \end{array}$$

Clearly, even at low temperatures ($T < 0.3T_m$), substantial leaking could occur and the kinetics can change from type-C to type-A for prolonged annealing times.

2.2.3 Diffusion Analysis and Measurement Methods

Due to the relative diffusion speed described above, grain boundary controlled processes usually occur in the type-B and C kinetics regimes. As a result, most studies of grain boundary diffusion were made in these regimes.

As expected, for the two different kinetics regimes, the analysis methods are generally different:

Profiling Method In the type-B kinetics regime, the leakage of diffusant into the lattice is substantial, which provides an adequate signal to noise ratio for experiments that are based on the analysis of the leaked diffusant distribution in the lattice. For a thick specimen,

$$l^2 \gg D_b t \; ,$$

which corresponds to the case of diffusion into a semi-infinite solid, the mathematics based on the slab model has been established first by Fisher [20] as an approximate solution for constant source and then by Whipple [22] and Suzuoka [23, 24] for a constant source and an instantaneous source, respectively. Based on these mathematical solutions, various concentration profiling methods were developed which can be classified into two categories: (1) 2-dimensional profiling, viz. along and across the grain boundary (concentration contour method), and (2) 1-dimensional profiling in the direction normal to the diffusion source, i.e., along the diffusion direction (sectioning method). To study structural effects on grain boundary diffusion, bicrystal diffusion specimens containing grain boundaries of desired structures are used.

Surface Accumulation Method In the type-C kinetics regime, none of the above profiling methods can be properly used because a negligible amount of diffusant is leaked into the lattice. For a thin specimen,

$$l^2 \ll D_b t \,,$$

the diffusant easily diffuses from the source surface through the grain boundaries to the back surface and accumulates there. By monitoring this accumulation rate, the grain boundary diffusion parameter can be deduced. Since the diffusion is collected on one surface rather than distributed in the bulk, the surface accumulation method can usually achieve very high sensitivity.

A detailed mathematical analysis for the interpretation of the accumulation kinetics was developed by Hwang and Balluffi [25], in which the source is either constant or instantaneous and the accumulation surface is assumed to have a certain finite capacity and infinite diffusion rate. Other models [26] in which the accumulation surface is simplified as an infinite sink or a zero capacity sink have also been proposed. However, all of the models developed so far are based on idealized conditions to a certain extent, which are difficult to meet in real experiments. Better understanding of surface diffusion, the surface accumulation mechanism, segregation effects and interdiffusion effects is necessary in order to improve the analysis of the surface accumulation method.

2.2.4 Grain Boundary Diffusion Mechanism

For different solute-solvent systems, the diffusion mechanism (e.g., vacancy, interstitial, etc.), and consequently the diffusion characteristics can be vastly different. Previous studies of the grain boundary diffusion mechanism generally support the idea that the vacancy mechanism is responsible for self-diffusion and for substitutional impurity diffusion in simple metal grain boundaries [27]. These studies include measurements of the activation volume and the correlation factor of grain boundary diffusion, and computer calculations of the formation energy and migration energy and transport kinetics of point defects in grain boundaries. By measuring the effects of hydrostatic pressure on grain boundary diffusivity, the activation volumes for Ag grain boundary self-diffusion and for Zn diffusion in Al grain boundaries are determined in separate experiments [28, 29]. These measured activation volumes are fairly close to those for the lattice diffusion of Ag self-diffusion and Zn in Al respectively, which suggests that the vacancy mechanism dominates the diffusion process along those grain boundaries. The grain boundary diffusion correlation factor measurements were performed by Robinson and Peterson [30] by analyzing the isotope effects associated with grain boundary self-diffusion in Ag. In both polycrystal and bicrystal samples, they found that the correlation factor is rather large, which requires three dimensional motion for the atoms. They argued that since the probability of interstitial jumping from the grain boundary into the lattice in a close packed solid is small, the mechanisms involving interstitials are inconsistent with their observations, so that the vacancy mechanism is then the preferred interpretation. Both that the activation volumes for grain boundary diffusion are large and the isotope effect is small imply that only a relatively small number of atoms is strongly involved in a typical jump, which means that the defects involved are localized. The most direct evidence for a vacancy mechanism for grain boundary diffusion was provided by the computer simulation studies of Balluffi and co-workers [9, 10, 31]. They calculated the formation energy of different point defects by the molecular statics method and simulated the migration kinetics by the molecular dynamics in the $\Sigma 5\,(310)$ tilt boundary in Fe. They found that while interstitials are incapable of making a contribution to diffusion, the vacancies can be formed and migrate in the way that is consistent with experimental observations.

2.2.5 Effects of Grain Boundary Segregation

In polycrystalline materials with more than one atomic component, grain boundary segregation occurs inevitably through the Gibbs adsorption. Namely, preferential segregation of a component to an interface tends to occur whenever an increase in its chemical potential tends to decrease the interface free energy. From the grain boundary diffusion measurement point of view, the segregation of a diffusant could change its apparent diffusivity due to a change of its boundary concentration[4]. For example, in the mathematical model for the type-B kinetics regime, the boundary condition relating the concentration in the grain boundary and the lattice (Eq. 2.10) becomes invalid. It was shown [32] that the segregation effect could be taken into account if one replaces the grain boundary width δ_b by $s_b\delta_b$, where s_b is the grain boundary segregation factor which is defined as

$$s_b = C_b/C_l \, . \tag{2.12}$$

Clearly, the measured quantity from sectioning experiments is $s_b\delta_b D_b$ for heterodiffusion. To obtain $\delta_b D_b$, it is necessary to determine the segregation factor in separate experiments.

In the case of the surface accumulation method in the type-C kinetics regime, the boundary segregation factor defined above is not directly involved, since the lattice diffusion is frozen out so that thermal equilibrium between the grain boundary and the lattice is not required. On the other hand, the boundary conditions between the grain boundary and the free surface at the entrance and the exit of the boundary are very important in the surface accumulation method. Therefore the difference between the boundary and the surface segregation has to be taken into account. We define the surface segregation factor similarly as

$$s_s = C_s/C_l \, , \tag{2.13}$$

and define the surface/grain boundary segregation ratio as:

$$k = s_s/s_b \, . \tag{2.14}$$

---

[4] More dramatic effects due to segregation-related phenomena such as grain boundary phase transformation, precipitation etc. are out of the scope of the current discussion.

Then the boundary condition at the entrance or the exit becomes

$$kC_b = C_s \, . \tag{2.15}$$

From the above discussion, it is clear that the determination of grain boundary diffusion, in general, requires the knowledge of both grain boundary and surface segregation. There is evidence that the grain boundary segregation behavior depends strongly on the boundary structure [8], which means that measured results involving the structure dependence of the grain boundary diffusivity during heterodiffusion always reflect the combined effects of both diffusion and segregation if the segregation effects are not well separated.

2.2.6 Effects of Diffusion-Induced Grain Boundary Migration

In grain boundary diffusion analyses, it is usually assumed that the grain boundaries involved are stationary during the diffusion annealing. However, it was discovered that when a solute diffuses along a grain boundary in a pure metal or a solid solution, the grain boundary may migrate, leaving the region behind either enriched by or depleted of the solute, leading to the formation of an alloyed zone in the former case and a dealloyed zone in the latter [33]. This phenomenon called diffusion-induced grain boundary migration (DIGM) is believed to occur in essentially all substitutional alloys [34], and accordingly, can greatly change the apparent grain boundary diffusion rate in these systems. For example, in a sectioning experiment, the measured solute concentration in the lattice could be much larger than the leakage due to lattice diffusion. On the other hand, in a surface accumulation measurement, the surface accumulation rate could be slowed down due to solute deposition in the film.

In principle, if the grain boundary migration velocity and the concentration in the alloyed zone are known, the diffusion results can be corrected. However, at this stage, the understanding of DIGM is rather poor. Thus it is impossible to provide any quantitative corrections. Experimental observations also showed that DIGM appears to be irregular in terms of start or stop conditions, migration direction, extent of the migration, activation energy, etc. Up to now, although many grain boundary diffusion experiments were performed where DIGM could very well occur and severely affect the measured diffusion results, there has been no attempt to address this problem.

2.3 Previous Works on Structural Effects

Among the limited number of studies devoted to the understanding of the effects of grain boundary structure on grain boundary diffusion, most of them were made on symmetric tilt boundaries, because these boundaries are simplest in terms of structure. Thus, their diffusion characteristics could be relatively easily linked to their structures. For the above reason, as well as the relevance to the current work, this section will be confined to discussing previous work on symmetric tilt boundaries. It is convenient to make separate discussions of this issue for the low and high angle boundary regions respectively. The former is considerably simpler and is therefore understood to a large extent, while the later still remains controversial in many respects.

2.3.1 Low Angle Tilt Boundaries

As described in Section 2.1.2, a small angle tilt boundary consists of equally spaced parallel primary dislocations. Based on this fact, Turnbull and Hoffman [35] proposed a "pipe" model of diffusion. In this model, they assumed that the lattice between the dislocations is strained but relatively perfect with a diffusivity similar to that of the perfect lattice. The dislocation core is highly disordered and has a much larger diffusivity, and therefore acts like a "short circuit" for diffusion or a diffusion "pipe". The grain boundary is represented by a planar array of pipes of cross-section area A_d. The measured grain-boundary diffusion parameter presented by using the slab model may be stated in terms of the dislocation model:

$$\delta_b D_b = D_d \frac{A_d}{d_p} , \tag{2.16}$$

where d_p is the spacing between primary dislocations, which is related to the tilt angle by Eq. 2.1. Therefore,

$$\delta_b D_b = 2 D_d A_d \frac{\sin \theta/2}{b} \ . \tag{2.17}$$

This model makes some predictions that can be tested experimentally:

(1) For small angle boundaries, the interaction between dislocations is negligible so that D_d remains constant with θ. The relationship between grain boundary diffusivity and misorientation angle is then simply

$$\delta_b D_b \sim \sin \theta/2 \ . \tag{2.18}$$

Further, since the activation energy ε_b depends on the mechanism of diffusion, not on the dislocation density within the limits of this model, it follows that ε_b is independent of θ. These predictions are supported by experiments on self-diffusion along low angle [001] tilt boundaries in silver bicrystals by Turnbull and Hoffman [35] and along similar tilt boundaries in copper and nickel bicrystals [36, 37, 38].

(2) On the basis of this model, diffusion in the boundary should be highly anisotropic at small θ, and $\delta_b D_b$ parallel to the dislocations should be much larger than that perpendicular to the dislocations. This prediction was first confirmed experimentally by Hoffman [39] who reported that the ratio of the diffusion parallel and perpendicular to the dislocation cores $D_{b\|}/D_{b\perp}$ for self-diffusion in symmetric [001] tilt boundaries of Ag decreases smoothly as tilt angle increases, but some anisotropy exists up to the maximum tilt angle of 45°.

2.3.2 High Angle Tilt Boundaries

At large misorientation angles, dislocation cores are severely distorted and it is more appropriate to describe the grain boundary core structures by using the SU model for the structure. Correspondingly, the grain boundary diffusion properties should be better described by the SU model for diffusion[5]. It should be noted that

---

[5] See Section 2.1.2 for details.

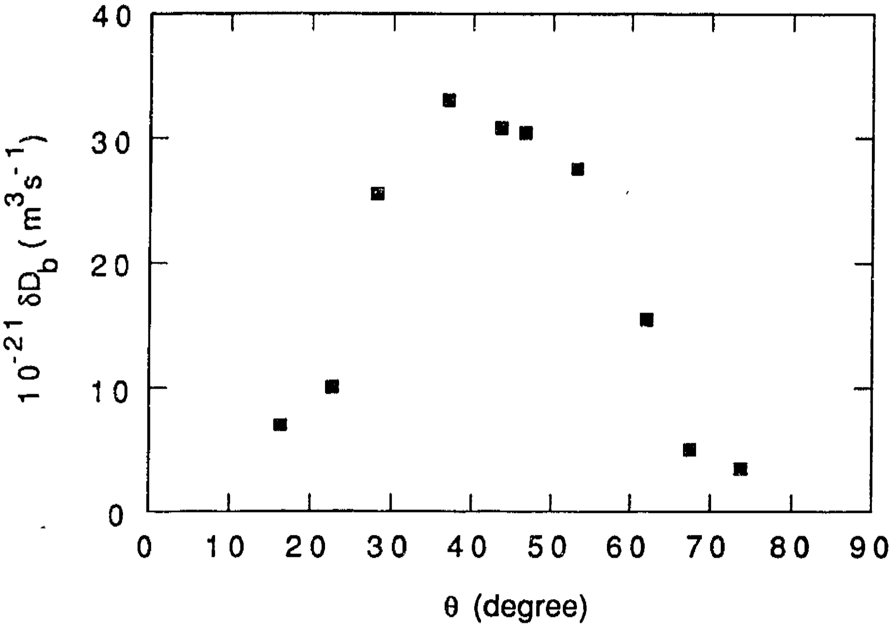

Figure 2-5: Grain boundary self-diffusion of Ag along [001] tilt grain boundaries, after Sommer et al. [41].

the SU model includes the dislocation model as a special case in the low angle region.

The most basic feature predicted by the SU model is that the grain boundary diffusion properties change with misorientation angle continuously within an angular range between two delimiting boundaries. This prediction has been verified in a number of studies [37, 40, 41]. Fig. 2-5 illustrates the orientation dependence of $\delta_b D_b$ in the Ag self-diffusion along symmetric [001] tilt boundaries by Sommer et al. [41].

However, in other work [6, 7][6], the presence of cusps at CSL misorientations was evident, which can not be satisfactorily explained by the SU model. Fig. 2-6 illustrates the results obtained by Aleshin et al. [6] for chemical diffusion in the same symmetric [001] tilt boundaries in the Al/Zn system. These results on the contrary, show sharp minima cusps at the CSL misorientations. These cusps were explained by relating them to the existence of cusps in the grain boundary energy vs. misorientation curves. In fact, it was found in these studies that the activation energies in the CSL

---

[6] An interesting observation is that all of the measurements that showed cusps in the [001] tilt series were performed in chemical diffusion systems, and therefore may have been influenced by certain chemical effects discussed in Section 2.2.5 and 2.2.6.

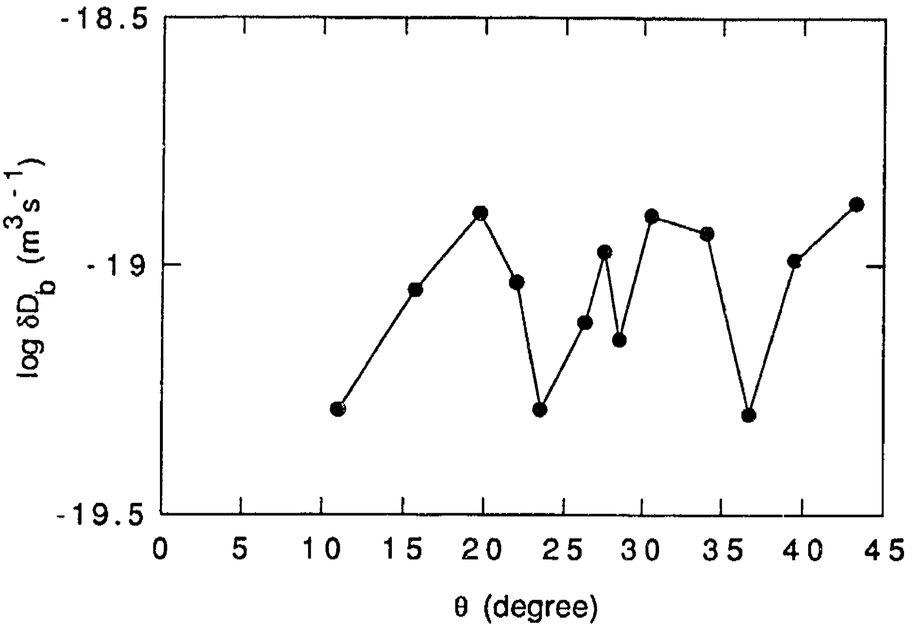

Figure 2-6: Grain boundary chemical diffusion along [001] tilt grain boundaries in Al/Zn system, after Aleshin et al. [6].

boundaries are larger than those in more general boundaries. Attempts were also made to correlate the activation energy and the quantity Σ [1, 42], which was assumed to be a measure of the degree of "perfection" of the boundaries.

Comparing the above two examples, it is clear that the most basic characteristics of grain boundary diffusion are yet to be understood. A thorough review and a complete compilation of the previous works can be found in references [43, 44].

Chapter 3

Multi-Crystal Surface Accumulation Method

Historically, the bicrystal depth profiling method has been the main means for studying structural effects on grain boundary diffusion. In this method, material is generally diffused from a surface source into a semi-infinite bicrystal with the grain boundary perpendicular to the source surface as shown schematically in Fig. 3-1a. Rapid diffusion then takes place along the grain boundary, while slower but simultaneous leakage into the lattice occurs provided that the annealing temperature is high enough. The distribution of the diffusion material in the lattice is then measured, which provides information about the grain boundary diffusivity. Appreciable leakage from the grain boundary to the lattice is usually essential for an adequate signal level, which in turn limits its application to the Harrison type-A and B kinetics regimes ($T > \frac{1}{3}T_m$).

To study structural effects in the type-C kinetics regime ($T < \frac{1}{3}T_m$), a special multi-crystal surface accumulation method is developed, which combines the beauty of having a well defined grain boundary structure and the superb sensitivity of surface analysis techniques. In this method (illustrated in Fig. 3-1b), specially prepared multi-crystal diffusion specimens are used, in which all of the transverse boundaries are parallel to each other and are of the same type (i.e., with the same misorientation and inclination). At relatively low temperatures ($T < \frac{1}{3}T_m$), lattice diffusion is frozen

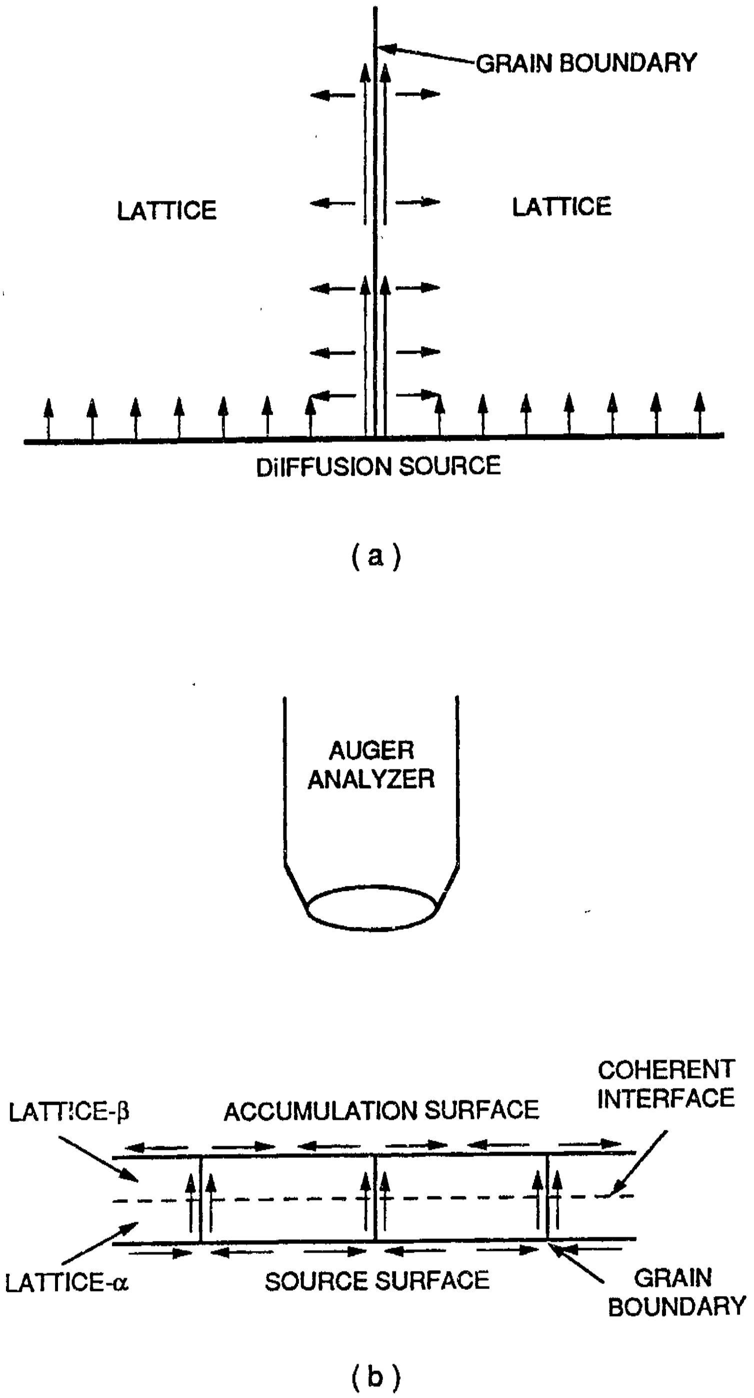

Figure 3-1: Schematic diagrams illustrating (a) the bicrystal profiling method, and (b) the surface accumulation method.

out, and atoms are diffused from the source surface to the accumulation surface through the transverse grain boundaries. The average chemical compositions of both surfaces are then monitored as functions of time, which allows a direct measurement of the grain boundary diffusion parameter, $\delta_b D_b$, to be made. In contrast to the depth profiling method, where the diffusant is distributed over a large volume, the accumulation method collects the diffusant on one single surface. As a result, a measurable concentration on the accumulation surface can be obtained with only a relatively small amount of mass transport occurring along the grain boundary, during which any lattice diffusion is negligible.

This technique is similar to that used earlier by Hwang and Balluffi [25, 45], but incorporates a number of major improvements in addition to the use of multicrystal diffusion specimens. These include a better defined constant source condition, the elimination of effects due to any segregation at the boundary or the source and accumulation surfaces and the elimination of the effects caused by DIGM. In this chapter, the basic diffusion model is presented first. Then the detailed experimental procedure is described including specimen preparation, measurement and calibration.

3.1 Diffusion Model

Consider a thin film specimen of thickness l which contains an array of parallel grain boundaries of the same type running perpendicular to the surfaces spaced at the distance b as shown in Fig. 3-2. The film consists of two layers of different materials α and β separated by a coherent interface. Surface 2 (top surface) serves as the accumulation surface for α atoms, but the source surface for β atoms and vice versa. The grain boundary is represented by a thin slab of uniform thickness δ_b with intrinsic grain boundary diffusion coefficients $D_{b\alpha}$ and $D_{b\beta}$ for the two different atoms respectively. Outside the slab, the diffusion coefficient is assumed to be zero, which corresponds to the fact that lattice diffusion is frozen out in the type-C kinetics regime. Similarly, both surface slabs are assumed to have an effective thickness δ_s

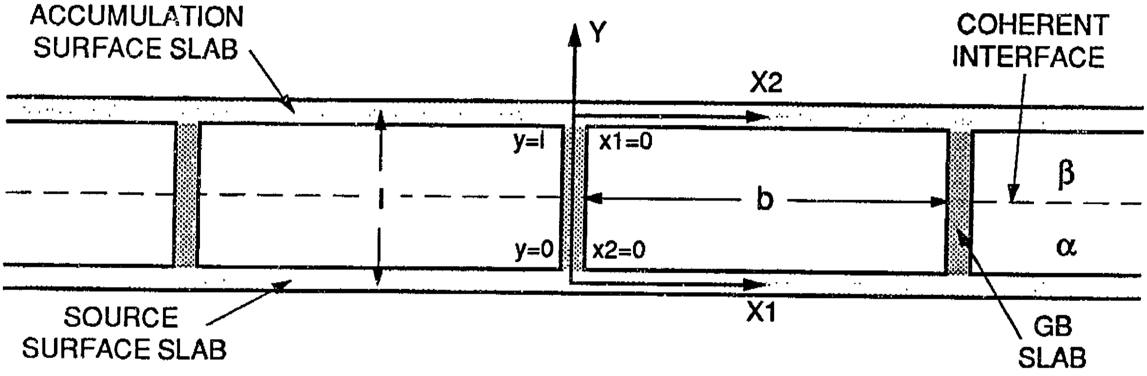

Figure 3-2: Schematic diagram of the diffusion model. Both the grain boundaries and the surfaces are treated as uniform thin slabs of thickness δ_b and δ_s, respectively.

and surface diffusion coefficients $D_{s\alpha}$ and $D_{s\beta}$. The concentration of the diffusion species α and β in the grain boundary is represented by $C_{b\alpha}$ and $C_{b\beta}$ respectively. The surface concentrations are similarly represented by $C_{s\alpha 1}$, $C_{s\beta 1}$, $C_{s\alpha 2}$ and $C_{s\beta 2}$. It is assumed that the volume change due to chemical mixing is negligible, which is true for the Au/Ag system. As a result, it is convenient to normalize the concentration so that

$$C_\alpha + C_\beta = 1 \ .$$

The coordinates shown in Fig. 3-2 have two horizontal axes, x_1 and x_2, for each surface and have one vertical axis y for the grain boundary. Due to symmetry, it is only necessary to consider the diffusion problem within the following region:

$$0 < x_1 < b/2 \ , \quad 0 < x_2 < b/2 \ , \quad 0 < y < l \ .$$

For a chemical diffusion system, the intrinsic diffusivities of the two species are generally different, so that the diffusion flux is unbalanced, resulting in some parts of the diffusion circuit gaining net material with other parts losing net material.

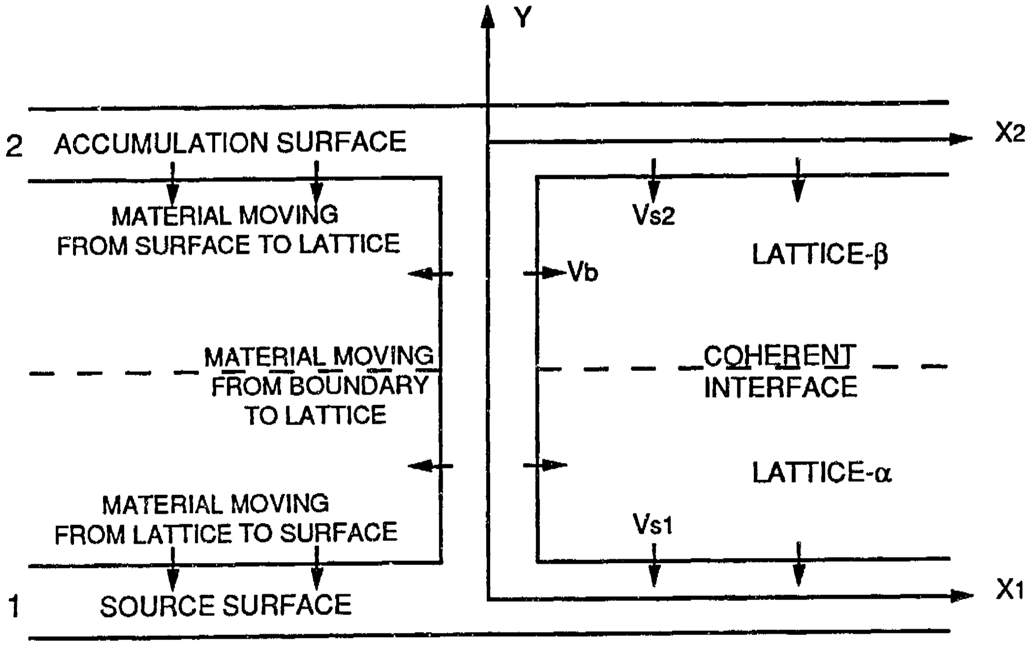

Figure 3-3: Schematic diagram showing material moving into or out of grain boundary and surface slabs.

If we assume that D_α is greater than D_β everywhere, then a net atomic flux will be established from surface 1 to surface 2. Surface 1 thus loses material, and the continuity equations in it are

$$\frac{\partial C_{s\alpha 1}}{\partial t} = \frac{\partial}{\partial x_1}(D_{s\alpha}\frac{\partial C_{s\alpha 1}}{\partial x_1}) + \frac{v_{s1}}{\delta_s}(1) \ , \tag{3.1}$$

$$\frac{\partial C_{s\beta 1}}{\partial t} = \frac{\partial}{\partial x_1}(D_{s\beta}\frac{\partial C_{s\beta 1}}{\partial x_1}) + \frac{v_{s1}}{\delta_s}(0) \ , \tag{3.2}$$

in which the velocity term v_{s1}/δ_s describes the process in which pure α atoms move into the surface slab from the lattice as illustrated in Fig. 3-3. On the other hand, surface 2 gains material, and the corresponding equations are

$$\frac{\partial C_{s\alpha 2}}{\partial t} = \frac{\partial}{\partial x_2}(D_{s\alpha}\frac{\partial C_{s\alpha 2}}{\partial x_2}) - \frac{v_{s2}}{\delta_s}C'_{s\alpha 2} \ , \tag{3.3}$$

$$\frac{\partial C_{s\beta 2}}{\partial t} = \frac{\partial}{\partial x_2}(D_{s\beta}\frac{\partial C_{s\beta 2}}{\partial x_2}) - \frac{v_{s2}}{\delta_s}C'_{s\beta 2} \ , \tag{3.4}$$

where

$$C'_{s\alpha 2} = \frac{1}{S_{s\alpha}} C_{s\alpha 2} , \qquad C'_{s\beta 2} = 1 - C'_{s\alpha 2} \tag{3.5}$$

The velocity terms in the above two equations describe the process in which material moves out of the surface slab. The concentration of material deposited in the lattice is different from that in the slab and they are related by Eq. 3.5. where $S_{s\alpha}$ is a function of the effective surface segregation factor (see discussion in Section 3.1.3).

The grain boundary can also gain or lose material, especially in the transient period. The condition under which it gains or loses material will be discussed later in Section 3.1.7. In general, for the part of the boundary that gains material, we have

$$\frac{\partial C_{b\alpha}}{\partial t} = \frac{\partial}{\partial y}\left(D_{s\alpha} \frac{\partial C_{b\alpha}}{\partial y}\right) - \frac{v_b}{\delta_b} C_{b\alpha} , \tag{3.6}$$

$$\frac{\partial C_{b\beta}}{\partial t} = \frac{\partial}{\partial y}\left(D_{b\beta} \frac{\partial C_{b\beta}}{\partial y}\right) - \frac{v_b}{\delta_b} C_{b\beta} . \tag{3.7}$$

For the part of boundary that looses material, the equations are

$$\frac{\partial C_{b\alpha}}{\partial t} = \frac{\partial}{\partial y}\left(D_{b\alpha} \frac{\partial C_{b\alpha}}{\partial y}\right) + \frac{v_b}{\delta_b} C_{l\alpha} , \tag{3.8}$$

$$\frac{\partial C_{b\beta}}{\partial t} = \frac{\partial}{\partial y}\left(D_{b\beta} \frac{\partial C_{b\beta}}{\partial y}\right) + \frac{v_b}{\delta_b} C_{l\beta} , \tag{3.9}$$

where $C_{l\alpha}$ and $C_{l\beta}$ are the concentrations in the adjacent lattice.

If α atoms move considerably faster than β atoms (as in the case of the Ag/Au system), it is easy to realize that eventually the system will be saturated with a high concentration of α atoms. If the surfaces are then cleaned just before the measurement, the boundary is still charged with α atoms. For the sake of simplicity, we therefore assume the initial condition as

$$C_{s\alpha 1} = C_{b\alpha} = 1 , \quad C_{s\alpha 2} = 0 , \quad t = 0 . \tag{3.10}$$

It is noted that the initial condition is important only in the short transient period at the very beginning. Thus, it should not affect the diffusion behavior in the later quasi-steady state.

The requirement of flux continuity establishes the boundary conditions which connect the surfaces and the grain boundary. They are

$$k_\alpha C_{b\alpha} = C_{s\alpha 2} \ , \tag{3.11}$$

$$\frac{1}{2}\delta_b D_{b\alpha} \frac{\partial C_{b\alpha}}{\partial y} = \delta_s D_{s\alpha} \frac{\partial C_{s\alpha 2}}{\partial x_2} \ , \tag{3.12}$$

at

$$x_2 = 0, \ y = l \ ,$$

and

$$k_\beta C_{b\beta} = C_{s\beta 1} \ , \tag{3.13}$$

$$\frac{1}{2}\delta_b D_{b\beta} \frac{\partial C_{b\beta}}{\partial y} = \delta_s D_{s\beta} \frac{\partial C_{s\beta 1}}{\partial x_1} \ , \tag{3.14}$$

at

$$x_1 = 0, \ y = 0 \ ,$$

where k_α and k_β are the surface/boundary segregation ratios for the α and β species respectively. These quantities will be discussed further in Section 3.1.4. Other boundary conditions on the surfaces are

$$\frac{\partial C_{s\alpha 2}}{\partial x_2} = 0, \qquad x_2 = b/2 \ ; \tag{3.15}$$

$$\frac{\partial C_{s\beta 1}}{\partial x_1} = 0, \qquad x_1 = b/2 \ . \tag{3.16}$$

With the above diffusion model established, we then proceed to discuss various aspects of the model in order to improve our general understanding of the diffusion system. A computer program is developed which is fully capable of solving the above equations numerically with the flexibility of changing all of the parameters used. These solutions are frequently used to assist our discussion. Whenever it is possible, the parameters used in the calculations are chosen to reflect the real physical properties of the Ag (α) and Au (β) atoms. Table 3.1 lists the parameters used in the

l (Å)	b/l	δ_b (Å)	δ_s (Å)
2000	10	5	4
$D_{b\alpha}$ (Å^2/s)	D_β/D_α	D_s/D_b	v_m (Å/s)
2×10^4	0.2	100	0
$S^0_{s\alpha}$	k^0_α	k^0_β	λ
2.5	2.5	0.2	0

Table 3.1: Common parameters used in diffusion model calculations.

calculations, unless otherwise specified.

3.1.1 Quasi-Steady State

When the diffusion begins, the system undergoes a complicated transient period, during which it adjusts itself so that sharp concentration gradients disappear. After that, a quasi-steady state is reached in which the source and sink conditions change slowly, so that a virtually constant atomic flux is established through the boundary. Since the behavior of a quasi-steady state is much simpler than a transient state, any measurements should be performed in the period of quasi-steady state. The condition for being able to establish a quasi-steady state is that the source and sink capacities are large compared with the amount of material diffused through the boundary during the relaxation period of the boundary, or

$$\delta_s b \gg j\tau_b \approx \left(\frac{\delta_b D_b}{l}\right)\left(\frac{l^2}{D_b}\right) .$$

Since $\delta_b \approx \delta_s$, the above relation reduces to

$$\frac{b}{l} \gg 1 .$$

Figure 3-4[1] shows the calculated accumulation profiles of α atoms (the quantity

---

[1] In this and other figures in Section 3.1 presenting calculated profiles, the parameters on the right are listed in the sequence corresponding to the grey level of the curves from dark to light.

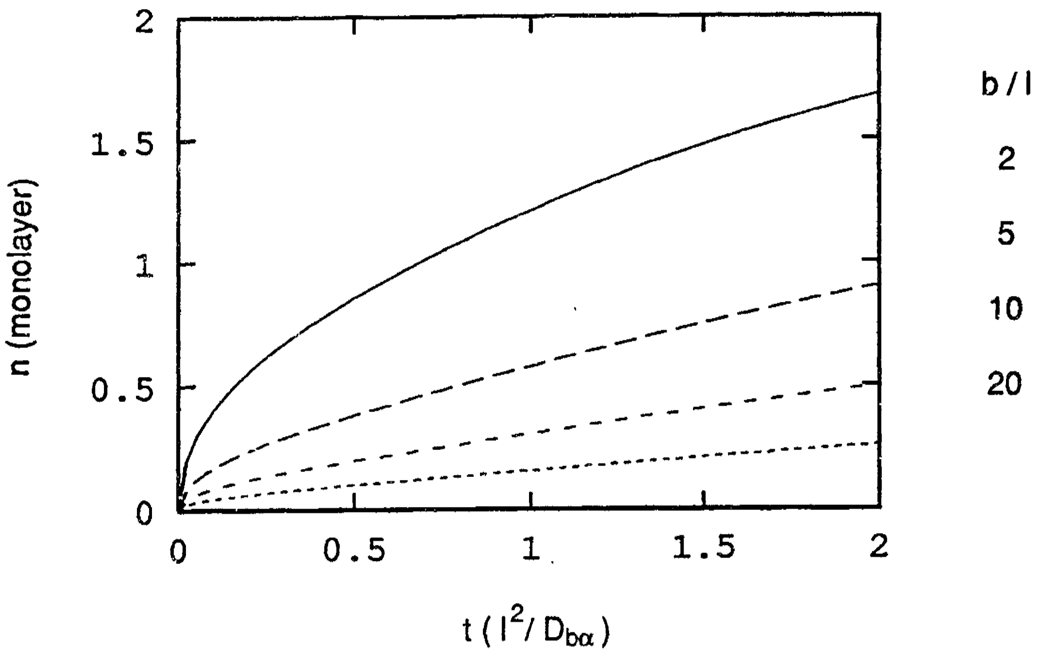

Figure 3-4: Calculated surface accumulation profiles for different b/l ratios.

of α atoms built up on surface 2 as a function of time) for several b/l ratios. The quasi-steady state is very quickly reached for a large b/l ratio, but difficult to establish for a small b/l ratio. However, when b is so large that the rate of surface diffusion begins to limit the source or sink effectiveness, further increase in b will only degrade the sensitivity of the method. We should then limit b so that

$$\frac{b^2}{D_s} \ll \frac{l^2}{D_b}.$$

Combining the above two relations, we then have

$$1 \ll \frac{b}{l} \ll \sqrt{\frac{D_s}{D_b}}. \tag{3.17}$$

3.1.2 Surface/Grain Boundary Diffusivities Ratio

Generally, surface diffusion is considerably faster than grain boundary diffusion at relatively low temperatures. However, in many cases, the surface diffusion coefficient

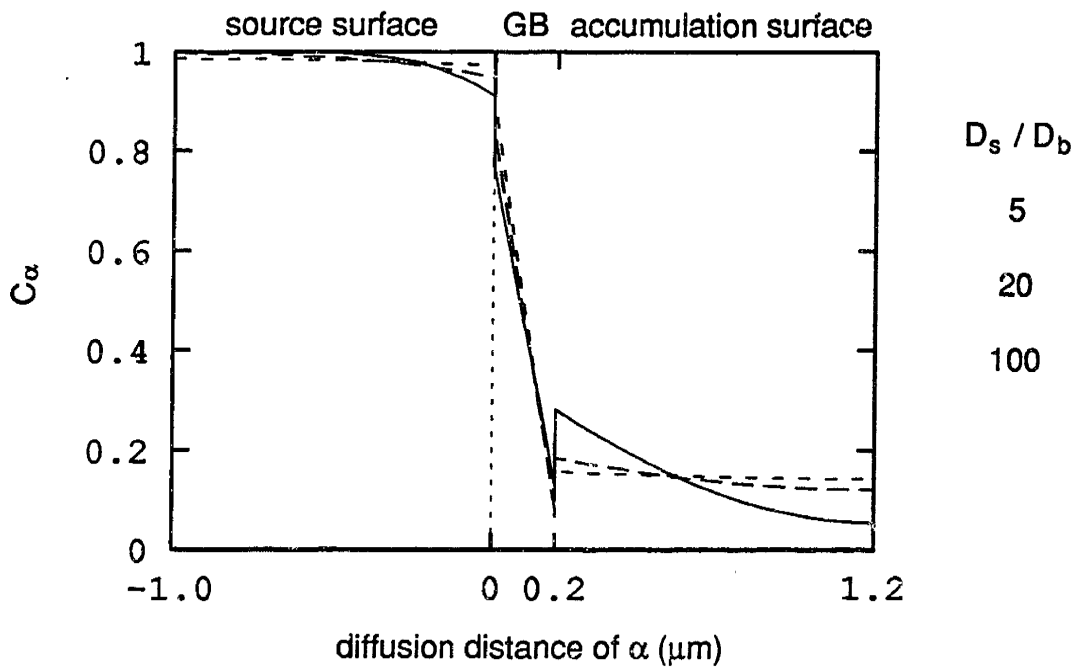

Figure 3-5: Calculated α concentration profiles in the grain boundary and the surface slabs for different D_s/D_b ratios.

is not quantitatively known. It is then necessary to investigate how its magnitude affects the diffusion behavior. In Fig. 3-5 the concentration of α atoms on both surfaces and in the boundary is plotted for several different D_s/D_b ratios. For large D_s/D_b ratios, the surface concentrations are very flat. But for smaller ratios, the accumulated material does not spread out fast enough and it piles up in the region close to the boundary exit. This affects the source and sink strengths and consequently reduces the amount of diffusion through the boundary.

3.1.3 Surface Accumulation

Surface accumulation is an extremely complicated process with diffusion, chemical mixing and material deposition or removal occurring simultaneously. Current knowledge of the details of this process is practically non-existent. In our model, we assume that the atoms diffuse in a surface slab of fixed thickness which has a diffusion coefficient as described earlier. Diffusion and mixing is allowed only inside this slab. The deposition or removal of material is taken care of by letting material move out of the slab into the lattice or move from the lattice into the slab. It is not necessary to assume that inside the slab the concentration is uniform in the direction perpendicular to the surfaces (the chemical potential is determined by the average concentration in the slab). In fact, recent calculations [46, 47] show that the solute segregation occurs primarily in the top monolayer, and that the concentration of solute in the atomic layers close to the top surface layer is approximately the same as that in the lattice if thermal equilibrium is established. The α concentration in the top layer C_α^1 and the concentration in the remaining part of the slab C_α^r can be related by the surface segregation factor:

$$C_\alpha^1 = s_{s\alpha} C_\alpha^r \ , \tag{3.18}$$

from which it is easy to derive:

$$C_\alpha^r = \frac{1}{\frac{a}{\delta_s}(s_{s\alpha} - 1) + 1} C_{s\alpha 2} \ . \tag{3.19}$$

Since the concentration of the material moving out of the slab in the case of surface gaining material (surface 2), $C'_{s\alpha 2}$ equals C_α^r, we have

$$\mathcal{S}_\alpha = \frac{a}{\delta_s}(s_{s\alpha} - 1) + 1 \ . \tag{3.20}$$

In general, $s_{s\alpha}$ is both temperature and concentration dependent. According to the McLean isotherm,

$$\frac{C_\alpha^1}{1 - C_\alpha^1} = \frac{C_\alpha^r}{1 - C_\alpha^r} s_{s\alpha}^0(T) \ , \tag{3.21}$$

where

$$s_{s\alpha}^0(T) = \exp(-\frac{g_{s\alpha}}{kT}) \tag{3.22}$$

is the segregation factor at the dilute α concentration limit, in which $g_{s\alpha}$ is the Gibbs free energy for surface segregation of α atoms.

By solving Eq. 3.18, 3.19 and 3.21, $s_{s\alpha}$ can be expressed in terms of $s_{s\alpha}^0$ and $C_{s\alpha 2}$, which can then be used in Eq. 3.20.

The surface accumulation of α atoms is calculated for several different $s_{s\alpha}^0$ values. The results indicate that the accumulation rate in the early period of diffusion is not

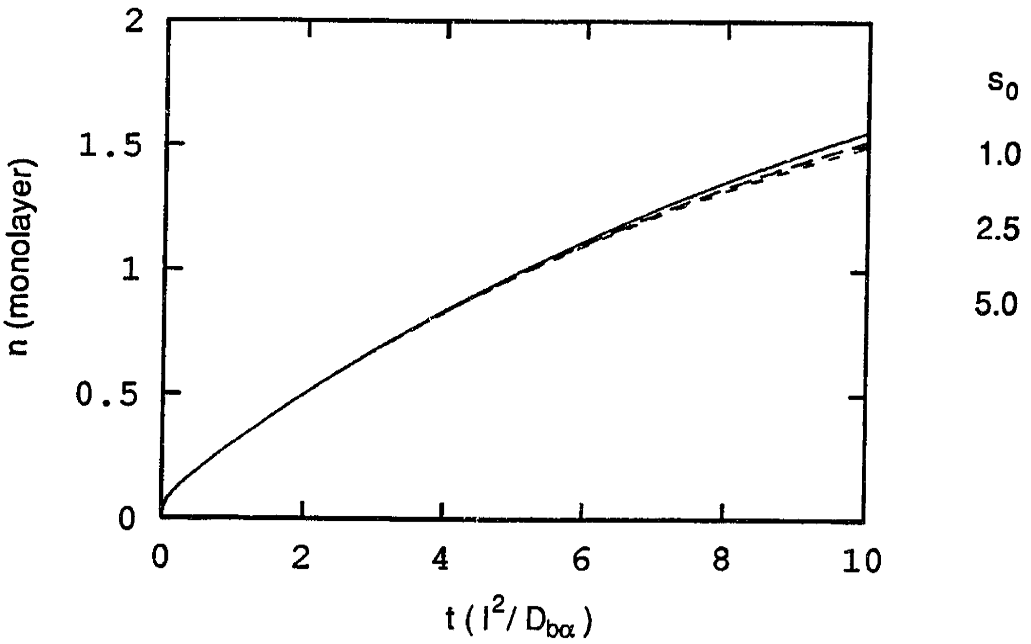

Figure 3-6: Calculated surface accumulation profiles for different values of surface segregation factors.

sensitive to the effective segregation factor (Fig. 3-6).

Another parameter that is important for the accumulation is the surface slab thickness, which determines the surface capacity for accumulation. It is conceivable that for a thicker slab, the surface has larger capacity, and thus saturates more slowly. Fig. 3-7 shows the accumulation of α atoms as a function of time. It is clear that in the early period of diffusion, the accumulation rate dn/dt is not sensitive to the choice of surface layer thickness δ_s, except in the extreme case where the surface slab consists of only one monolayer of atoms.

3.1.4 Surface/Boundary Segregation Ratio

The surface accumulation method is very sensitive to the boundary conditions that connect the surfaces and the grain boundary. The segregation ratio changes the apparent source or sink strength and therefore changes the grain boundary atomic flux and the surface accumulation rate. Since the grain boundary segregation factor is a function of grain boundary structure, it is necessary to consider the effects of the segregation ratio on the measured accumulation rate. Here we assume that local

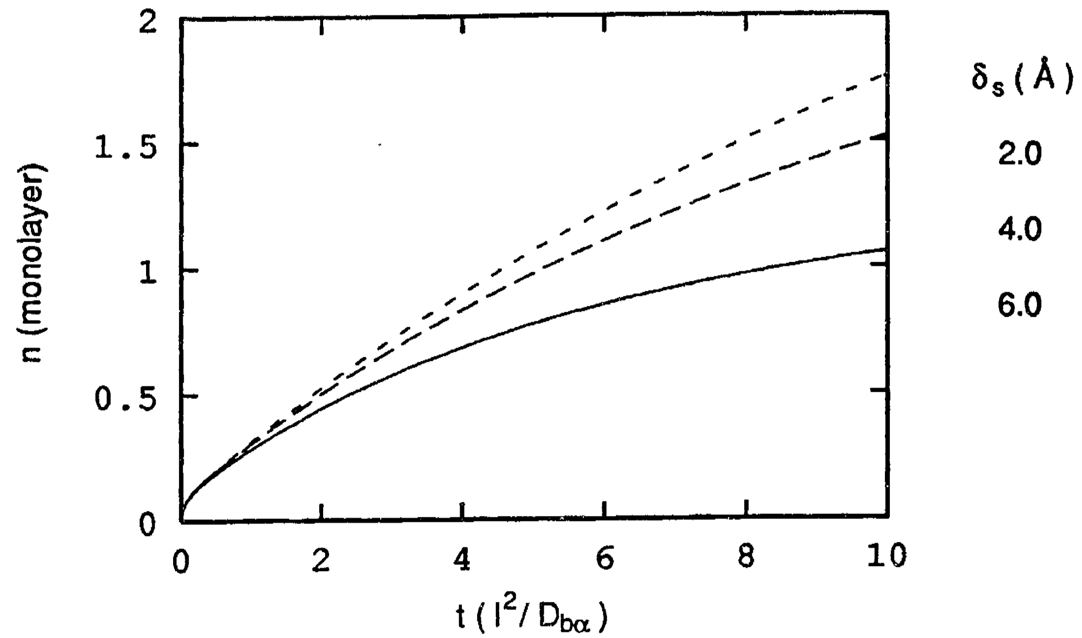

Figure 3-7: Calculated surface accumulation profiles for different choices of δ_s.

equilibrium is maintained at the two junctions of the boundary with the surfaces. The concentration discontinuities there can then be described by the two segregation ratio parameters k_α and k_β, which should be concentration dependent in general. By using the McLean isotherm, we have

$$\frac{C_{s\alpha 2}}{1 - C_{s\alpha 2}} = \frac{C_{b\alpha}(l)}{1 - C_{b\alpha}(l)} k_\alpha^0 \; ; \tag{3.23}$$

$$\frac{C_{s\beta 1}}{1 - C_{s\beta 1}} = \frac{C_{b\beta}(0)}{1 - C_{b\beta}(0)} k_\beta^0 \, . \tag{3.24}$$

The segregation ratios k_α and k_β can be obtained by solving Eq. 3.11, 3.13, 3.23 and 3.24.

From Fig. 3-8, it is apparent that the accumulation rate is insensitive to changes of the segregation ratio at the early stage of diffusion.

3.1.5 Constant Source

In the grain boundary diffusion experiment by Hwang and Balluffi [45], a thick layer of silver was used as the diffusion source. It was observed that the Au signal

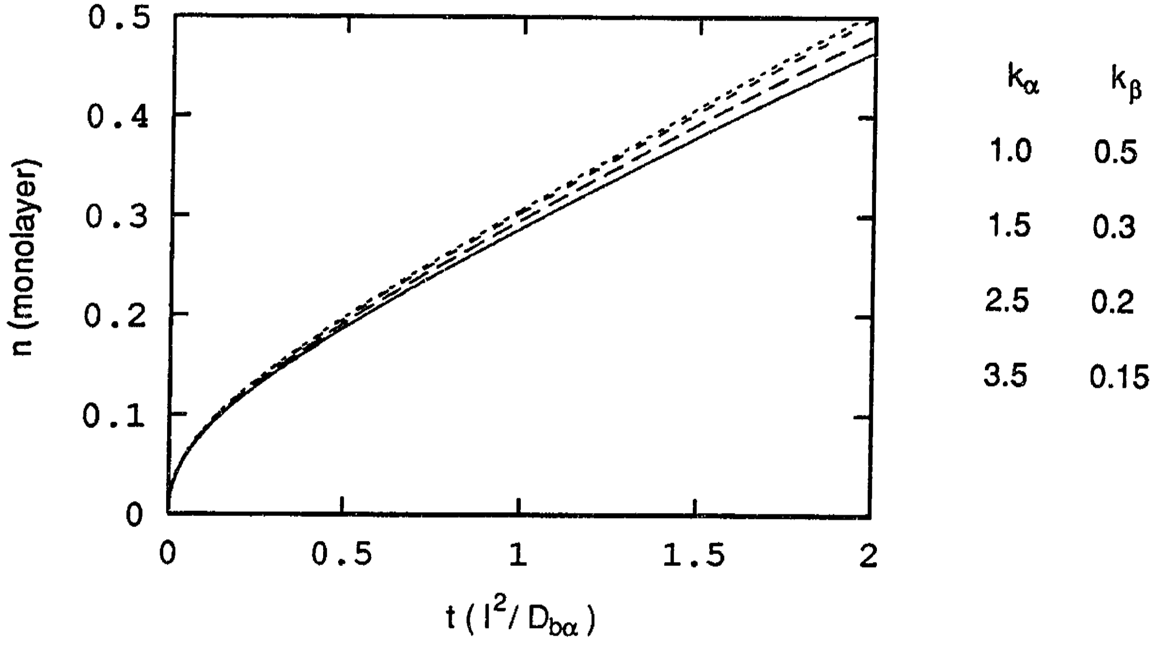

Figure 3-8: Calculated surface accumulation profiles for different surface/boundary segregation ratios.

on the Ag source surface always remained below the limit of detection of their Auger system. This result led to the assumption that the effective constant source of Ag was located somewhere between the Ag surface and the Ag/Au interface. In order to remove this ambiguity, a thin layer of Ag is used in the current method, and the Ag surface serves as the unambiguous source for the silver atoms. We must then ask under what conditions this source surface acts as a constant source. Calculations of the accumulated quantities of α and β atoms on surfaces 2 and 1 (Fig. 3-9 and Fig. 3-10 respectively) show clearly that if the diffusivity ratio D_α/D_β is large enough, surface 1 remains essentially free of β atoms in the early stage of diffusion, while α atoms accumulate on surface 2 at a virtually constant rate. Under these conditions, surface 1 acts as a constant source for all practical purposes.

3.1.6 Concentration Dependence of Diffusivity

It is generally observed in lattice diffusion experiments that if the α atoms move faster than the β atoms in a $\alpha-\beta$ alloy, then the diffusion coefficients for both the α and β species will increase with increasing α concentration. For the sake of simplicity,

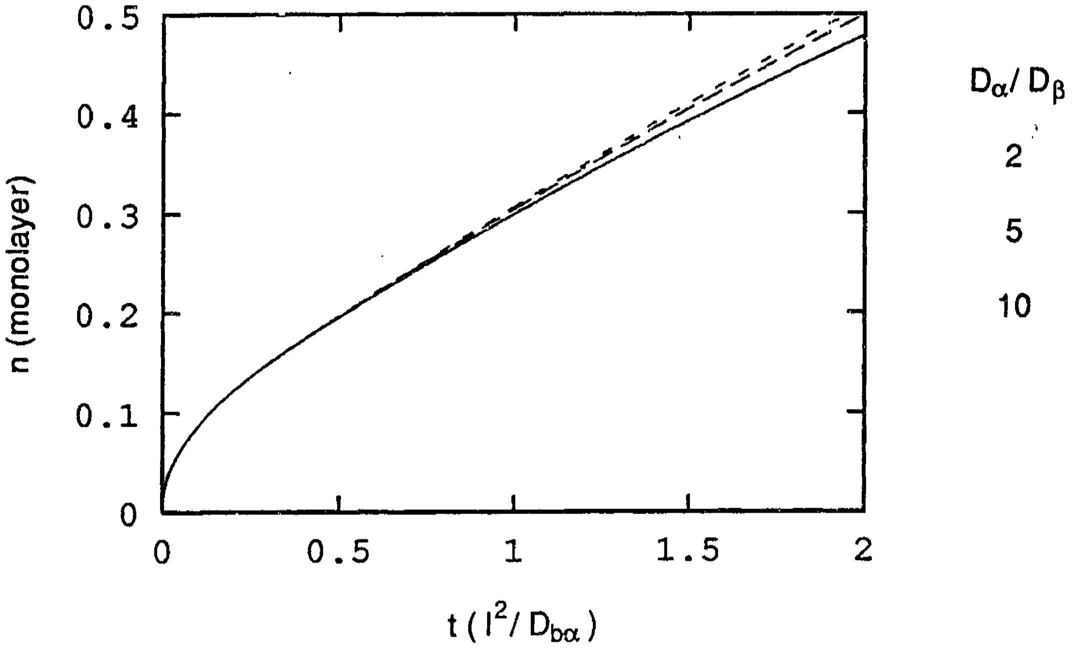

Figure 3-9: Calculated surface accumulation profiles of α for different D_α/D_β ratios.

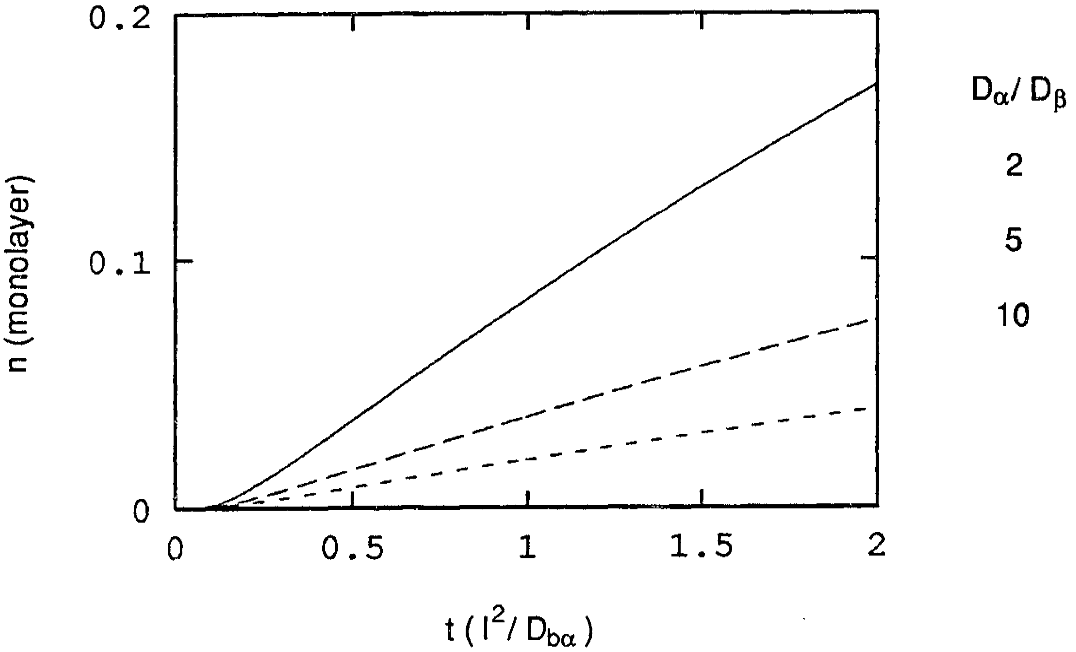

Figure 3-10: Calculated surface accumulation profiles of β for different D_α/D_β ratios.

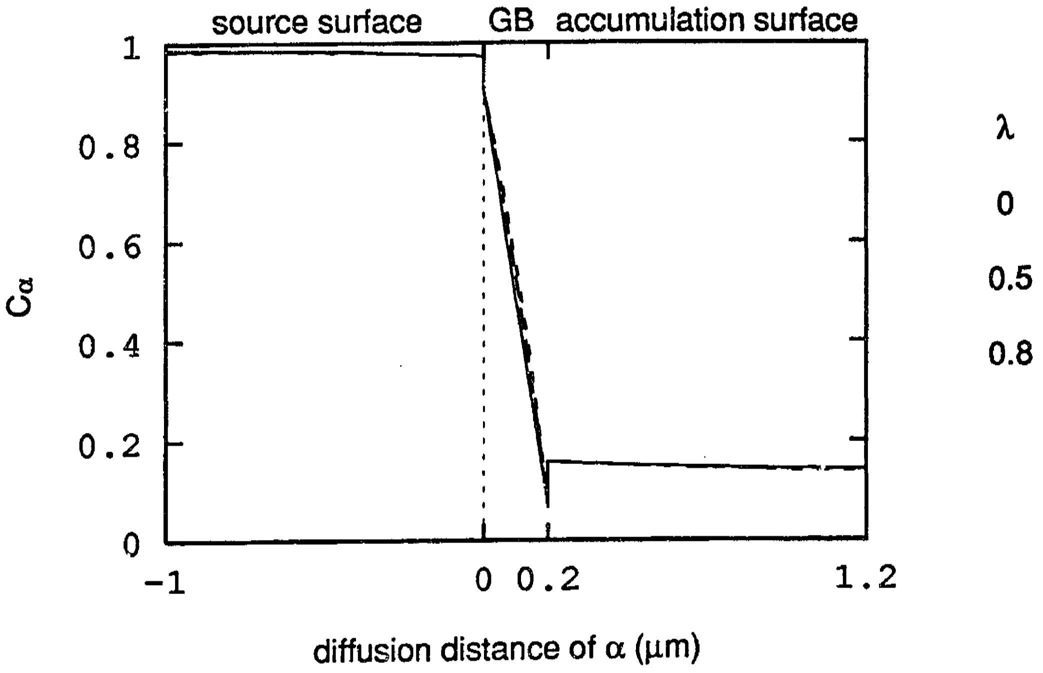

Figure 3-11: Calculated α concentration profiles in the grain boundary and the surface slabs for different λ values.

we assumed the following concentration dependence for our diffusion system

$$D = D^{*} \exp(\lambda C_{\alpha}) . \tag{3.25}$$

To study how the concentration dependence changes the general diffusion behavior, we calculated the concentration profile for several λ values. Different D^{*} are used so that the average diffusivity

$$\overline{D} = \int_{0}^{1} D dC_{\alpha} = D^{*}(e^{\lambda} - 1)/\lambda$$

remains the same for all calculations. It is clear from the calculated results (Fig. 3-11) that only the boundary concentration shows different curvatures for different λ values. The surface concentrations are essentially the same for the same average diffusivity, which implies that from the surface accumulation measurement we can only obtain the average diffusivity.

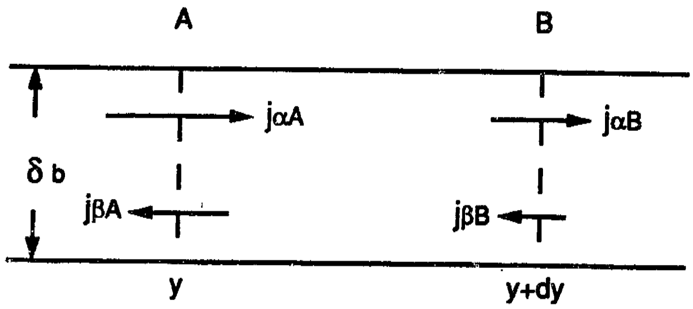

Figure 3-12: Schematic diagram showing the unbalanced atomic flux in a small grain boundary section AB.

3.1.7 Effects of Grain Boundary as Source or Sink

In the current diffusion model, although the grain boundary serves primarily as a diffusion path, it could gain or lose material during diffusion. Consider a small section of the boundary slab AB as illustrated in Fig. 3-12. The rate at which material deposits in this section is

$$\begin{aligned} & j_{\alpha A} - j_{\beta A} - j_{\alpha B} + j_{\beta B} \\ & = -(D_{b\alpha}\tfrac{\partial C_{b\alpha}}{\partial y})_y + (D_{b\beta}\tfrac{\partial C_{b\beta}}{\partial y})_y + (D_{b\alpha}\tfrac{\partial C_{b\alpha}}{\partial y})_{y+dy} - (D_{b\beta}\tfrac{\partial C_{b\beta}}{\partial y})_{y+dy} \\ & = \tfrac{\partial}{\partial y}(\Delta D_b \tfrac{\partial C_{b\alpha}}{\partial y})dy \ , \end{aligned}$$

where $\Delta D_b = D_{b\alpha} - D_{b\beta}$.

So the condition for section AB to gain material is

$$\frac{\partial}{\partial y}(\Delta D_b \frac{\partial C_{b\alpha}}{\partial y}) > 0 \ , \qquad (3.26)$$

or

$$\frac{\partial \Delta D_b}{\partial C_{b\alpha}}(\frac{\partial C_{b\alpha}}{\partial y})^2 + \Delta D_b \frac{\partial^2 C_{b\alpha}}{\partial y^2} > 0 \ . \qquad (3.27)$$

If the diffusion coefficients are independent of concentration, then the deposition rate is proportional to the second derivative of the concentration, which is significant

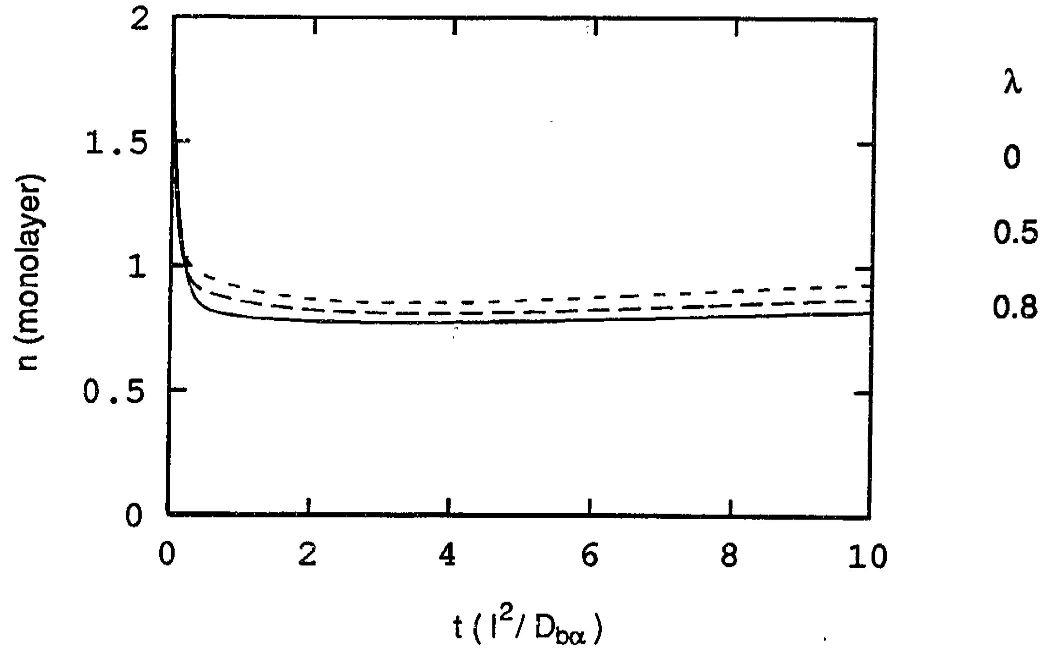

Figure 3-13: Calculated quantities of α in the grain boundary slab as functions of time for different λ values.

only in the transient period. However, since the transient period itself is of negligible effect, the second term is unimportant.

Fig. 3-13 shows the quantity of α atoms in the grain boundary as a function of time. In the transient period, the grain boundary loses about half of the α atoms originally stored. As discussed in Section 3.1.1, this transient period is of little importance in the accumulation process in the quasi-steady state that follows. The effects of the concentration dependence of the diffusion coefficients is even weaker. We thus conclude that the grain boundary as source or sink is of negligible significance.

3.1.8 Effects of DIGM

As reviewed in Section 2.2.6, DIGM occurs inevitably for chemical diffusion processes. This problem, although poorly understood, could be described phenomenologically by modifying our diffusion model to incorporate the migration of the boundaries. According to Cahn's model [48], the diffusion in the boundary is described by

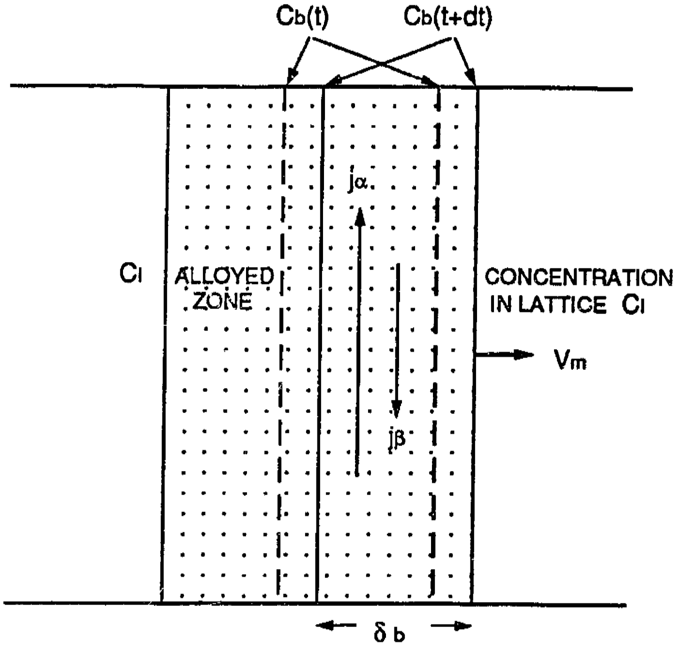

Figure 3-14: Schematic diagram of the DIGM process. The grain boundary is moving towards right with velocity v_m leaving behind an alloyed zone.

$$\frac{\partial C_{b\alpha}}{\partial t} = \frac{\partial}{\partial y}(D_{s\alpha}\frac{\partial C_{b\alpha}}{\partial y}) - \frac{v_m}{\delta_b}(C_{b\alpha} - C_{l\alpha}) \; , \tag{3.28}$$

$$\frac{\partial C_{b\beta}}{\partial t} = \frac{\partial}{\partial y}(D_{b\beta}\frac{\partial C_{b\beta}}{\partial y}) - \frac{v_m}{\delta_b}(C_{b\beta} - C_{l\beta}) \; , \tag{3.29}$$

where v_m is the migration velocity of the boundary as illustrated in Fig. 3-14, which could be independently determined, and C_l is the concentration in the adjacent bulk toward which the boundary is migrating. To estimate the error that could be possibly introduced in the diffusion measurement by DIGM, we calculated the accumulation for migration velocities: 0, 0.01, and 0.05 Å/s (Fig. 3-15). The velocity 0.01 Å/s is approximately the value measured by Pan and Balluffi [49] in random boundaries in the Au/Ag system. The velocity for the symmetric tilt boundaries used in this experiment should be smaller than that in random boundaries. It is then obvious that the DIGM effects should be very small.

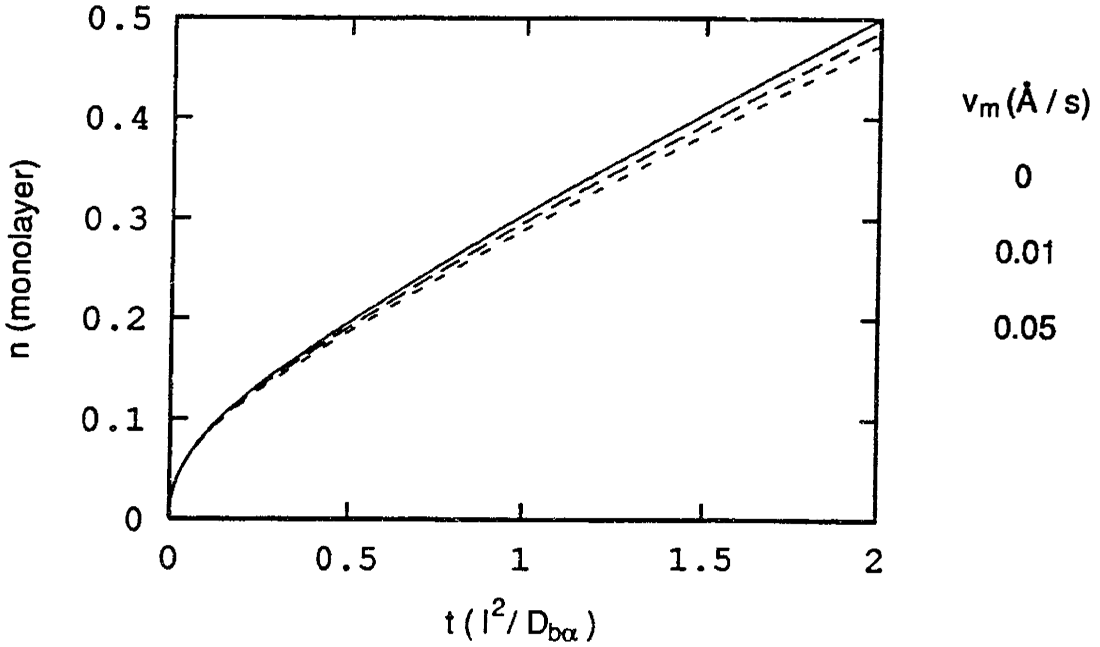

Figure 3-15: Calculated surface accumulation profiles for different values of migration velocities.

From the above discussion, we can summarize several basic features predicted by the diffusion model as following:

After the start of diffusion, the system very quickly settles itself into a quasi-steady state, in which the atoms diffuse through the grain boundaries and spread on the surfaces uniformly. At the early stage of diffusion, the source surface acts as a virtually constant source, and the accumulation rate for the faster diffusion α atoms is approximately constant and is insensitive to the surface accumulation mechanism, the surface/boundary segregation ratio or the composition dependence of the diffusivity. The grain boundaries serve primarily as diffusion paths, and their contribution to the source or sink of diffusion material is insignificant even with DIGM present.

3.2 Experimental Procedures

3.2.1 Diffusion Specimen Preparation

All the specimens used in this experiment possessed symmetric [001] tilt grain boundaries of specific misorientations. They were silver-gold double-layered thin films with an array of parallel grain boundaries of the same kind running perpendicular to the surfaces. The thickness of each layer was about 1000 Å, and the spacing between adjacent grain boundaries was 2μm.

The specimen preparation method is illustrated schematically in Fig. 3-16. First, a (001) single crystal Au film is epitaxially grown on a NaCl substrate as shown in Fig. 3-16a. A bicrystal is then prepared by welding two (001) single crystal Au films together face-to-face at the desired crystal misorientation (Fig. 3-16b). Then, by use of high resolution lithography techniques, an array of parallel troughs is produced as shown in Fig. 3-16c. Next, a layer of Au is epitaxially deposited to produce the configuration illustrated in Fig. 3-16d. The specimen is then ion-milled from the other side in order to remove all the material up to the dashed line in Fig. 3-16d to produce the configuration in Fig. 3-16e. Next, successive layers of Ag and Au are epitaxially deposited on the newly ion-milled surface as shown in Fig. 3-16f. Finally, the latest deposited Au layer is separated away by dissolving the thick Ag layer in nitric acid, and a thin layer of Ag of controlled thickness is epitaxially deposited on it to produce the final diffusion specimen in Fig. 3-16g.

During the development of the above method, a considerable amount of difficulty was encountered. These problems as well as their solutions are discussed when the detailed procedure is described below.

Single Crystal Film Epitaxy

(001) single crystal Au films of thickness about 1000 Å are obtained by thermal evaporation of Au directly on rocksalt substrates. First, the NaCl substrates about 10 × 10 × 2 mm are produced by cleaving (on the (001) faces) NaCl single crystal blocks. These substrates are irradiated with 400 eV low energy electrons at 320°C in

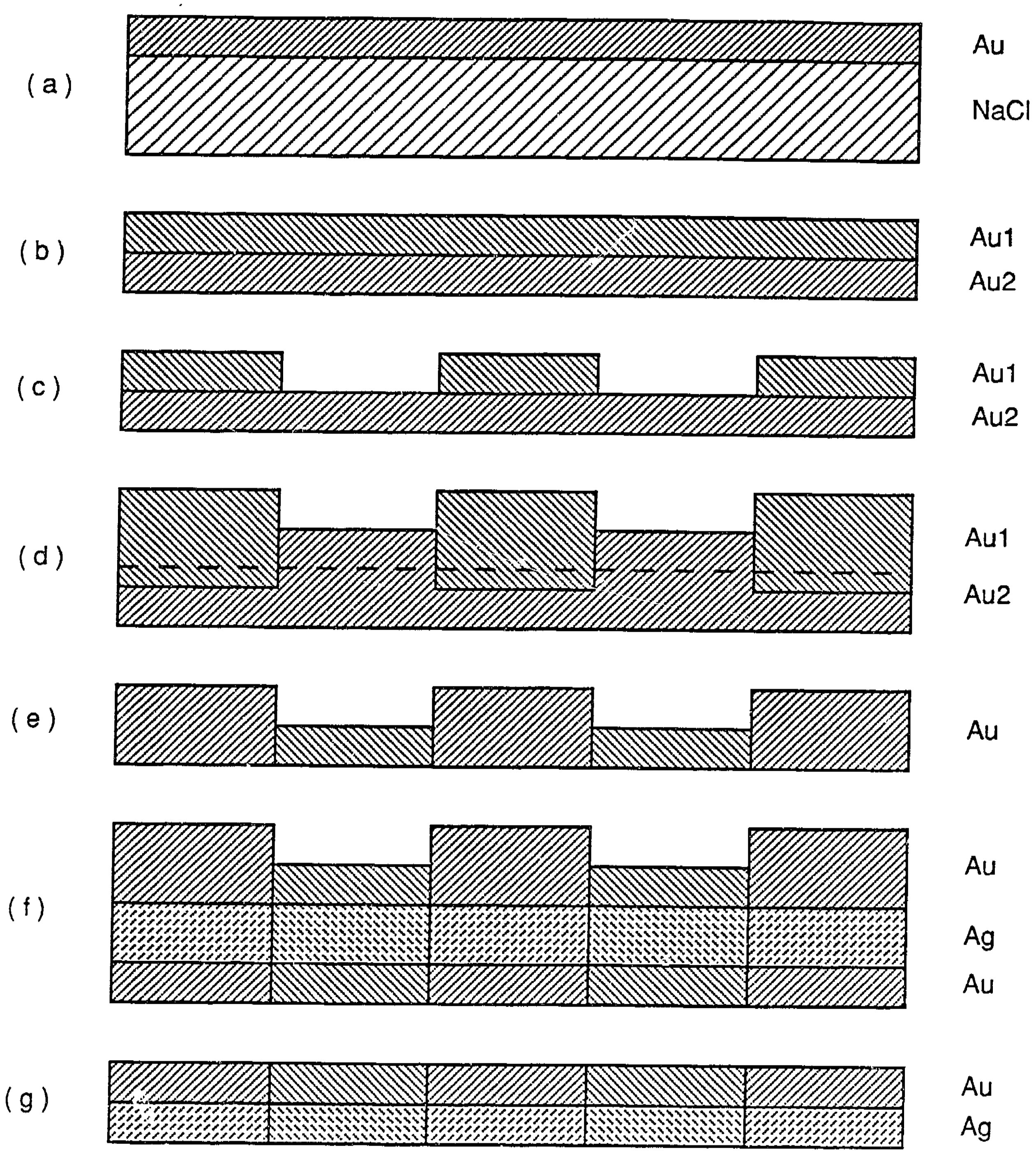

Figure 3-16: Schematic diagram of diffusion specimen preparation method.

high vacuum (low 10^{-7} torr range) for about 30 minutes. Finally, a predetermined amount of Au is evaporated from a resistively-heated tungsten boat with about a 100 Å/s deposition rate. An important measure of the single crystal Au film quality is the twin density, which directly determines the twin density in the final diffusion specimen. The diffusion along twin boundaries or stacking faults is considerably slower than in ordinary boundaries and therefore does not contribute significantly to the surface accumulation. However, these twins could intersect the grain boundaries under study and change the structure of the boundary from that desired.

Bicrystal Film Welding

Bicrystal Au films are produced using the hot pressing method developed by Schober and Balluffi [50]. Briefly, two gold films still attached to their substrates are placed face-to-face at the desired crystal misorientation. The two crystals are then annealed in air at 300°C under moderate pressure for about one hour. TEM observations show that an appreciable fraction of the overlapped area is welded.

Bicrystal Film Abstraction

The welded bicrystal film is laid on a piece of polished Si wafer for the lithography process. The smoothness of the film is crucial because any wrinkle can significantly degrade the uniformity of the photoresist, and eventually affect the boundary straightness. To achieve the required smoothness, the following method was developed. First, the NaCl substrates are dissolved in DI water and the film is cleaned by changing the water several times. Then the film is floated on the surface with the help of a piece of analytic paper. After the film is gradually stretched flat by the water surface tension, it is scooped up on a small piece of Si wafer. Before the wafer under the film dries up, the wafer is put on a photoresist spinner so that the rotation axis passes through the center of the film. Then the spinner is turned on and is immediately accelerated to a speed of 8000 rpm. While the water is spun away, the film is stretched to its limit and sticks to the wafer surface wrinkle-free.

High Resolution Lithography

The lithography process involves the following steps:

Sample Dehydration Baking The sample (Au bicrystal film attached to a Si wafer) is baked at 300°C for about two hours. The time used here is significantly increased compared to the normal 30 minutes [51] because the purpose of this step is not only to dehumidify the sample surface in order to improve the photoresist bonding, but also to strengthen the bonding between the Au film and the wafer, which is very important for the photoresist developing step later.

Photoresist Coating Photoresist of type KTI-820-20 is spin-coated on the sample at a speed of 5000 rpm for 30 seconds on a spinner to produce a photoresist layer about 6000 Å thick. Then the sample is soft baked at 95°C for 25 minutes.

Photoresist Exposure The sample is placed on the stage of a photoresist aligner. UV light is directed on the photoresist through a mask so that the pattern on the mask is replicated on the sample. The mask with a grating pattern of period 4μm is used to generate the parallel grain boundaries. Obviously, to have symmetric tilt boundaries, the sample has to be precisely oriented relative to the grating pattern. To do so, a micro-protractor pattern is added on the mask and then one of the straight edges of the Au film is aligned with one of the radiant lines on the protractor that represents the desired angle. By using this method, a precision of 0.5° is routinely achievable.

Photoresist Development The photoresist is developed so that the exposed part dissolves away and a parallel array of unexposed photoresist is left on the Au film.

Ion Milling The troughs of material that are unprotected by the photoresist are milled away. A low ion energy of 500 eV is used in order to minimize surface damage (about 20 Å depth at 500 eV [52]). In this step, a single crystal film of 1000 Å is placed beside the bicrystal film to monitor the sputtering rate. It is observed that a thin layer of Au is redeposited on the sidewalls of the photoresist during sputtering.

Photoresist Stripping The photo resist lines are then stripped away by using an O_2 plasma etcher. The redeposits have to be removed by a brief sputtering process.

Au Layer Deposition An approximately 5000 Å thick layer of Au is deposited on the sample after 30 minutes of annealing at 400°C to reduce the surface damage. The reason for depositing such a thick layer is as follows: After the deposition, the film has to be removed from the Si wafer and turned upside down for the next step. However, as the film sticks to the wafer firmly, it is extremely difficult to take it off if the film is thin.

Au Layers Separation After the film is turned upside down, it is sputtered again. A layer of Ag of about 2μm thickness and a Au layer of about 1100 Å thickness are then successively deposited. To reduce the grain boundary interdiffusion at this stage, the deposition temperature is kept as low as possible ($\sim$ 50°C). The thin Au film is separated away by floating it on the surface of 30% nitric acid while the Ag layer is dissolved away. In this process, the thick Au layer firmly adheres to the substrate which is a piece of Si wafer with a thin layer of Cr on its surface to increase the Au/substrate bonding.

Formation of Final Specimen The Au film obtained in the above step is carefully cleaned in DI water. It is then sputtered from the separation side to further clean the surface and to reduce the thickness to about 1000 Å. The film is then annealed at 500°C for about 30 minutes for high angle boundaries and for up to 2 hours for low angle boundaries to improve the grain boundary quality. Finally, about 1000 Å thick of Ag layer is epitaxially deposited on the sputter-cleaned surface at 100°C to form the double-layered diffusion couple.

3.2.2 Specimen Mounting and Characterization

After the diffusion couple is manufactured, it is mounted on a TEM grid and is then characterized by using TEM. Several factors have to be considered for choosing the best TEM grid:

(1) Contamination should not be introduced to the diffusion couple from the grid.

A gold grid is uniquely qualified because it brings in neither a new metal component nor oxides to the system.

(2) Heat conductance should be maximized so that during the diffusion measurement, the film is heated uniformly and the heat generated by the electron beam can dissipate quickly. Clearly, a fine grid is preferred over a coarse grid.

(3) The grid should not block those Auger electrons that will otherwise be collected by the analyzer. This criterion limits the fineness of the grid.

(4) For diffusion measurement, SEM is used to relocate the best area on the film that has been found with TEM. A grid with some kind of coordinate system is ideal for this purpose.

Combining the above considerations, a type of 300 mesh (each open area on the grid is about $70 \times 70\mu$m) pin-pointer Au grid is chosen for this experiment.

The purpose of TEM characterization is to check the specimen quality and to select the best area for the diffusion measurement. The quality of a particular area has two aspects: the boundary quality and the film quality. The boundary quality is determined by the following factors:

(1) Boundary straightness. A lack of straightness has several effects. First, it deviates the boundary plane from the desired geometry. Secondly, it increases the net length of the boundary. Finally, it introduces a large number of grain boundary steps which could change the diffusion behavior.

(2) Boundary grooving. Both chemical etching and thermal annealing could cause boundary grooving which introduces an error in the boundary diffusion distance, therefore causing inaccuracy in the derived diffusivity.

(3) Boundary defects. It is noticed that sometimes the twin density at the boundary is considerably higher than the average density in the film. Although twin boundaries and stacking faults by themselves do not contribute much to the diffusion circuit [40], twins at the grain boundary do change the geometry of the boundary and therefore change the diffusion characteristics.

While the boundary quality is rather subtle to determine, the film quality is apparent by using TEM.

During the specimen preparation process, any step can introduce defects into the film. Large cleavage steps cause cracks in the initial single crystal film that will propagate to the final specimen. Small particles from the air produce holes or polycrystal patches in the film. These defects could drastically change the diffusion behavior. Fortunately, they can be easily detected with TEM, and thus can be completely avoided.

A typical qualified area is shown in Fig. 3-17a, and a section of grain boundary with grain boundary edge dislocations is shown in Fig. 3-17b.

After structural examination by TEM, the specimen is placed in the scanning Auger microscope (SAM) for the diffusion studies. At the same time, the composition of the film is closely monitored. While no other impurity inside the films can be detected by AES, the gold layers were found to contain a trace amount of silver.

3.2.3 Auger Electron Spectrometer

The diffusion measurements were made in a Perkin-Elmer 590 SAM. As shown in Fig. 3-18, the vacuum chamber houses the scanning Auger spectrometer, the sample stage, a scanning ion gun and a SEM analyzer. The main body of the Auger spectrometer is a cylindrical mirror electron energy analyzer with a coaxial scanning electron gun. The electron gun is capable of producing a beam current ranging from 20 nA to 10μA with energy tunable from 2 keV to 15 keV. The electron beam diameter was about 2μm, which determines the resolution of the SEM.

The sample stage consists of six independent heaters mounted on a circular base which is attached to a manipulator. The manipulator is capable of four modes of motion, namely, three translational mode and one rotational mode. The rotation transports each individual heating block in front of the analyzer, and the translations position the specimen with about 5μm resolution. To implement the desired diffusion scheme discussed in Chapter 3, which requires either the front or the back side of the specimen to face either the Auger analyzer or the ion gun, a novel rotary heating module as shown in Fig. 3-19 was specially developed to introduce an additional rotational mode. This device consists of two parts, a frame piece and a cylinder

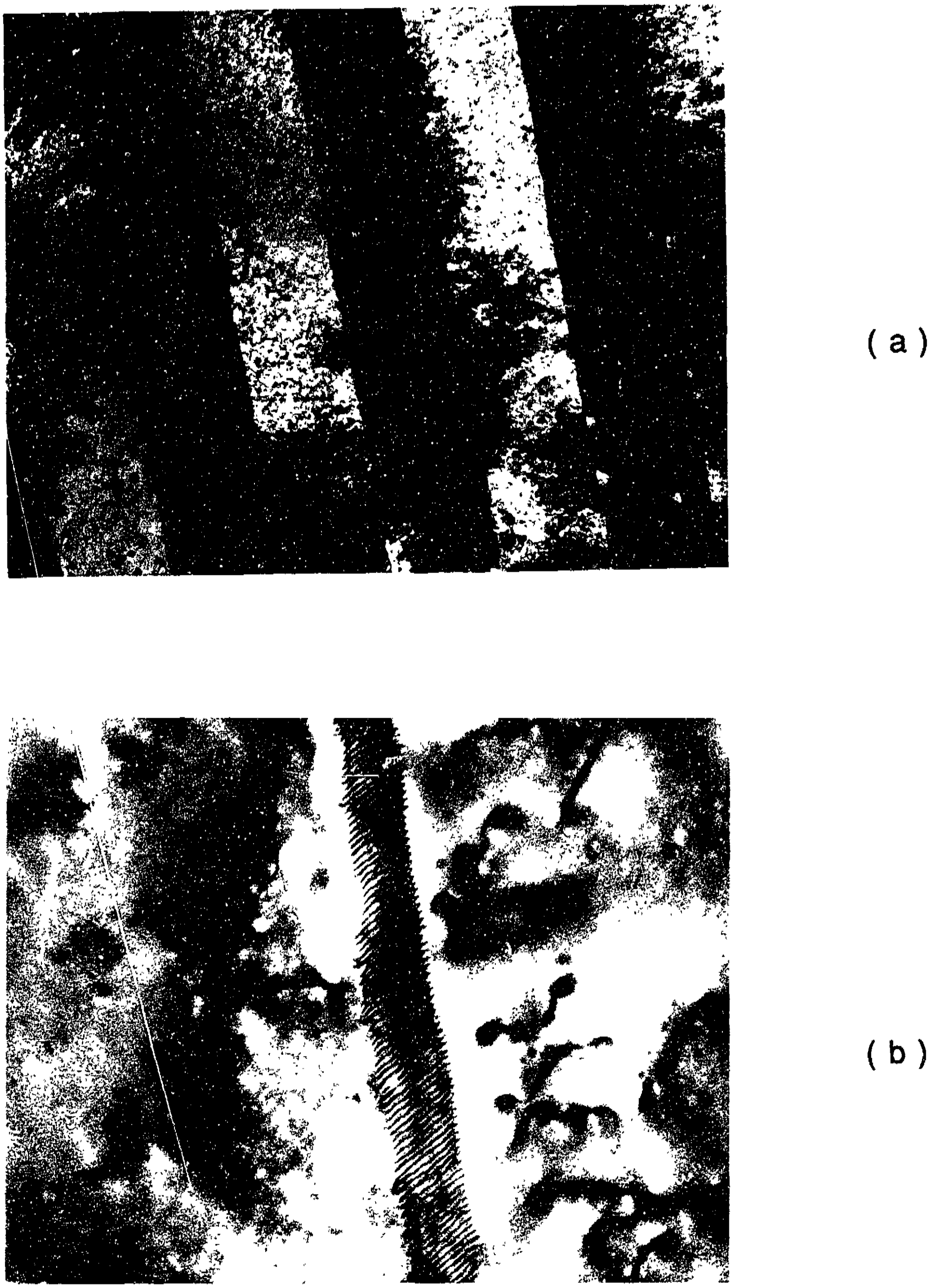

Figure 3-17: Multi-crystal diffusion specimen. (a) Top view of a typical area; (b) Grain boundary edge dislocations running parallel to the tilt axis.

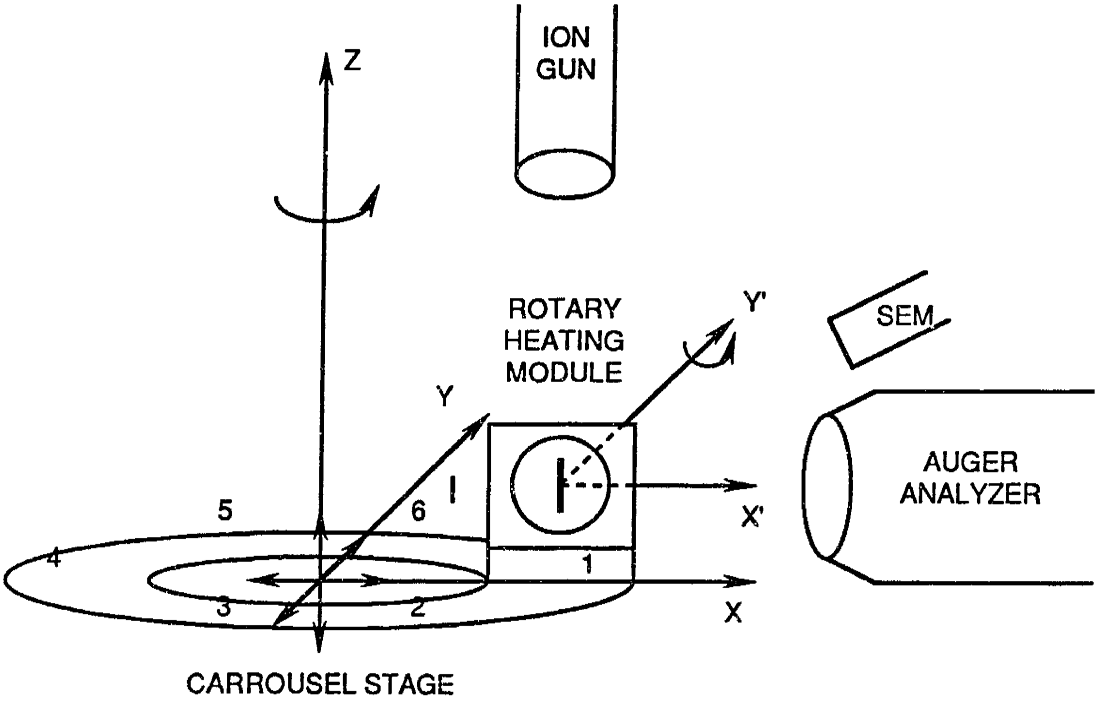

Figure 3-18: The experimental arrangement inside the vacuum chamber.

piece. The frame with a polished inner cylindrical surface is firmly mounted on the heating block. The cylinder piece is well fitted to the frame to allow smooth rotation and adequate heat conduction. The specimen is mounted at the center of the cylinder which has 120° openings on both sides.

The frame and the cylinder are made of pyrolytic graphite and molybdenum respectively to ensure good thermal conduction and to reduce redeposition during ion sputtering. Experimental test and theoretical estimates show that the real specimen temperature is within 2°C of that measured.

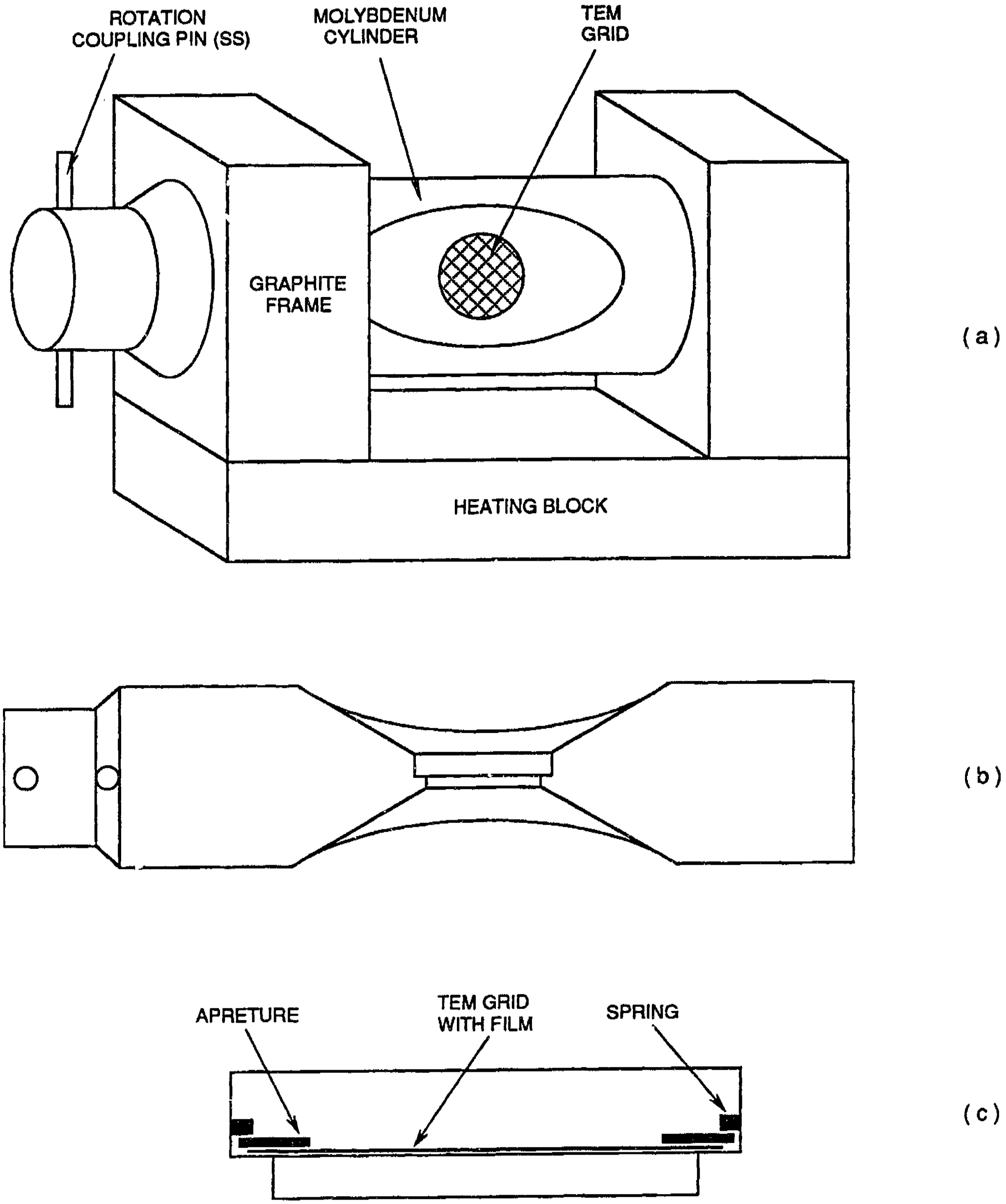

Figure 3-19: Diagrams of the rotary heating module. (a) The module mounted on a heating block; (b) The cylinder with a hole at the center; (c) A TEM grid mounted at the hole by using an aperture and a spring.

The ion gun is primarily used to sputter-clean both sides of the specimens prior to each diffusion measurement and to remove silver on the gold surface and gold on the silver surface between successive diffusion anneals of the same specimen. The ionization chamber is differentially pumped by a turbomolecular pump so that during sputtering, the vacuum in the chamber is usually kept below 1×10^{-9} torr. For cleaning purposes, the ion gun is set at 1000 V and 3 × 3 mm rastering area, which generates a sputtering rate of about 2 Å/s.

The vacuum system is equipped with a 220 l/s ion pump and a TSP with LN_2 cooling. After baking, the chamber pressure is generally below 5×10^{-10} torr. During the diffusion experiment when the sample is heated and all apparatus inside the chamber turned on, it remains below 1×10^{-9} torr, so that the sputtered surface maintained clean for up to one hour.

A typical diffusion measurement starts with the relocation of the favored area that has been chosen by using TEM. On the SEM video screen, the Au grid could be seen clearly and the favored area is positioned directly in front of the analyzer. By maximizing the elastic peak of the back scattered electrons, the distance between the specimen and the analyzer is optimized. Now, the specimen is heated to the desired temperature. Next, the front and the back surfaces of the specimen are turned to face the ion gun and sputter-cleaned successively. The gold surface is then turned perpendicular to the electron beam for Auger analysis. The electron gun is normally operated with an electron beam of 5 keV and 100 nA and a rastering area of about $30 \times 30 \mu m$ (each open area on the grid is about $70 \times 70 \mu m$). During the diffusion runs a multiplex control is employed so that only the energies adjacent to the Auger peaks of interest are scanned. After sufficient data are accumulated for the initial curve slope determination, the specimen is sputter-cleaned for another run.

3.2.4 Calibration of Auger Signals

Although the Auger electron spectroscopy of the Au-Ag system has been extensively studied [54, 55, 56, 53], there is no uniquely preferred method to calibrate the signals due to the differences in instrumentation and the nature of the experiment.

In this experiment, the data were collected over a period of several months, during which the instrumental parameters had certain variations. To minimize the instrumental errors, the Auger signals measured from the accumulation surface were always calibrated with respect to the Auger signals from pure silver and gold standards.

At the early stage of the diffusion process, the amount of accumulated Ag is a fraction x of a monolayer. If the surface segregation factor is relatively large, most of the Ag atoms will spread out on top of the Au surface and effectively cover the fraction x of the total area. The intensity of the major silver peak at 356 eV is

$$I_{356} = xK_{356} \, , \tag{3.30}$$

where K_{356} is a complex constant incorporating all parameters fixed during the measurements, e.g., primary beam I_p, Auger transition probability, spectrometer properties and others. The Auger peak intensity from a pure Ag bulk is

$$\begin{aligned} I^0_{356} &= K_{356}(1 + e^{-1/\lambda_{356}\cos\omega} + e^{-2/\lambda_{356}\cos\omega} + \cdots) \, , \\ &= K_{356}\frac{1}{1-\exp(-1/\lambda_{356}\cos\omega)} \, , \end{aligned} \tag{3.31}$$

where λ_{356} is the electron escape depth at 356 eV in terms of monolayers and ω is the emitting angle of the Auger electrons that will be collected by the analyzer. Combining the above equations, we have

$$I_{356} = xI^0_{356}(1 - e^{-1/\lambda_{356}\cos\omega}) \, , \tag{3.32}$$

or

$$x = \frac{I_{356}}{I^0_{356}}\frac{1}{1-\exp(-1/\lambda_{356}\cos\omega)} \, . \tag{3.33}$$

Let

$$C_{356} = \frac{1}{1-\exp(-1/\lambda_{356}\cos\omega)} \, , \tag{3.34}$$

we have

$$x = C_{356} \left(\frac{I_{356}}{I_{356}^0} \right) . \tag{3.35}$$

Similarly, the Au 69 eV peak can be monitored simultaneously and the intensity can be expressed as

$$I_{69} = I_{69}^0 - x I_{69}^0 (1 - e^{-1/\lambda_{69} \cos\omega}) , \tag{3.36}$$

or

$$x = C_{69} \left(1 - \frac{I_{69}}{I_{69}^0} \right) , \tag{3.37}$$

where

$$C_{69} = \frac{1}{1 - \exp(-1/\lambda_{69} \cos\omega)} . \tag{3.38}$$

For the single path analyzer employed, the acceptance angle $\omega = 35°$. Using additional standard values

$$\begin{aligned} \lambda_{356} &= 8 \text{ Å} &&= 4 \text{ monolayers} , \\ \lambda_{69} &= 4 \text{ Å} &&= 2 \text{ monolayers} , \end{aligned}$$

we get

$$C_{356} = 3.8 , \qquad C_{69} = 2.2 .$$

The above analysis assumes the accumulated Ag atoms just spread out on the top of the surface, which corresponds to the case that the surface segregation is strong. For the Au/Ag system, the segregation is relatively weak, and therefore the Ag distribution in other than the top atomic layer should also be considered. Assume the surface slab consists of 2 atomic layers m_1 and m_2. During the period that the total accumulation is less than 1 monolayer, the first atomic layer below the slab m_3 also needs to be considered. Letting the concentration in m_1, m_2 and m_3 be x_1, x_2 and x_3 respectively, we have

$$x = x_1 + x_2 + x_3 , \tag{3.39}$$

$$x_2 = \frac{1}{s_{sAg}} x_1 , \tag{3.40}$$

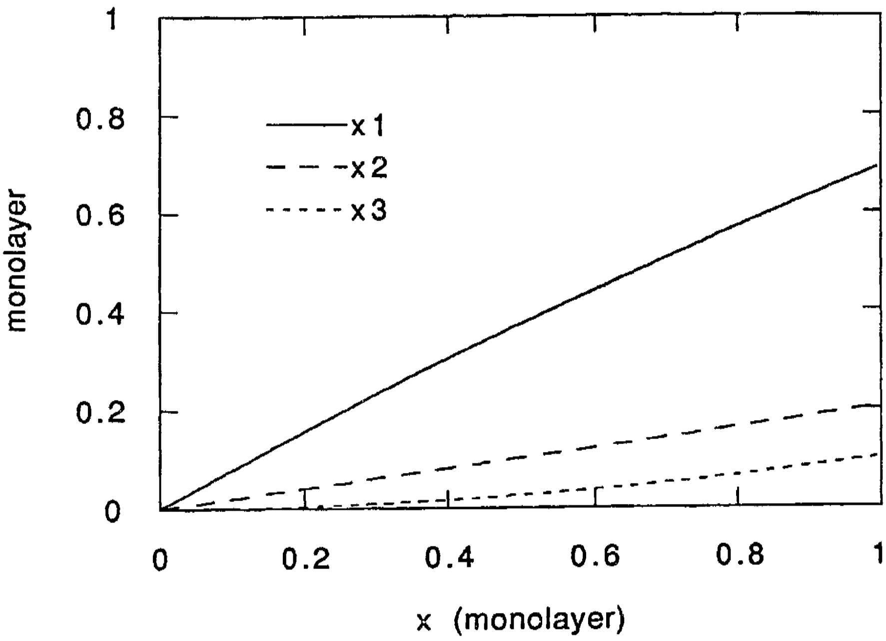

Figure 3-20: Calculated x_1, x_2 and x_3 as functions x for $s_{sAg} = 4.0$.

$$\frac{dx_3}{dt} = x_2 \frac{dx}{dt} , \tag{3.41}$$

where s_{sAg} is the effective surface segregation factor of Ag in the Au/Ag system. Figure 3-20 shows an example of x_1,x_2 and x_3 solved for $s^0_{sAg} = 4$ as functions of x. The Ag 356 eV and Au 69 eV peak intensities should then be expressed as

$$I_{356} = I^0_{356}\left(1 - e^{-1/\lambda_{356}\cos\omega}\right)\left(x_1 + x_2 e^{-1/\lambda_{356}\cos\omega} + x_3 e^{-2/\lambda_{356}\cos\omega}\right) ; \tag{3.42}$$

$$I_{69} = I^0_{69} - I^0_{69}\left(1 - e^{-1/\lambda_{69}\cos\omega}\right)\left(x_1 + x_2 e^{-1/\lambda_{69}\cos\omega} + x_3 e^{-2/\lambda_{69}\cos\omega}\right) . \tag{3.43}$$

By using the above equations, the Auger intensities are calculated and plotted in Fig. 3-21. Clearly, the relationship between the accumulated quantity x and the measured intensities I_{356} and I_{69} is still approximately linear. Consequently, if the accumulation rate of Ag is constant, I_{356} should increase while I_{69} should decrease linearly with time.

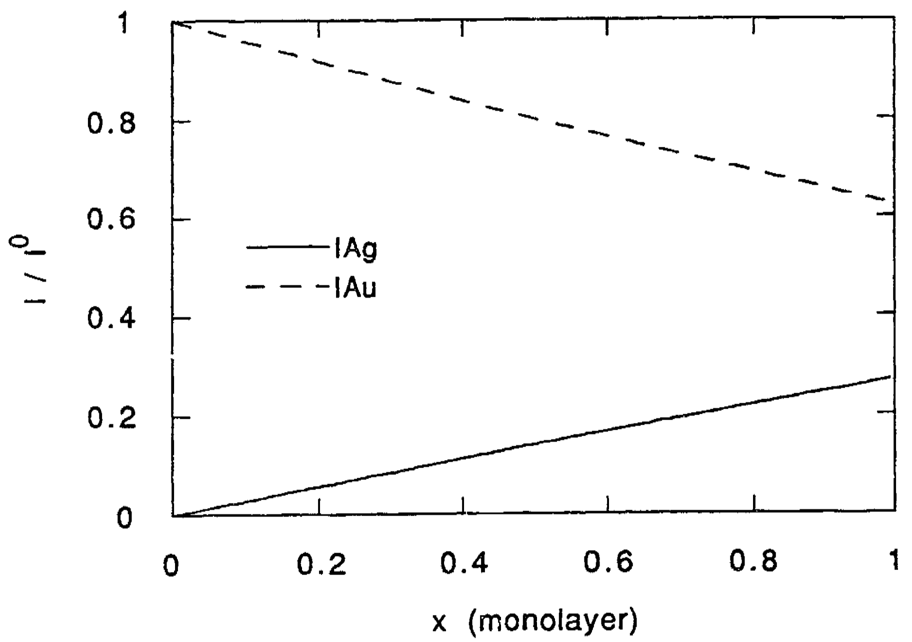

Figure 3-21: Calculated relative Auger intensities I_{356}/I^0_{356} and I_{69}/I^0_{69} as functions of x for $s_{sAg} = 4.0$.

Define the normalized intensities as

$$\mathcal{I}_{356} \equiv C_{356}\left(\frac{I_{356}}{I^0_{356}}\right) ; \tag{3.44}$$

$$\mathcal{I}_{69} \equiv C_{69}\left(1 - \frac{I_{69}}{I^0_{69}}\right) . \tag{3.45}$$

Therefore, during the period that $x_1 + x_2 + x_3 < 1$, we have

$$\mathcal{I}_{356} = x_1 + x_2 e^{-1/\lambda_{356}\cos\omega} + x_3 e^{-2/\lambda_{356}\cos\omega} ; \tag{3.46}$$

$$\mathcal{I}_{69} = x_1 + x_2 e^{-1/\lambda_{69}\cos\omega} + x_3 e^{-2/\lambda_{69}\cos\omega} . \tag{3.47}$$

By solving the above equations, $\mathcal{I}_{358}$ and $\mathcal{I}_{69}$ can be obtained as functions of x for different effective segregation factors, and then the relationship between their time derivatives and dx/dt can be established as shown in Fig. 3-22 for the early period of diffusion. By using a set of accumulation profiles measured at different temperatures, the effective segregation factor can be obtained as a function of temperature. Briefly, from experimental data, $d\mathcal{I}_{358}/dt$ and $d\mathcal{I}_{69}/dt$ are obtained by using Eq. 3.44 and Eq. 3.45. The dotted horizontal lines in Fig. 3-22 represent a pair of such experimentally obtained values. Each line intersects with the calculated curves and generates several possible dx/dt corresponding to different $s_{s\alpha}$'s. However, the accumulation rates from $\mathcal{I}_{358}$ and $\mathcal{I}_{69}$ should be the same and should be consistent with the same s_{sAg}. This criteria leads to a unique s_{sAg} for a certain temperature. The effective segregation factor obtained in such fashion is plotted in Fig. 3-23. Clearly, the effective segregation factor s_{sAg} decreases with increase of temperature as expected from Eq. 3.22. However, the values of s_{sAg} at the low temperature end are considerably larger than those previously measured or calculated [46, 56, 57], which suggests that the equilibrium in the surface slabs at low temperatures may not be completely established so that a larger fraction of Ag atoms stays on top of the surface resulting in relatively larger effective segregation factors.

With the above knowledge, the Ag accumulation rate can be obtained by using $\mathcal{I}_{356}$ only. It should be noted that both the model we used to describe the accumulation process and the model that relates the atomic concentration and the Auger intensities may have certain systematic errors. However, these systematic errors should be the same for all of the boundaries studied in this experiment because all of the accumulation surfaces involved are (001) surfaces.

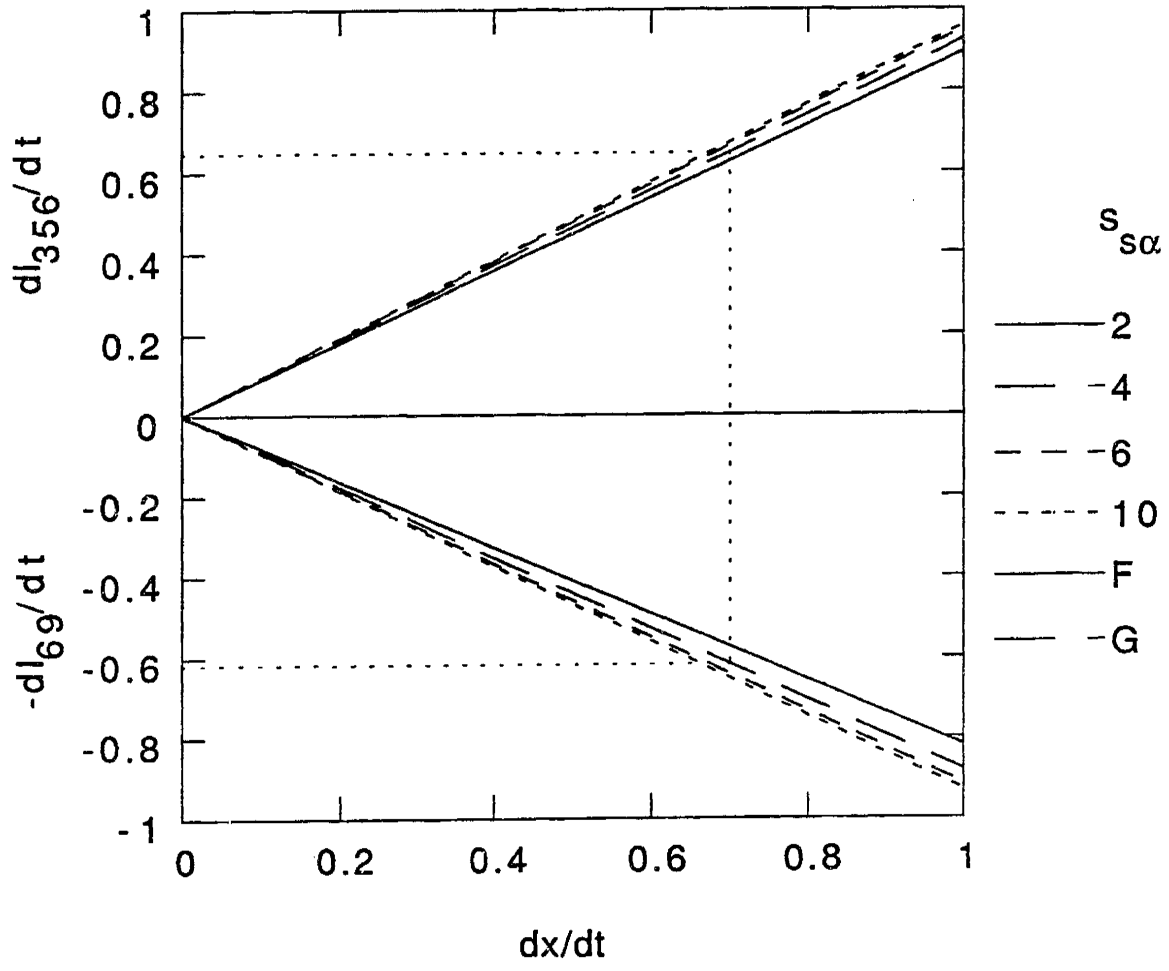

Figure 3-22: Calibration curves used to obtain s_{sAg} and dx/dt from experimental data.

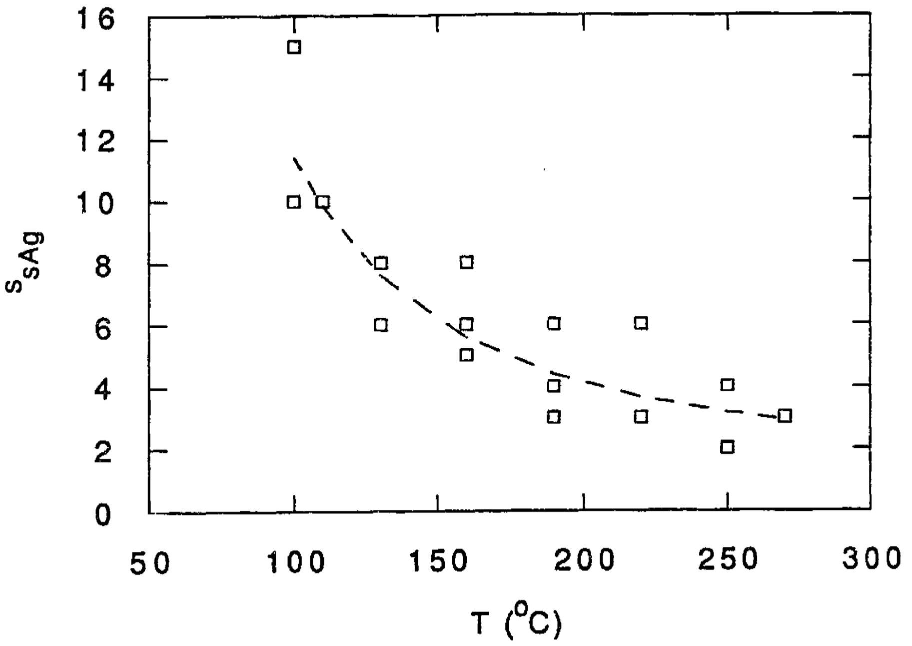

Figure 3-23: Temperature dependence of the effective surface segregation factor s_{sAg} obtained experimentally.

Chapter 4

Experimental Results and Discussion

4.1 General Behavior of the Diffusion System

Silver Auger signals from the accumulation surface were observed to increase with time after the source surface and the accumulation surface were in turn sputter-cleaned. The time dependence of the normalized intensity $\mathcal{I}_{356}$ is shown in Fig. 4-1 for a $\Sigma 5\,(310)$ boundary at 190°C. Clearly, the rate of Ag accumulation was highest initially and gradually slowed down as a function of time.

The time, $t = 0$, was defined as the instant the measurement was started. It is noticed that at $t = 0$, the function $\mathcal{I}_{356}(t)$ dose not equal to 0. Several factors may have contributed to this observation:

(1) The measurement started a short time after the sputtering on the accumulation surface was stopped, because the accumulation surface had to be turned perpendicular to the electron beam after the sputtering (see Section 3.2.3). As a result, the accumulation process had already started a short while before $t = 0$.

(2) According to the diffusion model (see Section 3.1), at the beginning of the diffusion process, the system undergoes a transient period during which the Ag atoms stored in the boundary diffuse out rapidly and thus contribute to a rapid increase of Ag concentration on the accumulation surface. The fact that we did not observe such

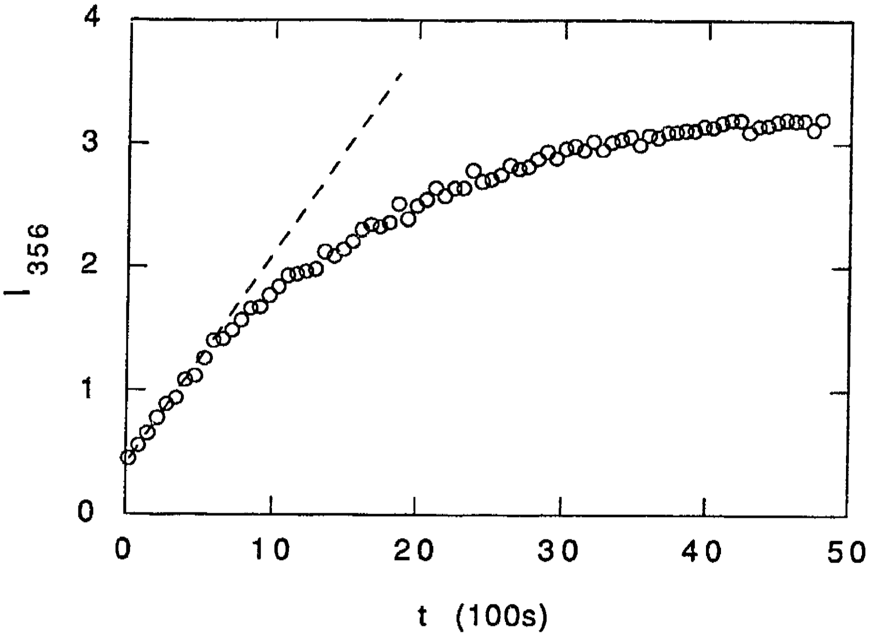

Figure 4-1: Surface accumulation profile (normalized intensity) for a $\Sigma 5\,(310)$ boundary at 190°C. The dashed line represents the constant accumulation rate at the early stage of diffusion.

a transient period in the measurement confirms that such a period is indeed very short as predicted by the model.

(3) To preserve the specimen for consecutive measurements, each sputtering process was limited to the removal of a layer of material less than about 30 Å thick from the accumulation surface. Due to the well-known artifacts associated with the sputtering process, the efficiency of cleaning decreases with decrease of surface impurity concentration. Consequently, the accumulation surface was not completely cleaned, although the actual accumulated Ag distribution was much thinner than 30 Å.

Fortunately, the slight residual concentration of Ag on the surface at the beginning should have little effect on the diffusion behavior later observed in the quasi-steady state.

Of primary interest was the surface accumulation rate which can be related to the grain boundary diffusion rate. Although the full range of the accumulation profile contains this information, the data obtained in the later period are difficult to interpret due to the following reasons:

(1) As described in the diffusion model, the surface accumulation rate in the later stage is severely affected by a number of factors including the surface/boundary segregation ratio, the detailed surface accumulation mechanism as well as the effects of interdiffusion of Ag-Au in the boundaries. All these factors are not well understood and currently impossible to measure independently. Therefore, it is impossible to obtain quantitative information about the grain boundary diffusion properties from the measured accumulation rate in the later period.

(2) The calibration method described before is most reliable when the accumulated amount of Ag is relatively small, so that only a very few atomic layers near the surface need to be analyzed.

(3) Experimentally, at relatively low temperatures, saturation takes a long period of time during which the accumulation surface is inevitably contaminated by the residual gases in the vacuum chamber, especially hydrocarbons. This contamination is known to reduce the surface diffusivity significantly and thus change the diffusion behavior.

On the other hand, the diffusion model predicts that the accumulation rate in the early stage of diffusion should be rather insensitive to the complicated effects due to segregation, the accumulation mechanism and interdiffusion, and therefore can be related to the grain boundary diffusion directly. In fact, it is clearly observed in the measurements that the Ag accumulation rate was virtually constant in the early stage of diffusion (Fig. 4-1 and 4-2). This result was predicted by the diffusion model and indicates that:

(1) The effective surface concentration of Ag near the boundary exit regions is small enough in the early stage of the diffusion to preserve the constant accumulation rate. This implies that the Ag atoms spread out on the surface fairly uniformly and did not pile up near the exit regions, which is consistent with the fact that surface diffusion is generally much faster than grain boundary diffusion.

(2) The source surface remains pure in Ag to a large extent, so that it acts as an effective constant source. This is confirmed by the observation that the Au signals from the source surface (which was measured intermittently) remained at the

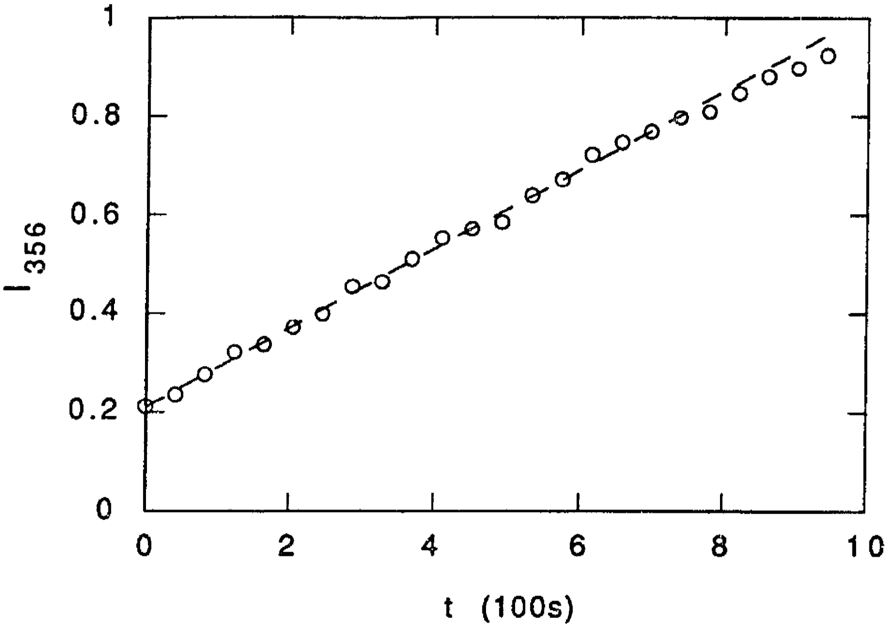

Figure 4-2: Surface accumulation profile (normalized intensity) illustrating the constant accumulation rate at the early stage of the diffusion.

background noise level during the period that the Ag accumulated linearly on the accumulation surface. This observation serves as strong evidence that the Au atoms diffuse more slowly than the Ag atoms. It is difficult, however, to make a quantitative estimate of the D_{bAg}/D_{bAu} ratio because the Au atom flux is very small and it may be strongly influenced by DIGM and possibly other effects as discussed in Section 3.1.

The above results have verified the assumptions made in the diffusion model and are in complete agreement with the predictions made by the model. As a result, it is concluded that this model describes the diffusion system adequately.

We now proceed to derive a formula that will relate the surface accumulation rate to the grain boundary diffusion parameter. Due to conservation of matter, the surface accumulation rate should equal the atomic current at the exit of the grain boundary:

$$\frac{dQ}{dt} = \frac{\delta_b j(l)}{b}, \qquad (4.1)$$

where Q is the surface density of accumulated Ag atoms, and $j(l)$ is the Ag flux at the boundary exit. Since the grain boundary effect as a sink or source is negligible in the quasi-steady state period, to a good approximation, $j(y)$ should be constant along the boundary, therefore

$$j(l) = j(y) = D_{bAg} \frac{dC_{bAg}}{dy} , \qquad 0 < y < l . \tag{4.2}$$

Multiplying both side by dy and integrating from the entrance to the exit of the boundary, we get

$$j = \frac{1}{l} \int_{C_{bAg}(0)}^{C_{bAg}(l)} D_{bAg}\, dC_{bAg} . \tag{4.3}$$

The concentration of Ag in the boundary at the entrance and exit can be related to the surface concentrations:

$$C_{bAg}(0) = k_{Ag} C_{sAg1} ; \tag{4.4}$$

$$C_{bAg}(l) = k_{Ag} C_{sAg2} . \tag{4.5}$$

At the beginning, C_{sAg2} is very small compared to the saturation value, so that $C_{bAg}(l) \approx 0$, and C_{sAg1} is pure in Ag, so $k_{Ag} \approx 1$ and $C_{bAg}(0) = 1$. Therefore, Eq. 4.3 becomes

$$j = \frac{1}{l} \int_0^1 D_{bAg} dC_{bAg} \equiv \frac{1}{l} \overline{D_{bAg}} . \tag{4.6}$$

Therefore, the initial slope of the accumulation profile is

$$\frac{dQ}{dt} = \frac{\delta_b \overline{D_{bAg}}}{lb} , \tag{4.7}$$

and the diffusion parameter (neglecting the overbar) is

$$\delta_b D_{bAg} = lb \frac{dQ}{dt} = alb \frac{dx}{dt} . \tag{4.8}$$

where a is the thickness of a monolayer and x is the accumulated Ag atoms measured in monolayers.

specimen	$\theta(100)_1/(100)_2$	Σ	specimen	$\theta(100)_1/(100)_2$	Σ
1,2	16.26	25	13	49.00	≈ 73
3	19.00	≈ 37	14,15	53.13	5
4,5	22.62	13	16	58.00	≈ 53
6	25.00	≈ 85	17,18	61.93	17
7,8	28.07	17	19	65.0	≈ 85
9	32.00	≈ 53	20,21	67.38	13
10,11	36.87	5	22	71.00	≈ 37
12	41.00	≈ 73	23,24	73.74	25

Table 4.1: Geometric parameters of diffusion specimens. Angles corresponding to exact Σ's can be found in Table 4.4.

4.2 Grain Boundary Diffusivity

In our experiments, a total of 24 diffusion specimens with 16 different structures in the symmetric [001] tilt boundary series were studied. The geometric parameters of these specimens are listed in Table 4.1. It should be realized that θ is the misorientation angle measured between the two [100] axes of the two adjacent grains, and $90° - \theta$ is the angle between [110] axes.

The temperature range of the measurements was limited by practical difficulties: If the temperature was too low, the diffusion rate was so low that before any detectable change of surface concentration occurred, the surface had already been contaminated. At the other end, the diffusion rate was so fast that it was very difficult to measure the initial accumulation profile. As a result, the annealing temperature ranges are different for different structures because the diffusion rate changes with structure. However, in the temperature ranges that were common for different structures, the same set of temperatures were used so that direct comparison among different structures were possible.

The values of the grain boundary diffusion parameters of silver, determined from Eq. 4.8 using the measured rate of accumulation, are listed in Table 4.2. The effective grain boundary diffusivities are also listed using $\delta_b = 5$ Å. The Arrhenius plots for these boundaries are shown in Figs. 4-3 and 4-4.

specimen	sequence	temperature (°C)	δD_b ($m^3 s^{-1}$)	D_b ($m^2 s^{-1}$)
1	1	170	1.3e-26	2.6e-17
	2	190	2.3e-26	4.6e-17
	3	220	7.1e-26	1.4e-16
	4	260	2.3e-25	4.7e-16
	5	220	6.5e-26	1.3e-16
	6	190	1.8e-26	3.7e-17
2	1	170	1.3e-26	2.6e-17
	2	190	2.9e-26	5.7e-17
	3	205	4.2e-26	8.4e-17
	4	250	2.1e-25	4.2e-16
	5	235	1.3e-25	2.6e-16
	6	190	2.1e-26	4.2e-17
3	1	160	1.4e-26	2.9e-17
	2	190	3.9e-26	7.9e-17
	3	255	3.2e-25	6.4e-16
	4	220	1.1e-25	2.2e-16
	5	190	3.4e-26	6.8e-17
4	1	160	2.0e-26	4.0e-17
	2	190	6.3e-26	1.3e-16
	3	250	5.2e-25	1.0e-15
	4	220	1.6e-25	3.2e-16
	5	190	5.0e-26	1.0e-16
	6	160	1.5e-26	3.0e-17
5	1	160	2.3e-26	4.6e-17
	2	220	2.3e-25	4.6e-16
	3	250	5.5e-25	1.1e-15
	4	190	6.3e-26	1.3e-16
	5	160	1.5e-26	3.1e-17
6	1	160	2.3e-26	4.6e-17
	2	220	2.0e-25	4.0e-16
	3	235	3.8e-25	7.7e-16
	4	190	7.1e-26	1.4e-16
	5	160	1.6e-26	3.2e-17

specimen	sequence	temperature (°C)	δD_b (m^3s^{-1})	D_b (m^2s^{-1})
7	1	130	1.2e-26	2.4e-17
	2	160	3.7e-26	7.5e-17
	3	190	1.1e-25	2.2e-16
	4	220	3.3e-25	6.6e-16
	5	190	9.8e-26	2.0e-16
	6	160	3.0e-26	6.0e-17
8	1	130	1.1e-26	2.3e-17
	2	160	3.6e-26	7.3e-17
	3	160	3.4e-26	6.9e-17
	4	190	1.0e-25	2.0e-16
	5	215	2.5e-25	4.9e-16
	6	190	9.0e-26	1.8e-16
	7	160	3.1e-26	6.2e-17
9	1	130	1.7e-26	3.3e-17
	2	190	1.6e-25	3.2e-16
	3	220	3.7e-25	7.4e-16
	4	190	1.5e-25	2.9e-16
	5	160	4.7e-26	9.4e-17
	6	130	1.0e-26	2.0e-17
10	1	130	2.3e-26	4.6e-17
	2	160	6.0e-26	1.2e-16
	3	190	1.9e-25	3.9e-16
	4	220	6.6e-25	1.3e-15
	5	160	5.2e-26	1.0e-16
	6	130	1.3e-26	2.6e-17
11	1	110	1.0e-26	2.1e-17
	2	130	2.2e-26	4.4e-17
	3	190	1.7e-25	3.4e-16
	4	210	3.8e-25	7.7e-16
	5	160	4.9e-26	1.0e-16
	6	160	5.3e-26	1.1e-16
	7	130	1.4e-26	2.8e-17
	8	110	5.2e-27	1.0e-17
12	1	100	8.3e-27	1.7e-17
	2	130	2.3e-26	4.7e-17
	3	160	7.5e-26	1.5e-16
	4	190	2.2e-25	4.3e-16
	5	160	5.9e-26	1.2e-16
	6	130	1.8e-26	3.6e-17

specimen	sequence	temperature (°C)	δD_b (m^{3}s^{-1})	D_b (m^{2}s^{-1})
13	1	100	6.0e-27	1.2e-17
	2	130	2.3e-26	4.7e-17
	3	220	5.4e-25	1.1e-15
	4	130	1.6e-26	3.2e-17
	5	220	5.3e-25	1.1e-15
	6	190	2.1e-25	4.2e-16
	7	160	5.0e-26	1.0e-16
	8	130	1.4e-26	2.9e-17
14	1	130	1.8e-26	3.6e-17
	2	220	5.1e-25	1.0e-15
	3	130	1.1e-26	2.2e-17
	4	220	4.5e-25	9.1e-16
	5	190	1.5e-25	3.0e-16
	6	160	4.3e-26	8.5e-17
	7	130	1.0e-26	2.0e-17
15	1	220	5.4e-25	1.1e-15
	2	190	1.3e-25	2.6e-16
	3	175	7.9e-26	1.6e-16
	4	160	3.8e-26	7.6e-17
	5	135	1.2e-26	2.5e-17
16	1	240	7.2e-25	1.4e-15
	2	220	4.7e-25	9.4e-16
	3	190	1.3e-25	2.6e-16
	4	160	4.3e-26	8.5e-17
	5	130	8.6e-27	1.7e-17
17	1	240	7.1e-25	1.4e-15
	2	220	3.6e-25	7.3e-16
	3	190	1.3e-25	2.6e-16
	4	160	3.1e-26	6.2e-17
	5	130	7.9e-27	1.6e-17
18	1	230	6.0e-25	1.2e-15
	2	220	3.4e-25	6.8e-16
	3	190	1.2e-25	2.4e-16
	4	160	2.8e-26	5.6e-17
	5	130	5.9e-27	1.2e-17

specimen	sequence	temperature (°C)	δD_b (m^3s^{-1})	D_b (m^2s^{-1})
19	1	130	8.0e-27	1.6e-17
	2	250	8.3e-25	1.7e-15
	3	220	2.2e-25	4.4e-16
	4	190	8.4e-26	1.7e-16
	5	160	2.3e-26	4.6e-17
20	1	130	5.8e-27	1.2e-17
	2	250	5.6e-25	1.1e-15
	3	220	2.0e-25	4.0e-16
	4	190	6.0e-26	1.2e-16
	5	160	1.4e-26	2.9e-17
21	1	250	6.1e-25	1.2e-15
	2	220	2.2e-25	4.4e-16
	3	190	5.7e-26	1.1e-16
	4	160	1.4e-26	2.8e-17
22	1	250	3.6e-25	6.5e-16
	2	220	1.3e-25	2.3e-16
	3	205	5.9e-26	1.3e-16
	4	190	3.6e-26	6.8e-17
	5	160	7.1e-27	1.5e-17
23	1	270	5.8e-25	1.2e-15
	2	250	2.3e-25	4.6e-16
	3	220	8.1e-26	1.6e-16
	4	190	2.2e-26	4.5e-17
	5	160	5.8e-27	1.2e-17
24	1	265	4.6e-25	9.1e-16
	2	245	2.3e-25	4.7e-16
	3	220	9.7e-26	1.9e-16
	4	190	2.3e-26	4.7e-17
	5	175	1.1e-26	2.1e-17

Table 4.2: Measured grain boundary diffusion parameters. The values of diffusivity are obtained by using $\delta_b = 5$ Å.

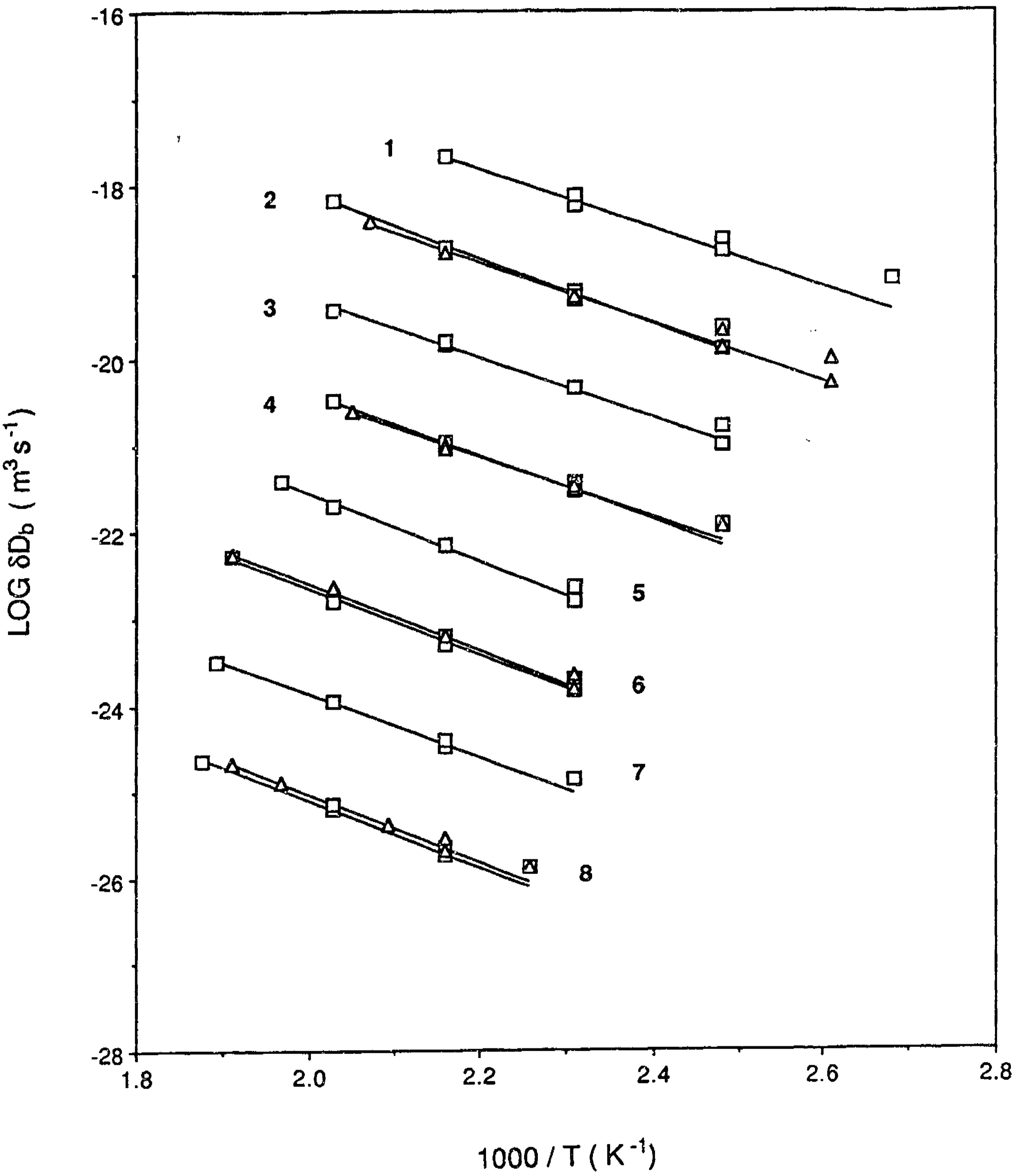

Figure 4-3: Arrhenius plots for measured diffusion parameters of grain boundaries on the $\theta < 45°$ side: $1 = 10^7\,\delta_b D_b\,(41.0°)$; $2 = 10^6\,\delta_b D_b\,(36.9°)$; $3 = 10^5\,\delta_b D_b\,(32.0°)$; $4 = 10^4\,\delta_b D_b\,(28.1°)$; $5 = 10^3\,\delta_b D_b\,(25.0°)$; $6 = 10^2\,\delta_b D_b\,(22.6°)$; $7 = 10\,\delta_b D_b\,(19.0°)$; $8 = \delta_b D_b\,(16.3°)$.

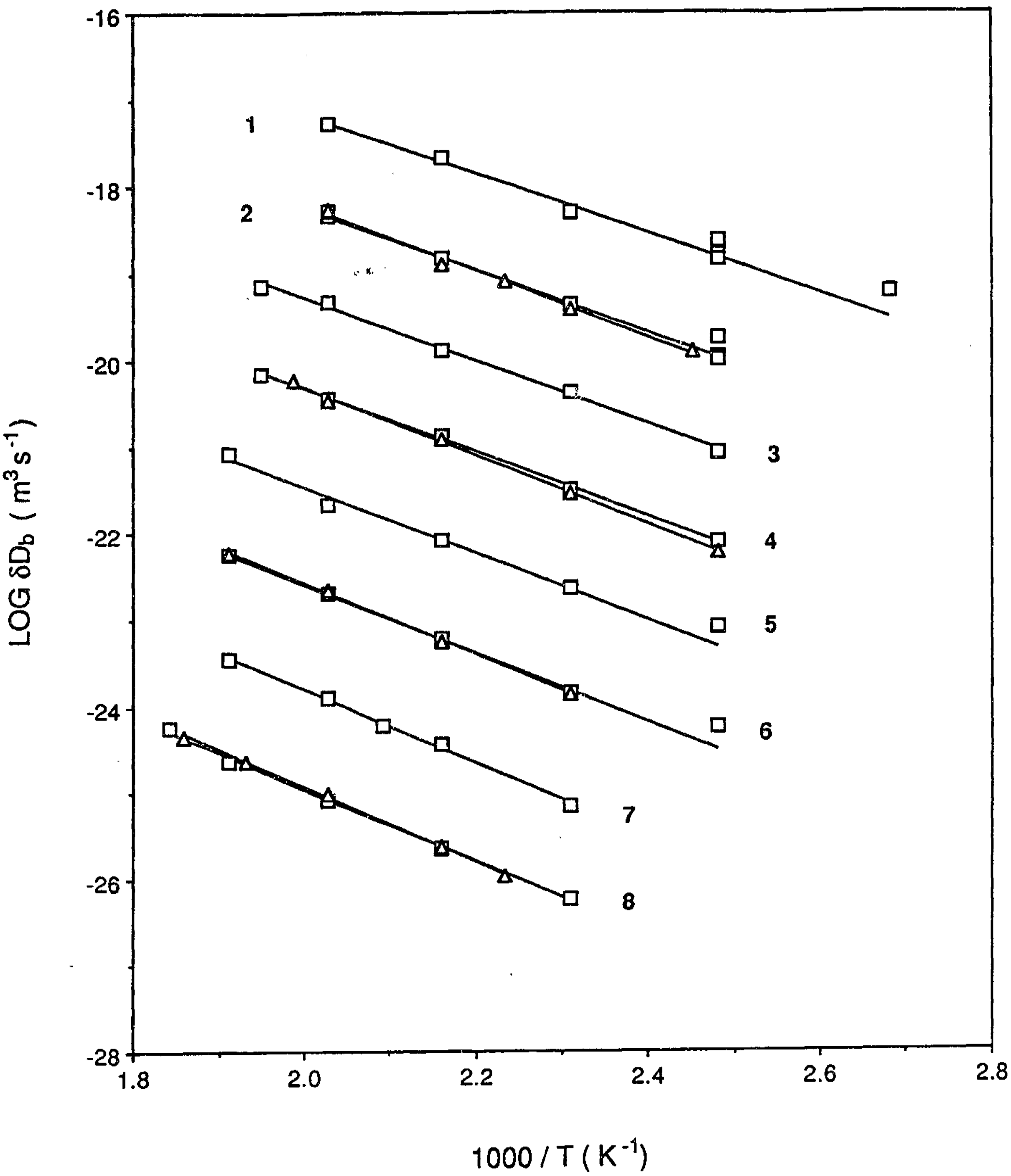

Figure 4-4: Arrhenius plots for measured diffusion parameters of grain boundaries on the $\theta > 45°$ side: 1 = $10^7\,\delta_b D_b\,(49.0°)$; 2 = $10^6\,\delta_b D_b\,(53.1°)$; 3 = $10^5\,\delta_b D_b\,(58.0°)$; 4 = $10^4\,\delta_b D_b\,(61.9°)$; 5 = $10^3\,\delta_b D_b\,(65.0°)$; 6 = $10^2\,\delta_b D_b\,(67.4°)$; 7=10 $\delta_b D_b\,(71.0°)$; 8 = $\delta_b D_b\,(73.7°)$.

4.2.1 Temperature Dependence

For diffusion in a simple lattice, usually one diffusion mechanism has dominant importance, and due to high symmetry, there is only one type of jump a defect can make. Therefore, the lattice diffusion is usually associated with a definite activation energy, and the diffusivity can be expressed in the familiar Arrhenius form:

$$D_l = D_l^0 \exp(-\varepsilon_l/kT) \, . \tag{4.9}$$

In a grain boundary, however, it is possible that several different defect mechanisms are involved simultaneously and frequently a defect makes several different types of jumps during the time it is active in the boundary. Consequently, the temperature dependence for diffusion along grain boundaries may be considerably more complicated, and in general, departures from linearity in the Arrhenius plots are expected. It is therefore very important to study the temperature dependence of the grain boundary diffusivity, from which information about the atomic jumping mechanism may be deduced.

In Fig. 4-5 the diffusivities at four different temperatures for a $\Sigma 5\,(310)$ boundary are plotted against $1/T$. Clearly, except for the first two data points, the logarithms of the diffusivities depend linearly on $1/T$, which indicates an effective constant activation energy. This effective activation energy should reflect the average effect produced by all of the contributions from all possible diffusion mechanisms and different atomic jumping paths. However, it will be clear in the next chapter that in this temperature range, there is only one mechanism and one type of diffusion path that dominates the diffusion process, because, in general, different diffusion mechanisms (or different paths) are usually associated with rather different activation energies. Therefore, this effective activation energy can be considered as the activation energy of a particular atomic jumping mechanism employing the lowest energy jumping paths. Similar to Eq. 4.9, we then have

$$D_b = D_b^0 \exp(-\varepsilon_b/kT) \, . \tag{4.10}$$

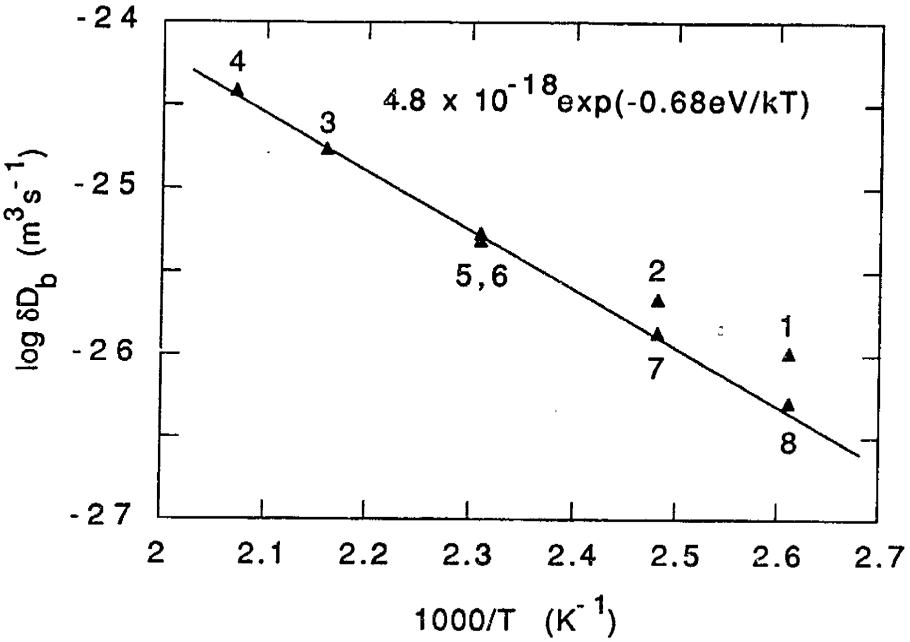

Figure 4-5: Arrhenius plot for a Σ5 (310) boundary. The numbers for each data point show the sequence of the measurements.

The sequence of measurements is indicated in the plot. It is noticed that, compared with the data measured later, the first two measurements indicate an abnormally fast diffusion rate. This phenomenon commonly observed in measurements for other boundaries is believed to be associated with the specimen preparation method. Because the final Ag layer was deposited on a Au film at a very high deposition rate and at relatively low temperature, it is likely that the resulting grain boundaries were not well equilibrated. They may have been microscopically rough (i.e., there may have been a high density of boundary steps present). These extrinsic boundary defects may have been responsible for the fast diffusion initially. After annealing at elevated temperatures, the majority of the boundary steps annihilated each other so that the short wave length roughness of the boundary disappeared and the diffusivities fell approximately on a straight line. After the boundary was stabilized, the diffusion became independent of time. Measurements 5 and 6 are consecutive runs at the same temperatures, which gives very similar values of the diffusivity.

Similar behavior, i.e., linear dependence of $\log \delta_b D_b$ on $1/T$, was observed for all of the boundaries, although small non-systematic deviations from linearity were

specimen	θ	ε_b (eV)	D_b^0 ($m^{-3}s^{-1}$)
1	16.26	7.74	-17.3
2	16.26	7.94	-17.0
3	19.00	7.29	-17.5
4	22.62	7.66	-16.9
5	22.62	7.73	-16.8
6	25.00	7.90	-16.6
7	28.07	7.34	-17.0
8	28.07	6.84	-17.6
9	32.00	6.85	-17.4
10	36.87	7.49	-16.5
11	36.87	6.84	-17.3
12	41.00	6.68	-17.4
13	49.00	6.85	-17.3
14	53.13	7.17	-17.0
15	53.13	7.62	-16.5
16	58.00	7.26	-17.0
17	61.93	7.34	-16.9
18	61.93	7.95	-16.3
19	65.00	7.62	-16.8
20	67.38	7.95	-16.6
21	67.38	8.74	-16.2
22	71.00	8.52	-16.2
23	73.74	8.37	-16.5
24	73.74	8.68	-16.2

Table 4.3: Measured activation energies and pre-exponential factors.

always present due to random errors (see Fig. 4-3 and 4-4). It is then straightforward to extract the activation energies and the pre-exponential factors for each boundary by fitting the data with straight lines (those data points that were measured at the beginning for each boundary when the boundaries had not fully equilibrated were not used for the fitting). The values obtained are listed in Table 4.3.

It is instructive to have a general idea about where our data stand in the vast spectrum of existing grain boundary diffusivity results. The existing data were very well compiled by Gust [43, 44] and surprisingly, when these data are plotted in an Arrhenius diagram using a common reduced temperature scale corresponding to the dimensionless parameter T_m/T, most of them fall closely on a straight line within

$2 \sim 3$ orders of magnitude (see the dashed line in Fig. 4-6). Also shown in Fig. 4-6 are some existing data for Ag and Au grain boundary self-diffusion or for Ag-Au grain boundary interdiffusion plotted with our data represented by the thicker line[1]. It is noticed that most of the data were obtained in the temperature range $T_m/T < 3$, where type-A or B short circuit diffusion behavior is expected. The present work, along with a few others, provides data at lower temperatures where the diffusion is strictly type-C. Clearly, the results of the present experiment are in general agreement with the existing data.

A curious behavior noticed by Hwang and Balluffi [45] is the general upward curvature, which according to them is possibly due to the temperature dependence of the effective activation energy, i.e., the effective activation energy at low temperatures is lower. This was explained by a very simple picture: Diffusion in a grain boundary usually involves atomic jumps along several types of paths. Each type of path is characterized by a different activation energy. At high temperatures, most of these paths are active, so the activation energy of the diffusion along the boundary is a weighted average of the activation energies of the different paths. But at low temperatures, the difference in rate between a large activation energy jump and a small activation energy jump is so large that the diffusion is dominated by the lowest activation energy jump, and therefore the effective activation energy appears to be lower.

The main difficulty arises, however, with the pre-exponential factor. From Fig. 4-6, it is clear that the pre-exponential factors obtained from the low temperature data could be as much as $3 \sim 4$ orders of magnitude smaller than those obtained from the high temperature data. Such a large difference can not be explained away by using arguments based on simple diffusion theory. This problem will be discussed in detail in Section 5.4.

---

[1] Since the majority of the existing data from the literature were obtained in polycrystals, which generally represent high angle boundary properties, this line represents the data from a $\Sigma 5\,(310)$ boundary.

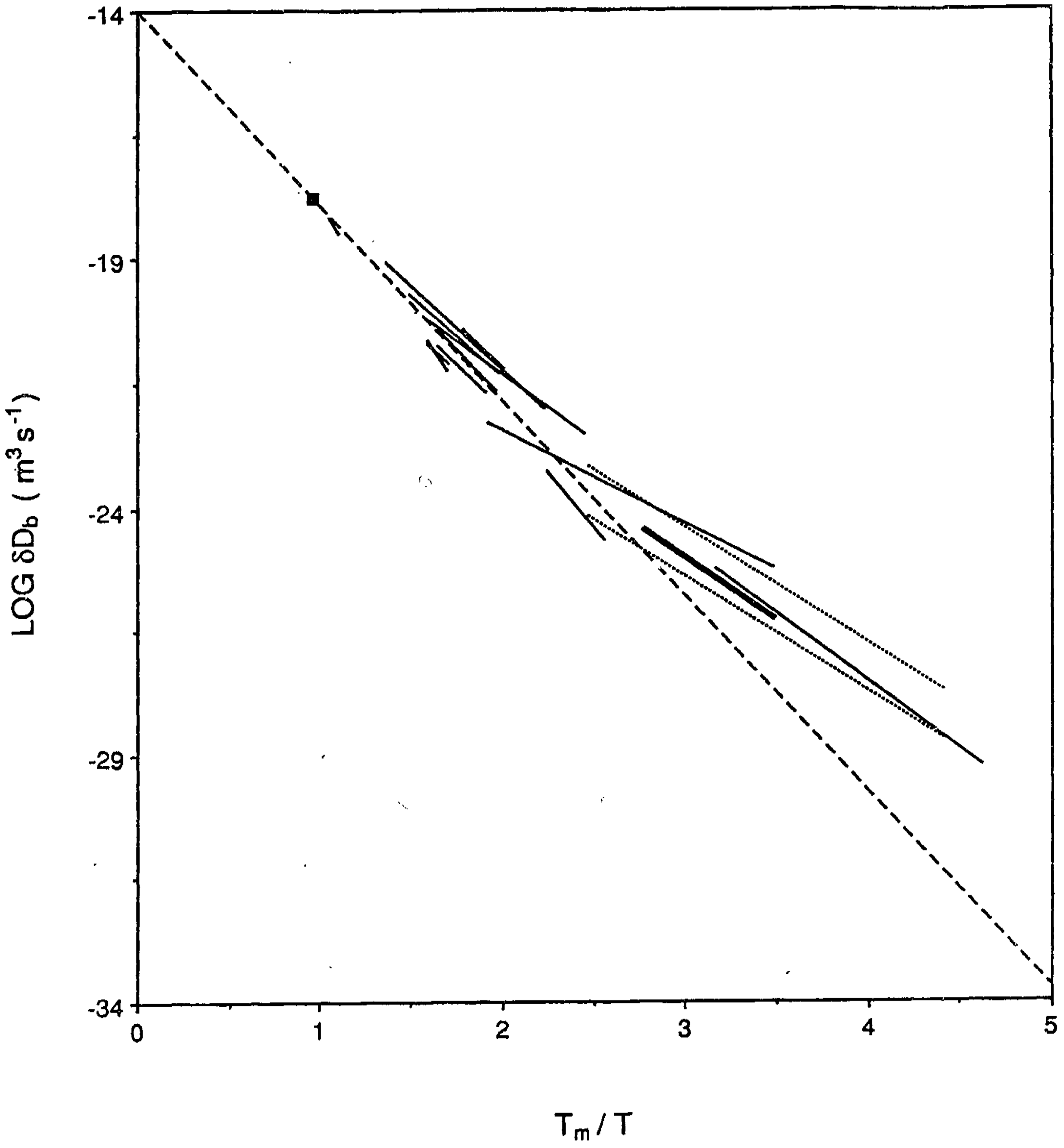

Figure 4-6: Arrhenius diagram of grain boundary diffusion parameters measured at different temperature ranges using a reduced temperature scale (T_m = melting temperature). The dashed line represents the average temperature dependence of diffusion parameters measured primarily in the type-A and B kinetics regimes in different FCC metal systems [1]; the solid square dot represents the diffusivity in the liquid metal just above the melting point multiplied by 10 Å [1]; the two parallel dotted lines give the upper and lower bounds of the results of Hwang and Balluffi [45]; and the thick line represents the present data.

4.2.2 Misorientation Dependence

The general behavior of the misorientation dependence of the diffusivity is illustrated by plotting the measured diffusivities at 190°C against θ (Fig. 4-7). Several features can be seen in the plot:

(1) The diffusivity D_b increases monotonically with increasing tilt angle in the region $\theta < 45°$ and reaches maximum near $\theta = 45°$; then it decreases monotonically with increasing of θ in the region $\theta > 45°$. Since the boundary changes from a low angle boundary to a high angle boundary with increasing of θ in the range $0 < \theta < 45°$ and from a low angle boundary to a high angle boundary with decreasing of θ in the range $90 > \theta > 45°$, we can conclude that the diffusivity increases monotonically with increasing tilt angle.

(2) The diffusion curve is not symmetric about the 45° point. This is expected because the primary dislocations (or structural units) forming the grain boundary on the two sides are different.

(3) No evident cusps or other special properties can be seen at the low-Σ short-period grain boundary misorientations.

It is also noticed from Fig. 4-7, Figs. 4-3 and 4-4 that the measurements of two independent specimens at each low-Σ short-period boundary misorientations give closely agreeing values, which indicates that our experimental method has a high degree of consistency.

We now direct our attention to the Arrhenius parameters, i.e., the activation energies and the pre-exponential factors. In general, both parameters should be functions of tilt angle θ.

From Fig. 4-8, it is evident that the activation energy is a fairly smooth function of tilt angle. It decreases slightly when the boundary structure changes from low angle boundaries to high angle boundaries. Again, no special features can be observed at the low-Σ misorientations.

Values of the pre-exponential factor D_b^0 are plotted in Fig. 4-9. The large non-systematic variations of D_b^0 are due to the following reason. Since the diffusion data were measured in a fairly small temperature range, the slope of the straight line in

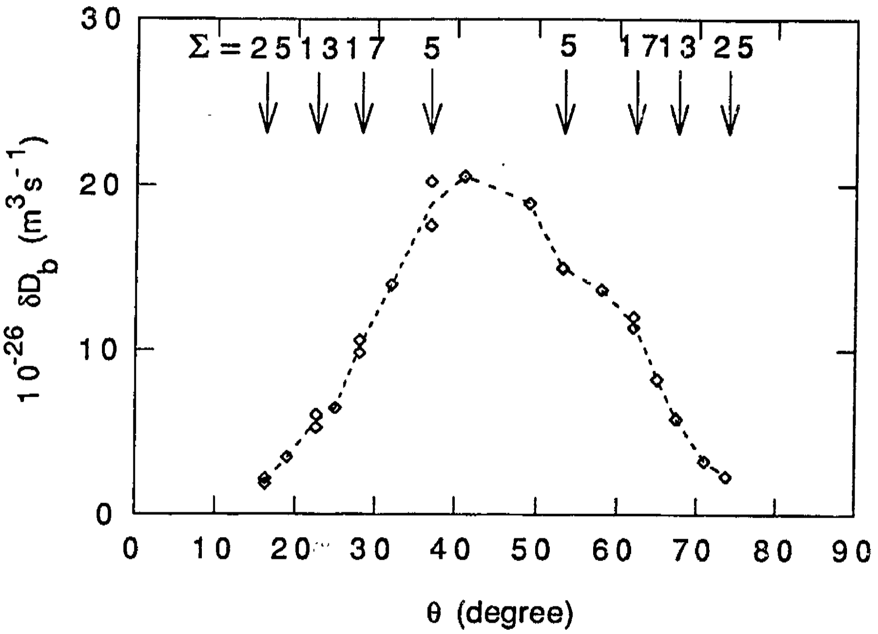

Figure 4-7: Measured grain boundary diffusion parameter $\delta_b D_b$ as a function of misorientation angle θ at 190°C. The diamond symbols represent the measures diffusion parameters for each individual specimen obtained from the Arrhenius straight line fit.

the Arrhenius plot obtained by fitting the data is not highly accurate. It is easy to see that a slight change of the slope will change the intercept of the line at the D_b axis (at $1/T = 0$) drastically. Consequently, the values of D_b^0 obtained this way have large errors. It is somewhat surprising to observe that the pre-exponential factors increase with θ by about one order of magnitude from left to right. According to Zener's theory of D_0, this is possible only if the migration energies of the defect mechanism are considerably larger on the right than on the left. As it will be seen in the next chapter, this is a real possibility.

The results generated in the present work are unique because this experiment is the only one which has studied the structural effects on grain boundary diffusion in the type-C kinetics regime. Comparison with the previous work (see review in Chapter 2) can then only be indirect, i.e., within different kinetics regimes. In view of the above discussion that the general behavior of boundary diffusion could be different for different temperature regions, it is not expected that the misorientation dependence should be the same. However, we believe the very basic features of the structural effects as

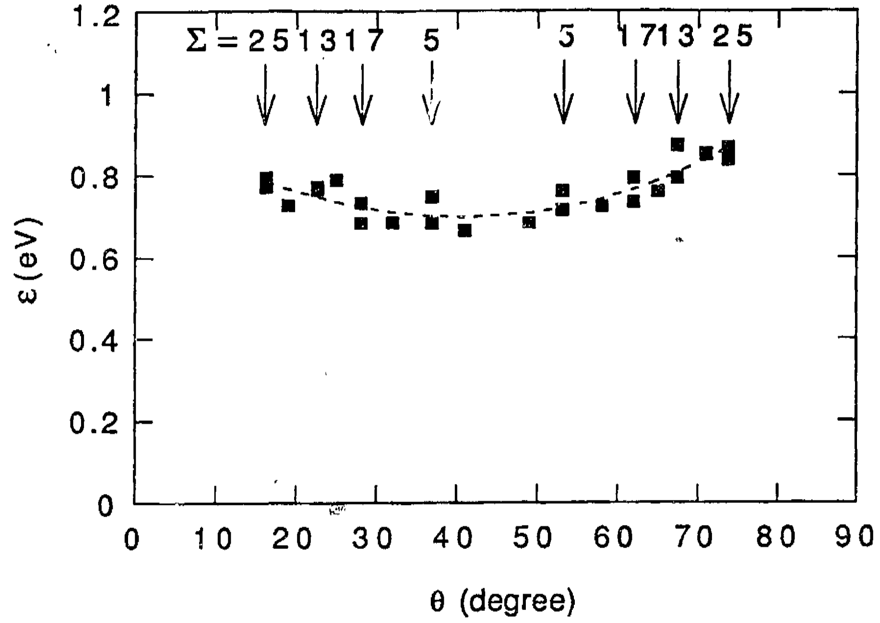

Figure 4-8: Measured activation energy as a function of θ.

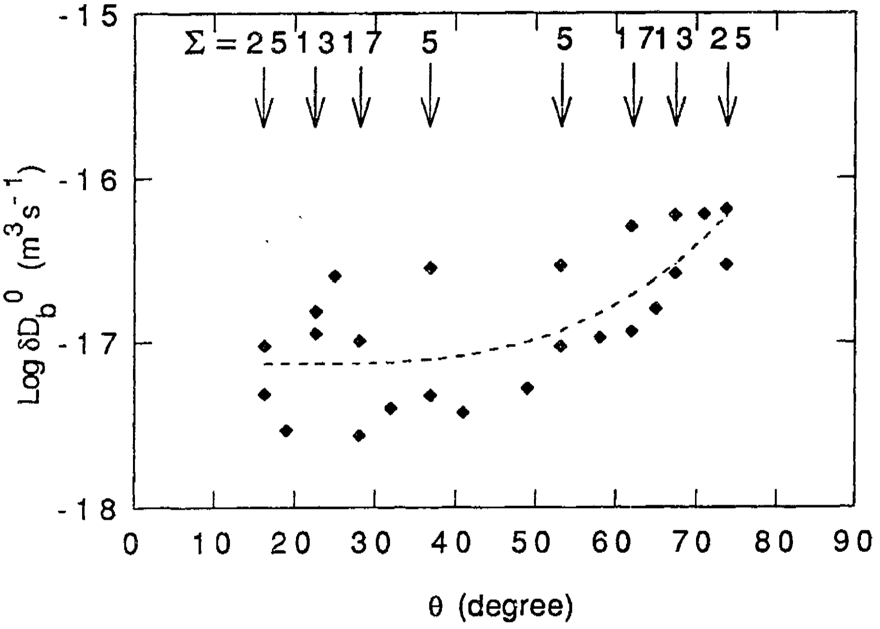

Figure 4-9: Measured pre-exponential factor as a function of θ.

θ	2λ	Σ	structural units	θ	2λ	Σ	structural units
0.00	[0,1]	1	C	46.40	[-3,7]	29	DBB
7.63	[-1,15]	113	12CD	47.92	[-4,9]	97	DBBB
8.80	[-1,13]	85	10CD	48.89	[-5,11]	73	DBBBB
10.39	[-1,11]	61	8CD	53.13	[-1,2]	5	B
12.68	[-1,9]	41	6CD	58.11	[-5,9]	53	A4B
14.25	[-1,8]	65	5CD	59.49	[-4,7]	65	ABBB
16.26	[-1,7]	25	4CD	61.93	[-3,5]	17	ABB
18.92	[-1,6]	37	CCCD	64.01	[-5,8]	89	ABABB
22.62	[-1,5]	13	CCD	64.94	[-7,11]	85	ABABABB
25.06	[-2,9]	85	CDCCD	67.38	[-2,3]	13	AB
25.99	[-3,13]	89	CDCDCCD	71.08	[-5,7]	37	AABAB
28.07	[-1,4]	17	CD	73.74	[-3,4]	25	AAB
30.51	[-3,11]	65	CDCDD	75.75	[-7,9]	65	AAABAAB
31.89	[-2,7]	53	CDD	77.32	[-4,5]	41	AAAB
36.87	[-1,3]	5	D	79.61	[-5,6]	61	4AB
41.11	[-3,8]	73	DDB	81.2	[-6,7]	85	5AB
42.08	[-5,13]	97	DBDDB	82.37	[-7,8]	113	6AB
43.60	[-2,5]	29	DB	90.00	[-1,1]	1	A

Table 4.4: Structural unit representations of grain boundary core structures.

mentioned above remain in effect. Consequently, it is concluded that our results are in agreement with those that showed rather smooth and monotonic behavior, and contradict those that showed deep cusps at low-Σ boundary misorientations.

4.3 Discussion of Structural Unit Model

According to the SU model, a grain boundary core can be decomposed into a regularly arranged array of structural units. By inspecting the dichromatic pattern, it is easy to find the period vectors for the boundaries with small exact Σ values (i.e., the delimiting boundaries). Then, following the method described in Chapter 2, the period vectors of large period intermediate boundaries are decomposed into those of the delimiting boundaries (e.g., $\Sigma1$, $\Sigma5$), thus providing the composition ratio of the two delimiting units. In Table 4.4, the core structures in terms of structural units are listed for some exact Σ boundaries in the [001] tilt series.

With the above knowledge of the structure of the grain boundaries, it is then straightforward to compare the experimental results with the expectation from the SU model. As proven by Balluffi et al., at the limit that the distortion of the structural units with changing of angle is negligible, the diffusivity vs. the misorientation angle should be represented by the solid straight lines as illustrated in Fig. 4-10. Since the boundaries $\Sigma 1\,(C)$, $\Sigma 5\,(D)$, $\Sigma 5\,(B)$ and $\Sigma 1\,(A)$ are chosen as delimiting boundaries, the straight lines should connect boundaries $\Sigma 1\,(C)$, $\Sigma 17\,(CD)$, $\Sigma 5\,(D)$, $\Sigma 29\,(DB)$, $\Sigma 5\,(B)$, $\Sigma 13\,(AB)$ and $\Sigma 1\,(A)$. Clearly, the agreement is only qualitative, which indicates that the effect of the distortion is not negligible. Assuming that the distortion is gradual and in a continuous fashion, it is easy to realize that if we choose more boundaries as delimiting boundaries and therefore decrease the angular range that each pair delimits, it is possible to achieve a better fit, because the change of the structural units in a smaller angular region should be less significant. The dashed lines in Fig. 4-10 illustrate one of the possible descriptions, in which $\Sigma 17\,(CD)$ and $\Sigma 13\,(AB)$ are added as delimiting boundaries. Obviously, more refined steps will generate better fit, but will also reduce the value of the SU model as a tool for predicting grain boundary structures and properties. However, the fact that a very limited number of steps can provide a fairly good fit suggests that the basic idea of the model is right, i.e., the grain boundary structure or property changes gradually as the composition of structural units changes continuously. In contrast, the diffusion results in the Al/Zn system (see Section 2.3.2) with deep cusps at low-Σ short-period misorientations suggest that the grain boundary properties change rather suddenly at those low-Σ short-period misorientations, and are thus difficult to explain on the basis of the SU model.

The general picture of the structure-diffusivity relationship is now clear: in the transition from low angle to high angle the density of the fast diffusion units (B or D) increases while at the same time the structures of these units are gradually distorted: both of these factors contribute to the change of diffusivity.

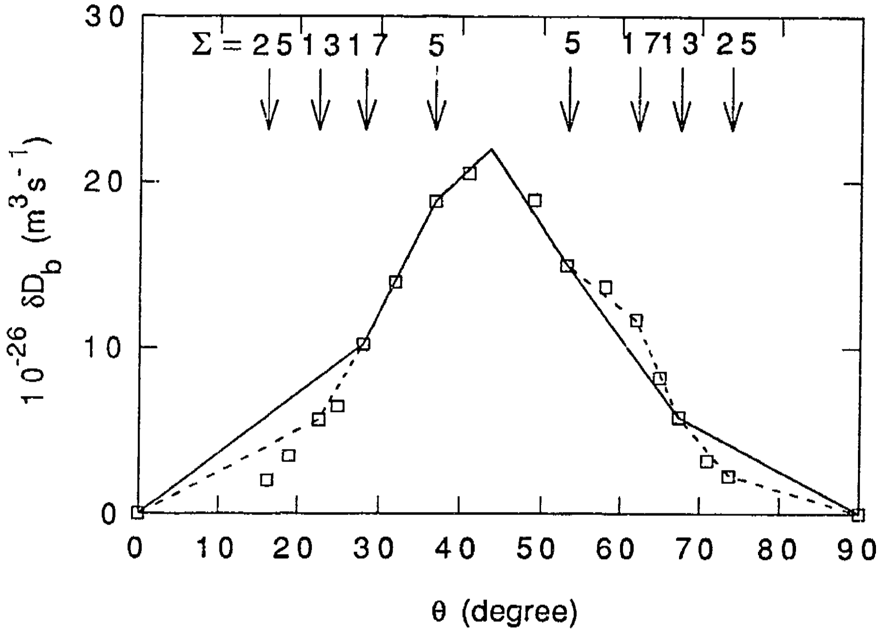

Figure 4-10: Interpretation of measured diffusion parameters by the SU model. The solid lines represent the description by delimiting boundaries $\Sigma 1\,(C)$, $\Sigma 5\,(D)$, $\Sigma 5\,(B)$ and $\Sigma 1\,(A)$. The dashed lines represent the refined description by introducing extra delimiting boundaries $\Sigma 17\,(CD)$ and $\Sigma 13\,(AB)$, and the square symbols represent the diffusion parameters obtained by the best Arrhenius straight line fit (values for the exact low-Σ boundaries are averaged over the two specimens).

4.4 Existence of Cusps

One of the questions this experiment was designed to answer is whether or not there are significant cusps in the grain boundary diffusivity vs. misorientation curves. Our experimental data, in contradiction with some of the previous observations, show clearly that no cusps at the low-Σ short-period boundaries are evident. To understand this result we should trace the origin of this problem and examine the previous observations.

4.4.1 Why Cusps were Expected

Two factors seem to have contributed to the belief of the existence of cusps:

(1) It is often observed that on average, the activation energies of grain boundary diffusion in materials with high activation energies for lattice diffusion are higher than those for grain boundary diffusion in materials with low lattice diffusion activation energies. Further, in the same material, the diffusion along low energy boundaries (for example twin boundaries, stacking faults) is slower than diffusion in high energy boundaries (general high angle boundaries). In an attempt to correlate the grain boundary diffusion, lattice diffusion and grain boundary energies, Borisov, et al. [58] postulated that the Gibbs free energy associated with a defect diffusion mechanism in the grain boundary is simply given by its level in the lattice, or

$$g_b = g_l - 2a^2\gamma_b \tag{4.11}$$

where $g_b = \varepsilon_b - s_bT$, is the Gibbs free energy required for an elementary jump by the operating mechanism in the grain boundary and g_l is the Gibbs energy for the corresponding process in the lattice, a is the mean distance between the atoms in the grain boundary which is approximately equal to the primitive lattice vector, and γ_b is the grain boundary energy per unit area. The factor 2 arises from the multiplicity consideration of the grain boundary between two crystals.

Although this empirical relationship is qualitatively consistent with some experimental observations, it has no theoretical basis and has never been seriously tested, therefore its applicability is vague.

(2) Since the establishment of CSL theory, a large number of calculations as well as experiments have been devoted to the study of the low-Σ short period boundaries. In many cases, it is certain that these special boundaries correspond to local minima (i.e., cusps) on the energy vs. misorientation curves.

Combining the above knowledge, it is then natural to think that these low-Σ boundaries might have special diffusion properties as well, or more specifically, there might exist cusps at the special misorientations on the diffusion curves.

To examine these arguments, we should examine the relevance of Borisov's relation to the origin of the cusps on the energy curves. First, in Borisov's relation, the grain boundary energy γ_b is a quantity that describes the total excess energy associated with all of the atoms in the boundary per unit area. It is therefore an average quantity. Consequently, the activation energy g_b given by the relation can at best represent only an average effect. However, it is known that in a grain boundary there are many different inequivalent sites and many inequivalent jumping paths. It will be clear in the next chapter, that the diffusion in grain boundaries is mainly controlled by a few diffusion paths out of many possible paths. As a result, an argument based on average quantities may not describe the actual situation realistically.

Secondly, by using the CSL model, it is easy to understand that a deviation from the misorientation of an exact Σ boundary requires the introduction of secondary grain boundary dislocations. The strain field of these dislocations generally causes an energy cusp. However, the strain field is usually very weak, at least in the [001] tilt boundary system. Thus it has little effect on the boundary core structure between the secondary dislocation cores. According to the SU model, the grain boundary cores are composed of structural units, and the fast diffusion units in the mix of units are responsible for the fast grain boundary diffusion. The secondary grain boundary dislocations are simply perturbations in the sequence of otherwise very regularly arrayed structural units. These perturbations are made by adding extra units, which do not have much effect on the activation energy for diffusion in the surrounding units. The effect of these extra units themselves is well taken into account by the change of structural unit composition from the unperturbed boundary structure. Clearly, the cusps on the energy curves are largely due to elastic strain energy stored in the lattice, rather than the change of energy inside the boundary core structure. Thus these cusps are not related in any way to the grain boundary diffusion.

From the above discussion, it is obvious that neither Borisov's arguments nor the appearance of cusps on grain boundary energy vs. misorientation curves should lead to the conclusion that cusps should appear on grain boundary diffusion vs. misorientation curves.

4.4.2 Observations of Cusps

Some support for the existence of such cusps has been provided by previous measurements in which deep cusps at low-Σ misorientations were indeed observed unambiguously (see Section 2.3.2). However, all of these experiments involved chemical systems. Also, the chemical effects were not carefully considered. Among all possible chemical effects, we mention two which may have been responsible for the appearance of cusps in previous studies:

Grain Boundary Segregation Factor

It is noticed that for the bicrystal profiling method, the diffusion equations and boundary conditions remain unchanged if the grain boundary thickness δ_b is replaced by $s_b\delta_b$ for chemical diffusion systems, where s_b is the segregation factor of the solute. As a result, the quantity which is measured experimentally is the so called lumped diffusion parameter $s_b\delta_bD_b$ for chemical diffusion, rather than δ_bD_b as for self-diffusion systems. Since all of the previous work reporting cusps used the bicrystal profiling method, their observations indicate that $s_b\delta_bD_b$ curves are cusped. Since s_b is known to depend significantly on structure and has often been found to be relatively small at short period boundaries due to the relatively small number of attractive sites available [8], it is likely that boundary segregation may be responsible for the appearance of cusps on $s_b\delta_bD_b$ vs. misorientation curves.

DIGM

The problem of measuring grain boundary diffusion is compounded by the fact that the grain boundary, in general, does not remain stationary during the diffusion. It has been observed that DIGM occurs in all of the chemical systems studied in the previous bicrystal profiling work. Unlike the situation in the surface accumulation method, where boundary sink and source effects can be minimized by choosing a large surface to boundary capacity ratio and DIGM effects can be essentially eliminated, in the bicrystal profiling method the leaking of diffusant from the boundary to the lattice could be altered by DIGM and the alloyed zone produced by the DIGM could have markedly affected the measured concentration of the diffusant. There is evidence that the extent of DIGM is dependent on the grain boundary structure and is relatively weak for low-Σ boundaries [34]. Although a quantitative evaluation of the effect produced by DIGM on diffusion measurements by the bicrystal profiling method requires detailed modeling, it is evident that the effect could significantly change the appearance of grain boundary diffusivity vs. misorientation curves.

In view of the above discussion, it is concluded that the existence of cusps on diffusivity vs. misorientation curves is theoretically unfounded and that their experimental observations are likely to have been caused by extraneous chemical effects.

4.5 Source of Error

In this experiment, errors could come from every measurement of quantities such as temperature, Auger intensity, etc. Errors could also come from other factors, such as the imperfection of the specimens. These errors could be random, or they could be systematic to a certain extent; their effects on the final results are therefore very complicated. In the following, these sources of error will be discussed, and, whenever possible, the magnitude of each error will be estimated. Possible errors introduced in the data interpretation process due to deficiencies of the model or the approximations necessary to utilize the model (such as the neglect of chemical effects) were discussed in detail in Section 3.1, and therefore will not be further discussed here.

4.5.1 Errors from Measurement

Temperature

The relationship between the error in measuring T and the resulting error in D_b can be easily derived:

$$\frac{dD_b}{D_b} = \frac{\varepsilon_b}{kT}\frac{dT}{T} . \tag{4.12}$$

Because, in the temperature range where the measurements were made, ε_b/kT is a large factor, small variations in T could have relatively large effects on D_b.

In this experiment, errors in temperature measurement could have been caused by several factors:

i. Auger Electron Beam Heating Since the diffusion specimen is a self-standing thin film of thickness about 2000 Å (1000 Å of Au and 1000 Å of Ag), which has rather limited thermal conductance, the local heating due to the electron beam should be considered.

A simple model (Fig. 4-11) neglecting any radiation loss (which is very small in the experimental temperature range) leads to the following simple relation

$$T_c - T_R = \frac{P}{4\pi\mathcal{K}}(1 + 2\ln\frac{R}{r}) , \tag{4.13}$$

where T_c is the temperature at the center of the beam heating spot, and T_R is the temperature of the grid on which the film is mounted. The power of the electron beam $P = IV = 100$ nA $\times$ 5 kV$= 10^{-4}$ W. The conductance of the film $\mathcal{K} = K_{Au}l_{Au} + K_{Ag}l_{Ag} \approx 3.5$ W cm^{-1} K^{-1}. The size of the opening of the Au grid $R \sim 35\mu$m, and the dimension of the beam rastering area $r \sim 15\mu$m. Therefore,

$$T_c - T_R \approx 0.2 \text{ K} ,$$

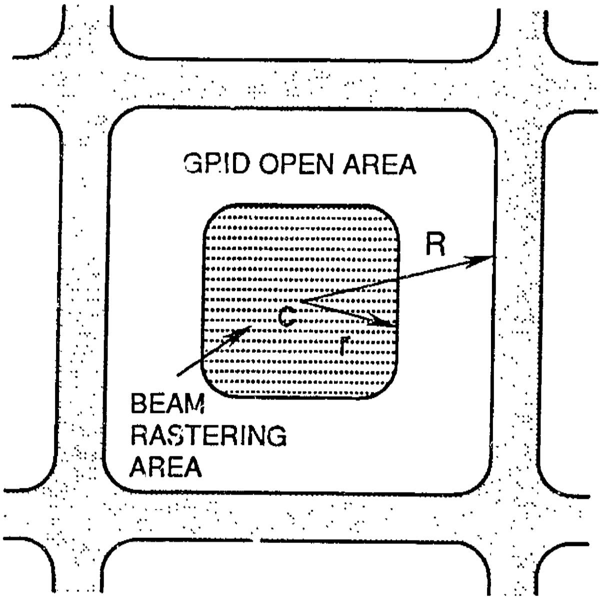

Figure 4-11: Model used for calculating the effect of beam heating.

which introduces a negligible error of about 1% or less depending on the temperature.

ii. The Temperature Difference between the Au Grid and the Thermocouple Contact Point Because the cylindrical part of the hot stage carrying the specimen has to be rotated frequently, it is very difficult to measure the temperature of the specimen directly. Instead, the thermocouple is welded on the heating block, which is stationary (see Fig. 3-19). The thermal conductance from the heating block to the grid can be limited at the following two places:

(1) At the center hole where the grid is mounted on the cylinder. The radiation energy from the grid is very small, so that the conductance between the cylinder and the grid is large enough to insure thermal equilibrium between them. In fact, the mounting arrangement here is exactly the same as employed at standard TEM hot stages (see Fig 3-19), which are designed to be used at much higher temperatures with temperature measuring accuracy. So it is believed that the error introduced from this origin is negligible.

(2) At the interface between the cylinder and the frame. Since the cylinder has to be rotated relative to the frame, the fitting between them can not be too tight.

Also the area of the cylinder surface that is exposed to open space is relatively large (~1 cm^2), and the situation is therefore not clear-cut. An experimental test was therefore conducted by welding a second thermocouple to the cylinder and measuring the temperature of both the cylinder and the frame simultaneously when quasi-equilibrium was reached. The test was conducted in high vacuum so that the only heat loss was via radiation. The results showed that the difference of the temperature of the two parts was less than 1 K at ~ 300°C.

The upper limit of the error introduced to D_b from the above error sources is about 5%. This error should be systematic for each individual specimen, because the thermal conductance across the cylinder-frame interface should be about the same for all the consecutive measurements of a specimen. However, among the six stages there could have been some slight differences. Therefore there is a random component in this error from one specimen to another.

iii. Error from the Temperature Measurement System The temperature of the stage was controlled and measured by an Eurotherm Digital Temperature Controller, which has a temperature resolution of ±1 K. The thermocouples were welded on the frames with extreme care so that point contacts were produced. Therefore the error from the thermocouple itself is negligible. Obviously, any error would have to be a reading error, and thus must be random for each measurement. The resulting error in D_b is therefore about ±5%.

Thickness of Specimen

From Eq. 4.8 the effect of any thickness variation on measured diffusivity is

$$\frac{dD_b}{D_b} = \frac{dl}{l} \,. \tag{4.14}$$

In this experiment, the thickness of the specimen is controlled by the amount of material placed in the evaporation source and the distance between the source and the substrate. A thickness calibration was carefully made by depositing thin films on glass slides using measured amounts of source material and measuring the final film thickness with a Dektak Surface Profiler. For the same amount of source, the film thickness variation could be as large as 10% at film thickness near 1000 Å. This error is the combined error in measuring the amount of material in the source, the error due to randomness of the deposition, and the error in measuring the thickness. The thickness of the final diffusion specimen could also be measured by tilting the specimen in the TEM and measuring the boundary projection. However, the error of this method is generally larger than 10% for films about 2000 Å thick. So the thickness used in the calculation of D_b is that derived from the measured amount of material in the source according to the calibration, and the upper limit of error is 10%. This error is systematic for an individual boundary, but it is random from one specimen to the other.

Error from Auger Intensity Measurements

First, an error could be introduced simply because of counting statistics. However, since Ag has a very strong signal, even at very small concentrations, the statistical error is small enough to be neglected. On the other hand, both the current and voltage of the primary electron beam varied and the Auger electron multiplier was rather noisy. By monitoring the pure Ag surface for a long period of time while the surface is statically sputtered by Ar ions, this variation is estimated to be about 10%. It should be realized that the error in I^0_{356} can be minimized by averaging over long periods of time. But the error in I_{356} and I_{69} propagated into the profile slope, so that the initial profile slope has an error of about 10%.

4.5.2 Other Possible Sources

Lattice Diffusion

In the surface accumulation method it is always assumed that lattice diffusion is frozen out, so that the system is in the type-C kinetics regime. To verify the assumption, let us estimate the lattice diffusion distance during the time of one diffusion run. At 270°C, the highest annealing temperature used, the lattice diffusivity $D_l = 2 \times 10^{-24}$ m^{-2}s^{-1}. At such a high temperature the early constant accumulation period is less than 2 minutes for the slowest diffusion boundary. The diffusion distance in the lattice is then

$$l_l = \sqrt{D_l t} = 0.15 \text{ Å} ,$$

which confirms that the experiments were performed strictly in the type-C kinetics regime.

Contribution to Surface Accumulation other than from Grain Boundary Diffusion

Besides grain boundary diffusion, Ag atoms could diffuse along twin boundaries, stacking faults and dislocations that are randomly distributed in the film. In order to make sure that these defects do not contribute significantly to the measured accumulation, a test was conducted by diffusion annealing at 300°C a Ag-Au double layered single crystal film containing about the same density of defects. No appreciable amount of Ag could be detected on the Au surface after about one hour.

Another possibility is that Ag could diffuse around the edges of the film, or through a hole or a crack in the film and then migrate to the area of measurement. In order to prevent such a process from affecting the measurements, specimen areas that were within 100μm from a hole or a crack were not used for the measurements. In the test mentioned above, it was found that no Ag can be detected 50μm away from the edge of the film. So we conclude that the Ag accumulations measured were completely due to grain boundary diffusion.

Error due to Grain Boundary Imperfections

Grain boundary quality can affect the diffusion rate significantly. For example, the diffusion rate was abnormally high when the specimen was first annealed because the boundary probably contained a high density of steps. Although any short wavelength roughness of the boundary can be annealed out quickly, longer wavelength roughness

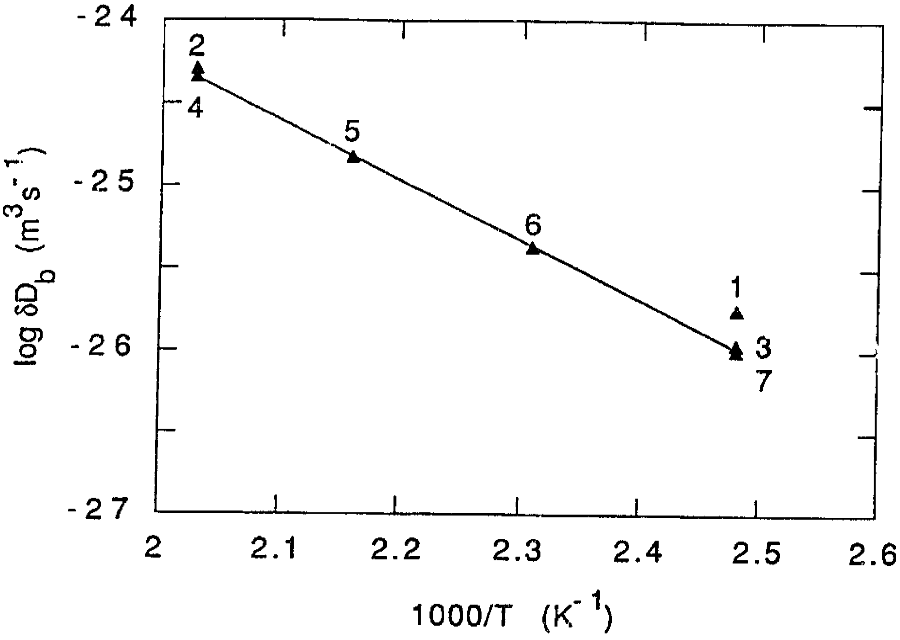

Figure 4-12: Arrhenius plot illustrating a test of the diffusion slowing-down effect. The numbers in the plot show the sequence of measurement.

remains[2]. As a result, a certain density of boundary steps existed during each measurement. It is difficult, however, to estimate the error that could be introduced by such boundary steps, because the diffusion rate at those steps is unknown.

In an attempt to obtain a rough idea about the magnitude of this effect, a specimen ($\theta = 41°$) was repeatedly measured at low and high temperatures. The results shown in Fig. 4-12 confirm that the slowing-down effect was significant only for the first few measurements, and that the error in the later measured data due to this effect is less than 10%. Since this error depends on the history of each specimen, it should be a systematic error for the measurement of the individual specimen, but random from one specimen to another.

In the above, possible sources of error were discussed, and the magnitudes of the possible errors were estimated. However, their overall effect on the final diffusion results is very difficult to estimate, because of the different nature of each type of error. From the data analysis it is observed that the random deviations of each

---

[2] In general, the rate of diminishing of interfacial roughness is inversely proportional to λ^4.

individual diffusivity data from the best straight line fits are less than 20%, which is in very good agreement with the probable total random error discussed above. The random error in the activation energies of about 0.03 eV should depend largely on the systematic errors discussed above. An error of 0.03 eV corresponds to an error of about 10-20% in D_b, which is again consistent with the above discussion.

Therefore, we conclude that the error for each individual diffusivity data point is less than 35%, the error for the diffusivity of a boundary obtained by best straight line fits is about 15%, and the error for ε_b is about 0.03 eV.

Chapter 5

Atomistic Model for Grain Boundary Diffusion

In the last chapter, the experimental results were presented and discussed at the microstructural level. In order to have some understanding at the atomic level, an analytical formulation of correlated walks is extended to describe diffusion in grain boundaries, and then computer simulations are performed to study the grain boundary diffusion kinetics and mechanism. These calculated results are then compared with the experimental results obtained in the present work and also previous work.

5.1 Correlated Walk in a Grain Boundary - A General Formulation

In general, for grain boundary self-diffusion in metals or grain boundary chemical diffusion in substitutional alloys, a simple interstitial mechanism is unlikely to play a major role, because large open channels are generally absent in the boundary structures. Therefore atomic transport along the grain boundary is usually by more complicated defect mechanisms (e.g., vacancy and interstitialcy mechanisms). As a result, the movement of a marked atom in the boundary is often a correlated walk.

Following Howard[59], consider a marked atom M, which completes a series of n

elementary jumps by a certain defect mechanism or several mechanisms executed in sequence in a period of time τ. The total displacement in the z direction is

$$Z_M = z_1 + z_2 + z_3 + \dots + z_n \ . \tag{5.1}$$

The square of the displacement is then

$$Z_M^2 = \sum_{i=1}^{n} z_i^2 + 2 \sum_{i=1}^{n-1} \sum_{j=i+1}^{n} z_i z_j \ . \tag{5.2}$$

If drifting effects (e.g., that present in ionic diffusion in an external electrical field) are absent, the diffusion of the marked atom in the z direction is given by the Einstein formula:

$$D_M = \lim_{\tau \to \infty} \frac{< Z_M^2 >}{2\tau} \ , \tag{5.3}$$

where the symbol $< >$ represents the operation of averaging over a large ensemble. Substituting Eq. 5.2 into Eq. 5.3, we have

$$D_M = \lim_{\tau \to \infty} \left[< \sum_{i=1}^{n} z_i^2 > +2 < \sum_{i=1}^{n-1} \sum_{j=i+1}^{n} z_i z_j > \right] / 2\tau \ . \tag{5.4}$$

It should be realized that $n \to \infty$ at the limit $\tau \to \infty$, and the summation and averaging operations are exchangeable, therefore,

$$D_M = \lim_{\tau \to \infty} \left[\sum_{i=1}^{\infty} < z_i^2 > +2 \sum_{i=1}^{\infty} < \sum_{m=1}^{\infty} z_i z_{i+m} > \right] / 2\tau \ . \tag{5.5}$$

For ordered structures, such as grain boundaries are believed to possess, assume that there are R different types of elementary jumps (i.e., they can not be related by translation symmetry operations). Let p and q be two jumps of the same type. We then have

$$< z_p^2 >=< z_q^2 >= z_p^2 \ ;$$

$$< \sum_{m=1}^{\infty} z_p z_{p+m} >=< \sum_{m=1}^{\infty} z_q z_{q+m} > \ .$$

Therefore,

$$D_M = \lim_{\tau\to\infty} \sum_{\alpha=1}^{R} n_\alpha \left[z_\alpha^2 + 2 < \sum_{m=1}^{\infty} z_\alpha z_{\alpha+m} > \right] / 2\tau \ , \tag{5.6}$$

where n_α is the number of type-α jumps in the series. Let r_α be the type-α jump rate:

$$r_\alpha = \lim_{\tau\to\infty} \frac{n_\alpha}{\tau} \ , \tag{5.7}$$

Eq. 5.6 can be rewritten as:

$$D_M = \frac{1}{2} \sum_{\alpha=1}^{R} r_\alpha z_\alpha^2 \left[1 + \frac{2 \sum_{\alpha=1}^{R} < \sum_{m=1}^{\infty} z_\alpha z_{\alpha+m} > / z_\alpha^2}{\sum_{\alpha=1}^{R} r_\alpha z_\alpha^2} \right] \ . \tag{5.8}$$

If the jumping of the marked atom is completely random (e.g., small atoms diffusing in a loosely packed lattice by a simple interstitial mechanism) then the term in the square bracket equals 1, and we have

$$D_M = D_R = \frac{1}{2} \sum_{\alpha=1}^{R} r_\alpha z_\alpha^2 \ . \tag{5.9}$$

However, in more closely packed materials, atomic migration is usually facilitated by certain defect interactions resulting in a correlation between successive jumps. This correlation effect is described by the quantity in the square bracket of Eq. 5.8, which is consequently called the correlation factor:

$$f = 1 + \frac{2 \sum_{\alpha=1}^{R} < \sum_{m=1}^{\infty} z_\alpha z_{\alpha+m} > / z_\alpha^2}{\sum_{\alpha=1}^{R} r_\alpha z_\alpha^2} \ . \tag{5.10}$$

In general, f is less than unity because successive jumps of an atom tend to have displacements in opposite directions. This is obvious for diffusion by a vacancy mechanism: a marked atom having exchanged with a vacancy has a better than random chance of executing the reverse jump. As a result, the effect of correlation is simply reducing the diffusivity from the random diffusivity by the correlation factor:

$$D_M = D_R f \ . \tag{5.11}$$

For a complex system where different jumping paths or even different defect mechanisms co-exist, it is instructive to decompose the diffusivity into individual contributions. From Eq. 5.8, D_M can also be expressed as

$$D_M = \frac{1}{2}\sum_{\alpha=1}^{R} r_\alpha z_\alpha^2 \left[1 + 2 < \sum_{m=1}^{\infty} z_\alpha z_{\alpha+m} > / z_\alpha^2\right] , \tag{5.12}$$

or

$$D_M = \frac{1}{2}\sum_{\alpha=1}^{R} r_\alpha z_\alpha^2 f_\alpha , \tag{5.13}$$

where

$$f_\alpha = 1 + 2 < \sum_{m=1}^{\infty} z_\alpha z_{\alpha+m} > / z_\alpha^2 \tag{5.14}$$

is the partial correlation factor for a type-α jump. The total correlation factor can then be expressed as:

$$f = \frac{\sum_{\alpha=1}^{R} r_\alpha z_\alpha^2 f_\alpha}{\sum_{\alpha=1}^{R} r_\alpha z_\alpha^2} . \tag{5.15}$$

For a specific grain boundary, assume there are N grain boundary "lattice" sites (i.e., the sites that are occupied by atoms when the boundary is in the lowest energy configuration) in a unit cell. Also assume there are n_a type-a sites (type-a sites could be grain boundary lattice sites or interstitial sites). Let τ_a be the total amount of time the marked atom stays at type-a sites during a jumping sequence, then

$$\tau_a = P_a \tau , \tag{5.16}$$

where P_a is the probability that the marked atom is on a type-a site. If a type-α jump is the jump from a type-h site to a type-d site, then the number of type-α jumps during the period τ is

$$n_\alpha = \Gamma_{M\alpha(h\to d)}\tau_h = \Gamma_{M\alpha(h\to d)} P_h \tau , \tag{5.17}$$

where $\Gamma_{M\alpha(h\to d)}$ is the jumping frequency of the marked atom from a type-h site to a type-d site (type-α). Therefore the type-α jump rate becomes

$$r_\alpha = \frac{n_\alpha}{\tau} = \Gamma_{M\alpha(h\rightarrow d)}P_h \ . \tag{5.18}$$

From Eq. 5.13, the diffusivity of the marked atom is then:

$$D_M = \frac{1}{2}\sum_{\alpha=1}^{R}\Gamma_{M\alpha(h\rightarrow d)}P_h z_\alpha^2 f_\alpha \ . \tag{5.19}$$

In the above summation, the partial correlation factor f_α is the most complicated quantity. Although it describes the extent of correlation of a particular jump type α, it is actually associated with all of the possible jump types in the boundary as Eq. 5.14 indicates. Therefore, an analytical discussion of f_α is possible only for the few simplest lattices. For more complicated structures like grain boundaries, numerical tools are more adequate. In the next section, such studies using a computer will be carried out for an idealized grain boundary. In the following, we will concentrate on the jumping frequency $\Gamma_{M\alpha}$ and the occupation probability P_h for different defect mechanisms.

Among all possible diffusion mechanisms, the vacancy, interstitial and interstitialcy mechanisms are most frequently observed. Thus they are discussed in detail in the following:

Vacancy Mechanism The jump of a marked atom from site h to site d by a vacancy mechanism can be considered as a two-step process: first, a vacancy occupies site d, then the vacancy jumps into site h, thus

$$\Gamma_{M\alpha(h\rightarrow d)} = C_d^v \Gamma^v_{-\alpha(d\rightarrow h)} \ , \tag{5.20}$$

where C_d^v is the occupation probability of a vacancy at site d, and $\Gamma^v_{-\alpha(d\rightarrow h)}$ is the jumping frequency of the vacancy from site d to site h. With local equilibrium established, the detailed balance requires:

$$C_d^v \Gamma^v_{-\alpha(d\rightarrow h)} = C_h^v \Gamma^v_{\alpha(h\rightarrow d)} \ , \tag{5.21}$$

therefore,

$$\Gamma_{M\alpha(h\to d)} = C_h^v \Gamma^v_{\alpha(h\to d)} \; . \tag{5.22}$$

It should be realized that at the dilute vacancy concentration limit (which is true in the low temperature region), and if local equilibrium is established, the probability that the marked atom is in each grain boundary lattice site is the same. Therefore P_h is simply the fraction of type-h sites in the lattice:

$$P_h = \frac{n_h}{N} \; , \tag{5.23}$$

where n_h is the number of type-h sites in a grain boundary unit cell. Finally, the diffusivity of the marked atom by the vacancy mechanism is

$$D_M = \frac{1}{2N} \sum_{\alpha=1}^{R} C_h^v \Gamma^v_{\alpha(h\to d)} z_\alpha^2 f_\alpha n_h \; . \tag{5.24}$$

Interstitial Mechanism If the marked atom jumps interstitially, then

$$\Gamma_{M\alpha(h\to d)} = \Gamma^i_{\alpha(h\to d)} \; , \tag{5.25}$$

where all the sites refer to interstitial sites and $\Gamma^i_{\alpha(h\to d)}$ is the type-α interstitial jump frequency. If the interstitial concentration is dilute, the probability that the marked atom is at type-h sites is

$$P_h = C_h^i \frac{n_h}{N} \; , \tag{5.26}$$

where C_h^i is the occupation probability of an interstitial at a type-h site, and n_h is the number of type-h interstitial sites in a grain boundary unit cell.

As mentioned before, interstitial diffusion is usually uncorrelated, thus $f_\alpha = 1$. Therefore, the diffusivity of the marked atom by the interstitial mechanism is

$$D_M = \frac{1}{2N} \sum_{\alpha=1}^{R} C_h^i \Gamma^i_{\alpha(h\to d)} z_\alpha^2 n_h \; . \tag{5.27}$$

Interstitialcy Mechanism Two situations have to be considered separately:

(1) The marked atom is initially at a grain boundary lattice site h^l and jumps to a grain boundary interstitial site d^i. Clearly, an interstitial at any of the nearest interstitial sites s^i except at d^i has a probability to cause such a jump. Therefore,

$$\Gamma_{M\alpha(h^l\to d^i)} = \sum_{s^i} C^i_s \Gamma^{icy}_{\alpha(s^i\to h^l,h^l\to d^i)} \;, \tag{5.28}$$

where C^i_s is the occupation probability of an interstitial at s^i, and $\Gamma^{icy}_{\alpha(s^i\to h^l,h^l\to d^i)}$ is the jumping frequency of the marked atom from h^l to d^i, caused by an interstitial jumping from s^i to h^l. The summation is taken over all of the nearest s^i's except d^i.

In this case, the probability of finding the marked atom at type-h^l sites is similar to that for the vacancy mechanism. Therefore,

$$P_h = n^l_h/N \;, \tag{5.29}$$

where n^l_h is the number of grain boundary lattice sites of type-h^l in a unit cell.

(2) The marked atom is initially at an interstitial site h^i and jumps to a grain boundary lattice site d^l and causes the atom initially at site d^l to jump to an interstitial site s^i. Similarly,

$$\Gamma_{M\alpha(h^i\to d^l)} = \sum_{s^i} \Gamma^{icy}_{\alpha(h^i\to d^l,d^l\to s^i)} \;, \tag{5.30}$$

where $\Gamma^{icy}_{\alpha(h^i\to d^l,d^l\to s^i)}$ is the jumping frequency of the marked atom from h^i to d^l. The summation is taken over all of the nearest interstitial sites of d^l except h^i.

It is easy to realize that here P_h should be the same as for the interstitial mechanism, therefore,

$$P_h = C^i_h n^i_h/N \;, \tag{5.31}$$

where n^i_h is the number of type-h^i interstitial sites in a unit cell.

Combining the above cases, we have the diffusivity of the marked atom by the interstitialcy mechanism:

$$D_M = \frac{1}{2N}\left[\sum_{\alpha 1}^{R1}\sum_{s'} C_s^i \Gamma^{icy}_{\alpha 1(s^i \to h^l, h^l \to d^i)} z_{\alpha 1}^2 f_{\alpha 1} n_h^l + \sum_{\alpha 2}^{R2}\sum_{s'} C_h^i \Gamma^{icy}_{\alpha 2(h^i \to d^l, d^l \to s^i)} z_{\alpha 2}^2 f_{\alpha 2} n_h^i\right] . \tag{5.32}$$

The above formula will be used in the next and the last sections in this chapter.

5.2 Correlated Walk in a Grain Boundary - A Case Study

As indicated in the last section, a very important quantity in describing a correlated walk is the correlation factor. In fact, much of the information about grain boundary structure is embodied in the correlation factor. For example, if the marked atom jumps three dimensionally in the boundary slab, the correlation factor would be close to that in the bulk ($f = 0.653$ for diffusion by a vacancy mechanism in a simple cubic structure). However, if diffusion is very much confined to a two-dimensional plane, f will be reduced ($f = 0.467$ for diffusion by a vacancy mechanism in a square lattice). Finally, if atoms diffuse along a one-dimensional path, f will approach 0.

The importance of the correlation factor is also due to the fact that it is closely associated with the diffusion mechanism. Accurate measurements of correlation factors in bulk materials by the isotope effect method have helped in identifying diffusion mechanisms in different materials. Attempts have also been made by Robinson and Peterson [30] to identify the diffusion mechanism in grain boundaries in Ag by using similar techniques. However, due to a lack of understanding of the correlated walks in grain boundaries, their conclusion that the vacancy mechanism holds is not convincing. Efforts were then made to calculate correlation factors by matrix methods [60, 61, 62, 63, 64]. However, due to the limitation of these methods, the systems studied were oversimplified dislocation-like structures confined one dimensionally, and therefore reflect only certain aspects of the problem.

5.2.1 Model and Method

The Idealized Grain Boundary

In the following, an idealized grain boundary with changeable parameters is studied in order to reveal the basic features of the correlated walk in grain boundaries. The vacancy mechanism is assumed for its simplicity (similar behavior is expected for the interstitialcy mechanism which will be discussed later in Section 5.4). Since in a real grain boundary, atoms move three dimensionally, but are also heavily confined to several active paths (i.e., atoms move considerably faster in these paths), it is of particular interest to study the diffusion behavior for different confinements.

The idealized boundary is illustrated in Fig. 5-1. Assume it is a symmetric tilt boundary with tilt axis z perpendicular to the paper. The circles represent the grain boundary lattice sites. Assume that the grain boundary region consists of three atomic layers (the center layer labeled 1, and two side layers labeled 2). Also assume the periodicity in the y direction is $3a$ (i.e., assuming only one type of structural unit, and each unit has 6 different sites 1A, 2A, ...2C) and in the z direction is a. The formation energy of a vacancy at each site and the migration energy for each possible path are assumed to be different from those in the bulk and from one site (or path) to another. Clearly, by changing these energies, the diffusion environment, or effectively the grain boundary structure, can be changed flexibly. The formation and migration energies are expected to increase with increase of $|x|$, and to change periodically along the y direction.

With the formation energies and migration energies specified, the jumping rates can then be expressed explicitly. According to Boltzmann statistics, the vacancy occupation probability at a type-h site is

$$C_h^v = \exp\left(-\frac{g_h^f}{kT}\right) = \exp\left(-\frac{s_h^f}{k}\right)\exp\left(-\frac{\varepsilon_h^f}{kT}\right) , \qquad (5.33)$$

where g_h^f, s_h^f and ε_h^f are the Gibbs free energy, entropy and energy of vacancy formation at a type-h site. Usually it can be assumed that $s^f \approx k$ to a rough approximation.

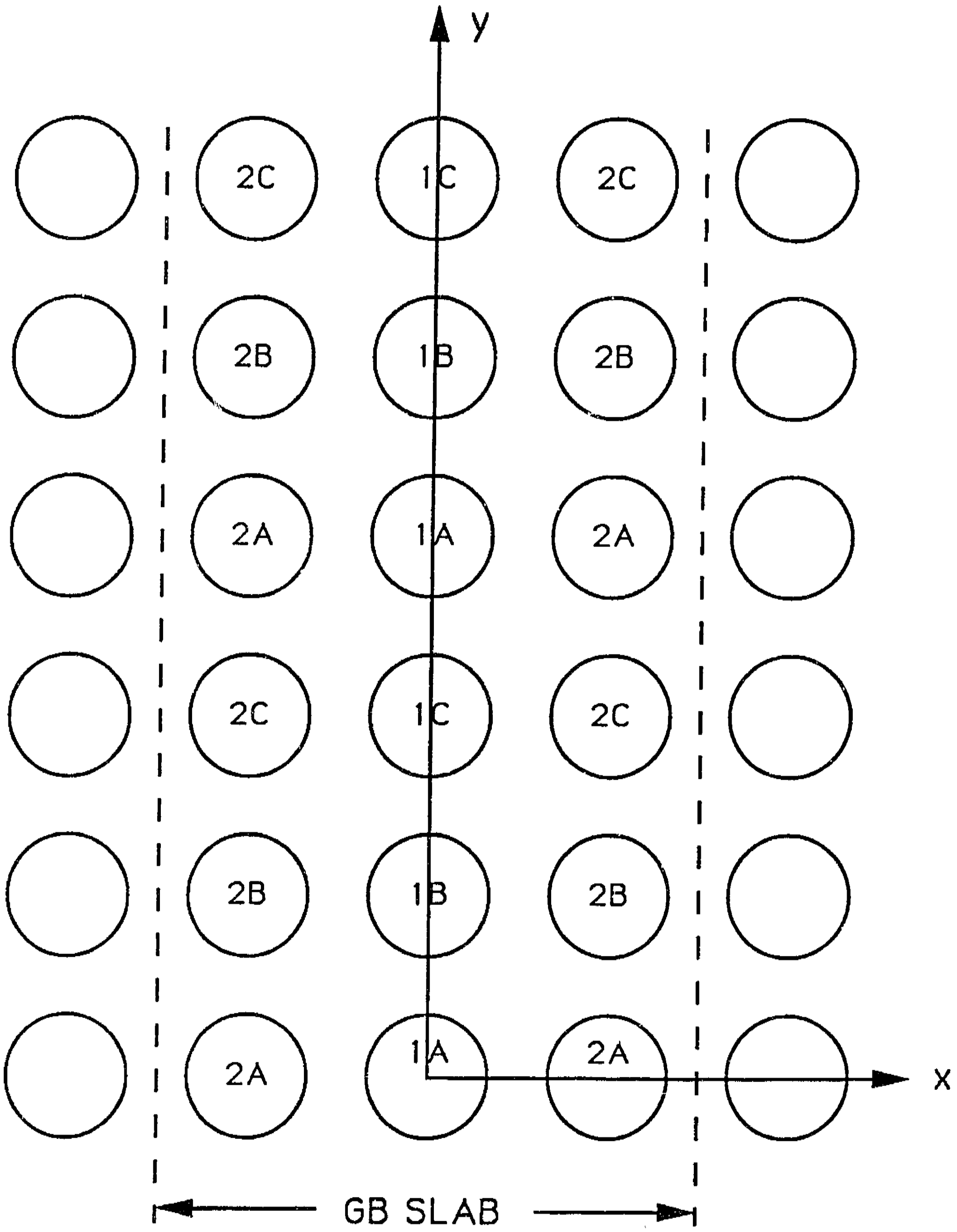

Figure 5-1: Illustration of an idealized tilt grain boundary. The z axis is the tilt axis which is perpendicular to the paper. The periods in the y and z directions are $3a$ and a, respectively.

Since the jumping process is thermally activated, the jumping frequency of a vacancy for a type-α jump can be expressed as:

$$\Gamma_\alpha^v = \nu_\alpha^0 \exp\left(-\frac{g_\alpha^m}{kT}\right) \exp\left(-\frac{\Delta\varepsilon^f}{kT}\right) = \nu_\alpha^0 \exp\left(-\frac{s_\alpha^m}{k}\right) \exp\left(-\frac{\varepsilon_\alpha^m}{kT}\right) \exp\left(-\frac{\Delta\varepsilon^f}{kT}\right) , \tag{5.34}$$

where g_α^m, s_α^m and ε_α^m are the Gibbs free energy, entropy and energy of vacancy migration of type-α jump respectively (see Fig. 5-2), and

$$\Delta\varepsilon_\alpha^f = \begin{cases} \varepsilon_h^f - \varepsilon_d^f & \text{if } \varepsilon_h^f - \varepsilon_d^f < 0 , \\ 0 & \text{otherwise.} \end{cases} \tag{5.35}$$

ν_α^0 is an effective atomic "attempt" frequency which is of order of the characteristic vibration frequency of the atoms in the boundary, which can be estimated from

$$\nu_\alpha^0 = \nu_D \sqrt{\frac{\varepsilon_\alpha^m}{\varepsilon_l^m}} , \tag{5.36}$$

where $\nu_D \sim 4 \times 10^{12}$ s^{-1} is the Debye frequency in the lattice, and $\varepsilon_l^m \sim 1$ eV is the typical migration energy in the lattice.

The migration entropy can be estimated by Zener's theory of D^0 [65]:

$$s_\alpha^m = \frac{\beta_Z \varepsilon_\alpha^m}{T_m} , \tag{5.37}$$

where T_m is the melting temperature and β_Z is defined as

$$\beta_Z = -\frac{d(\mu/\mu_0)}{d(T/T_m)} , \tag{5.38}$$

where μ refers to an appropriate elastic modulus, and the suffix 0 refers to the absolute zero temperature. $\beta_Z \approx 0.45$ and 0.31 for Ag and Au bulk respectively [65]. Because the atomic bonding at grain boundaries is "looser", $\beta_Z = 0.5$ is assumed in estimating the migration entropy in the boundaries.

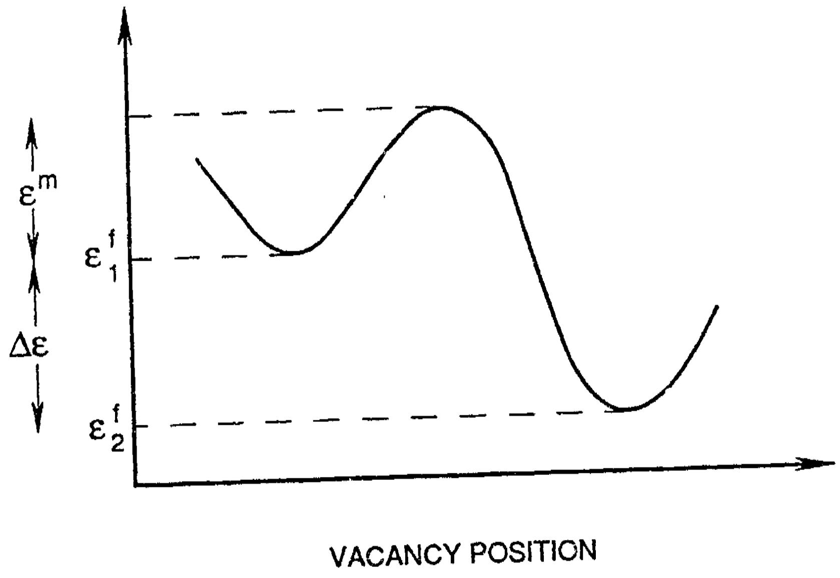

Figure 5-2: Definition of the vacancy migration energy between two sites with different vacancy formation energies.

Calculation Method

The partial correlation factor for a type-α (h to d) jump can be calculated by using Eq. 5.14. A computer program was developed to simulate the correlation process:

(1) A vacancy is introduced into the system at site d and allowed to cause a type-α jump of the marked atom, resulting in the vacancy occupying site h and the marked atom occupying site d and the displacement of the marked atom z_α.

(2) The vacancy is then allowed to jump freely to a nearest neighbor site s_i. The decision of which nearest neighbor site it jumps into is made by a Monte Carlo method: First the probability of the vacancy jumping from site h to each nearest neighbor sites s_i is calculated:

$$P_i = \frac{\Gamma^v(d \rightarrow s_i)}{\sum_i \Gamma^v(d \rightarrow s_i)} \,. \qquad (5.39)$$

Then a random number *ran* is produced by a random number generator which generates numbers that are randomly distributed between 0 and 1. If

$$\sum_{i=0}^{k-1} P_i < ran < \sum_{i=1}^{k} P_i \ , \tag{5.40}$$

the vacancy jumps to site s_k. This procedure is repeated to let the vacancy jump around until it wanders so far away that the probability of returning is practically 0.

(3) During the course of the lifetime of the vacancy, it may exchange with the marked atom a number of times. Each time the exchange happens, the displacement $z_{\alpha+m}$ is recorded. The summation in Eq. 5.14 can then be calculated afterwards.

(4) The whole simulation process (from 1 to 3) is repeated many times to achieve the ensemble average.

5.2.2 Calculated Results

As far as diffusion correlation is concerned, the most fundamental nature of the grain boundary structure is its effective dimensionality. Using the above method, we can easily study the change of the behavior of correlated walks in grain boundaries as the dimensionality changes. This can be achieved without excessive hypothetical assumptions by systematically changing the relative activation energies in the grain boundary region and calculating the correlation factor as well as the diffusivities. This can be divided into two parts:

Two-Dimensional Confinement

In diffusion studies, a grain boundary is usually simplified as a thin slab consisting of a few atomic layers. Within this slab, a simple effective diffusivity is assumed. This simple slab model implying uniformity inside the grain boundaries, although useful in describing the overall diffusion capability of the boundary, has never been tested for correlation effects. In the following, the center atomic layer and the two adjacent layers are assumed to form the grain boundary slab. The energies are then varied linearly from those shown in Fig. 5-3a to those in Fig. 5-3b by five steps. The numbers on the left side of the circles are the vacancy formation energies at each site, the numbers on the right are the vacancy migration energies in the z direction. The numbers between the two circles are the migration energies from one site to the other. The first configuration (Fig.5-3a) corresponds to a completely uniform slab, so that the diffusion is only confined by the slab walls. As the energies change, diffusion is more and more confined in the center atomic layer, and finally approaches a two-dimensional system in Fig. 5-3b.

The grain boundary diffusion processes in the form of correlated walks along the tilt axis z were studied. Fig. 5-4a illustrates the partial correlation factors f_1 and f_2 (the suffixes 1 and 2 refer to the jumping paths in the z direction in the layer 1 and 2, respectively) and the total correlation factor f for two different temperatures ($T_m/T = 1.5$ and 3.5) as a function of the energy changes. At the initial configuration, although the diffusion is confined in three atomic layers, the correlation is effectively the same as in a three-dimensional simple cubic lattice. As the energies in the two side layers increase, the partial correlation factor of the center layer decreases rapidly at first and then gradually reaches the value for a two-dimensional square lattice, while the partial correlation factor f_2 (for the side layers) increases to unity. The increase of f_2 is easily understood because once a vacancy has made an exchange in the side layers, it has a large probability to jump into the center layer and rarely goes back to cancel the exchange. The total correlation factor, however, follows the trend of f_1 because the diffusion is more and more dominated by the center layer as the energies in the side layers increase. It is also clear that the correlation factors change more rapidly at lower temperatures. This is because the energy barriers are effectively higher at lower temperatures: at high temperatures the vacancy can frequently jump into the side layer, so that the confinement effect is weaker; at low temperatures, small energy barriers pose more severe confinements.

More practical configurations can be achieved by increasing the energies in path 1A (path along 1A sites). Similarly, the energies are changed from the configuration in Fig. 5-3b to that in Fig. 5-3c by five steps, which gradually confines the diffusion to two parallel adjacent paths (1B and 1C). The correlation factors are illustrated in Fig. 5-4b. The general trend is very similar to that in Fig. 5-4a, with the total

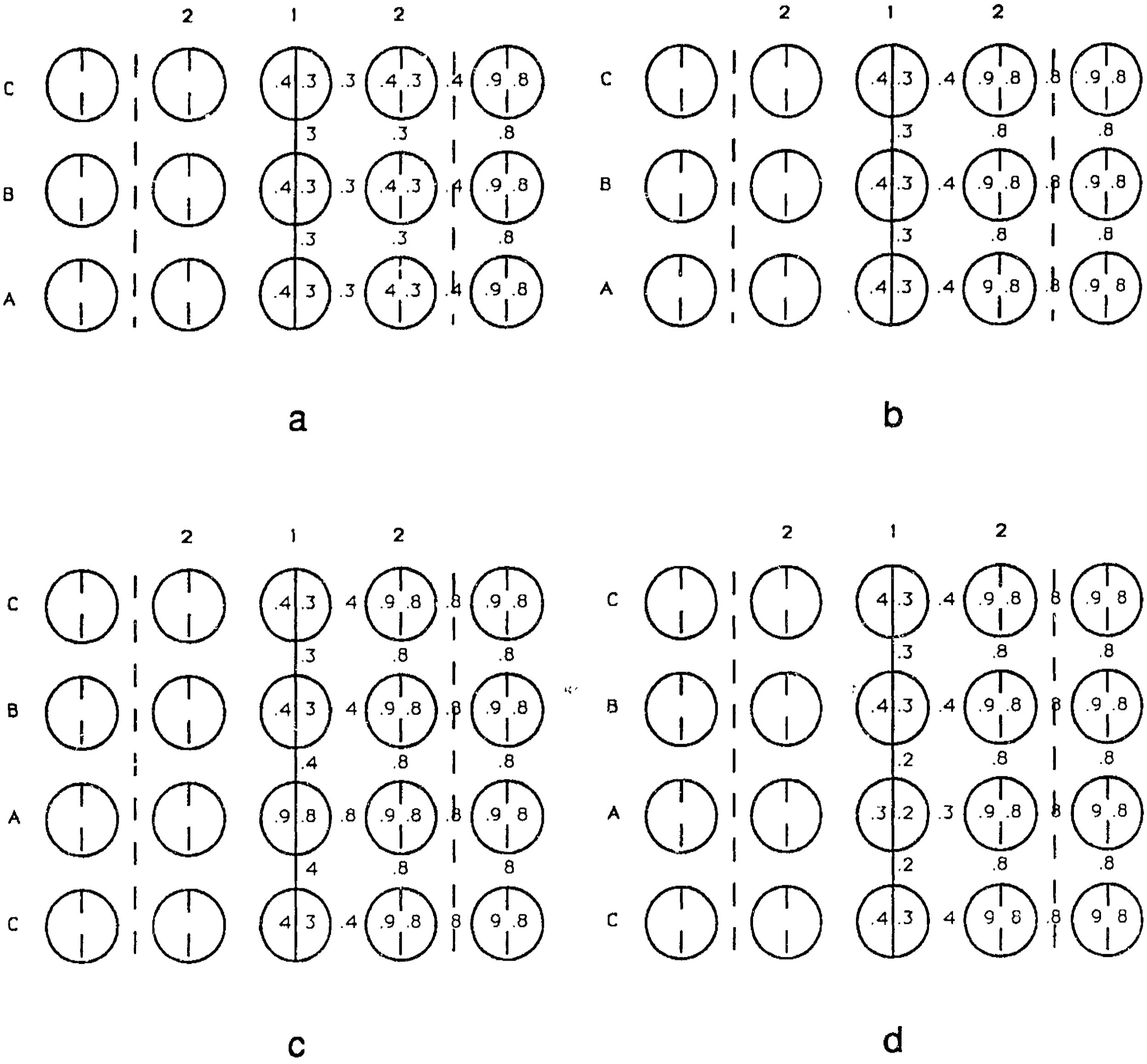

Figure 5-3: Configurations of different confinements: (a) A uniform grain boundary slab; (b) A two-dimensional lattice; (c) A confinement to two parallel paths; (d) A one-dimensional isolated path confinement. The numbers on the left side of the circles are the vacancy formation energies at each site, the numbers on the right are the vacancy migration energies in the z direction. The numbers between the two circles are the migration energies from one site to the other. The energies are in eV.

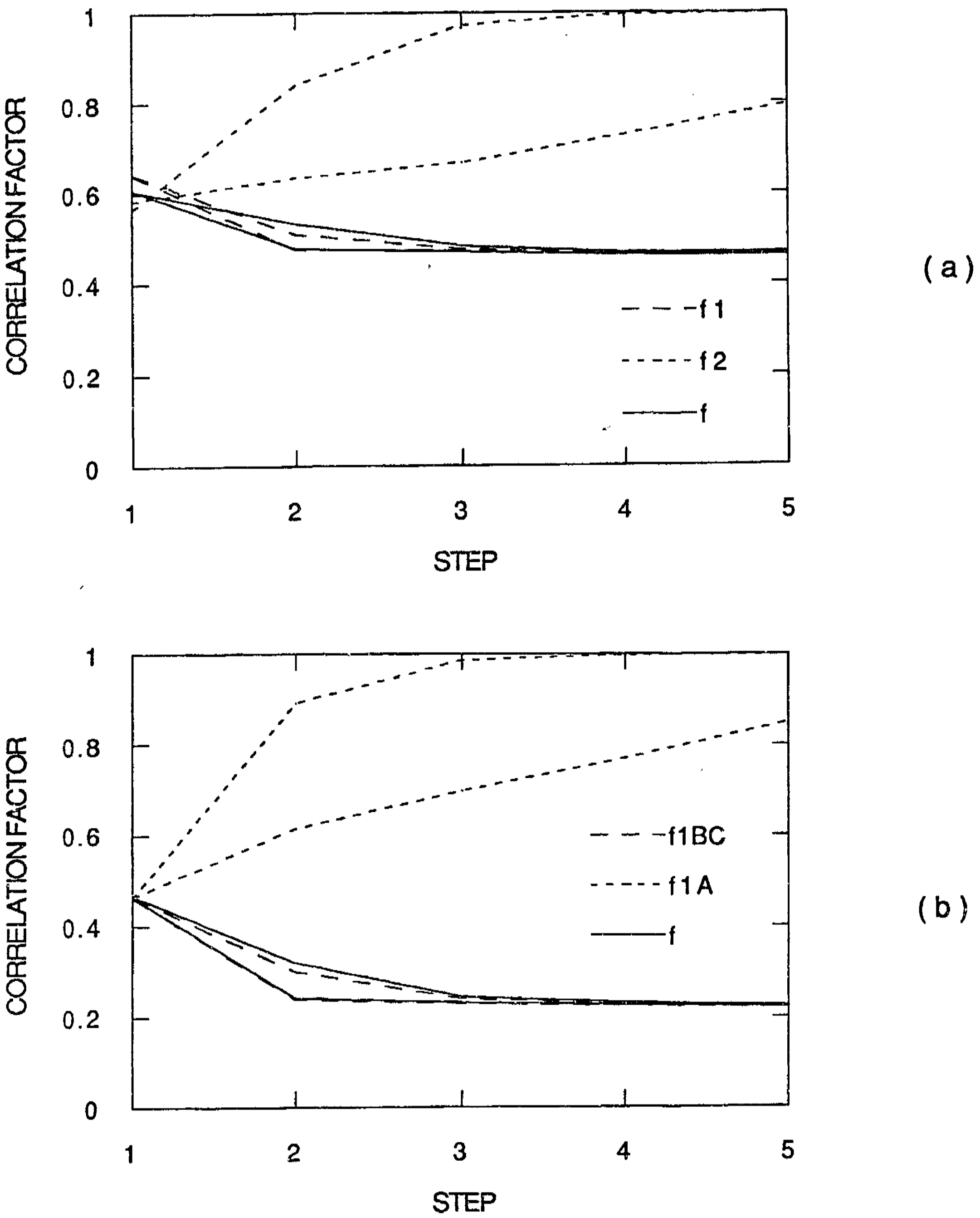

Figure 5-4: Calculated partial and total correlation factors as functions of effective dimensionality. From step 1 to 5, the system undergoes a transition (a) from a uniform slab (Fig. 5-3a) to a two-dimensional lattice (Fig. 5-4b); (b) from a two-dimensional lattice (Fig. 5-4b) to a set of two parallel paths (Fig. 5-4c). Two sets of curves were calculated at $T_m/T = 1.5$ (weaker T-dependence) and $T_m/T = 3.5$ (stronger T-dependence) respectively.

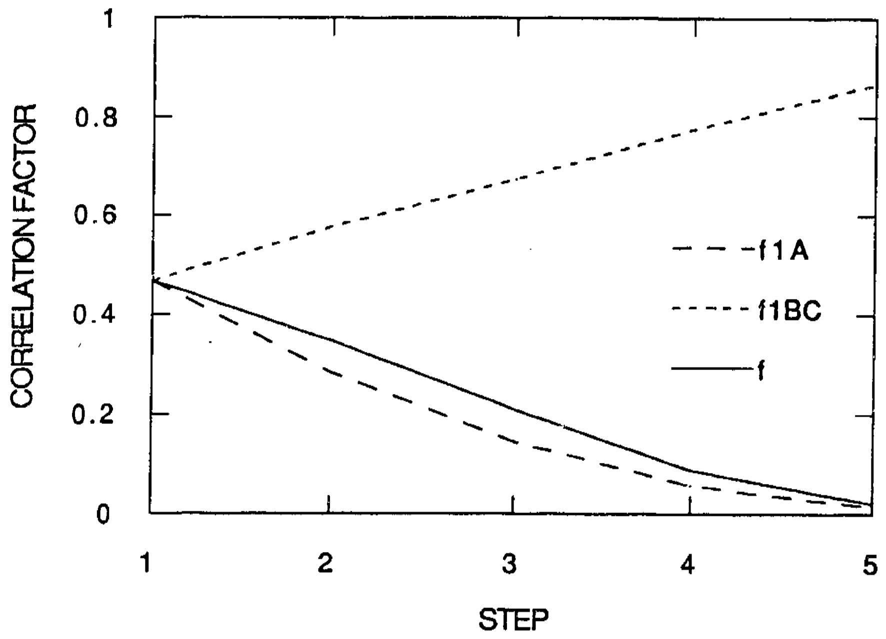

Figure 5-5: Calculated partial and total correlation factors at $T_m/T = 3.5$ as functions of effective dimensionality. From step 1 to 5, the system undergoes a transition from a two-dimensional lattice (Fig. 5-4b) to a set of one-dimensional isolated paths (Fig. 5-3d).

correlation factor further reduced.

One-Dimensional Confinement

Another interesting situation is when there exists individually isolated paths with particularly low activation energies. Depending on the energies of the surrounding sites, these paths are confined one-dimensionally to a certain extent. This case can be studied by lowering the energies of the 1A sites from those in the configuration in Fig. 5-3b. Again five steps were taken to achieve the configuration in Fig. 5-3d. As shown in Fig. 5-5, unlike the previous two cases, here the correlation factor is seen to change drastically as the energy well deepened. The total correlation factor follows the trend of the low energy path closely because vacancies spend most of their life time in the low energy path. Plotting the logarithm of f_{1A} (partial correlation factor of the path along 1A sites) and f against T_m/T in Fig. 5-6 for the configuration in Fig. 5-3d, it is easy to realize that the correlation factors are approximately associated with an "activation" energy. By measuring the slope of the curve at the low temperature end,

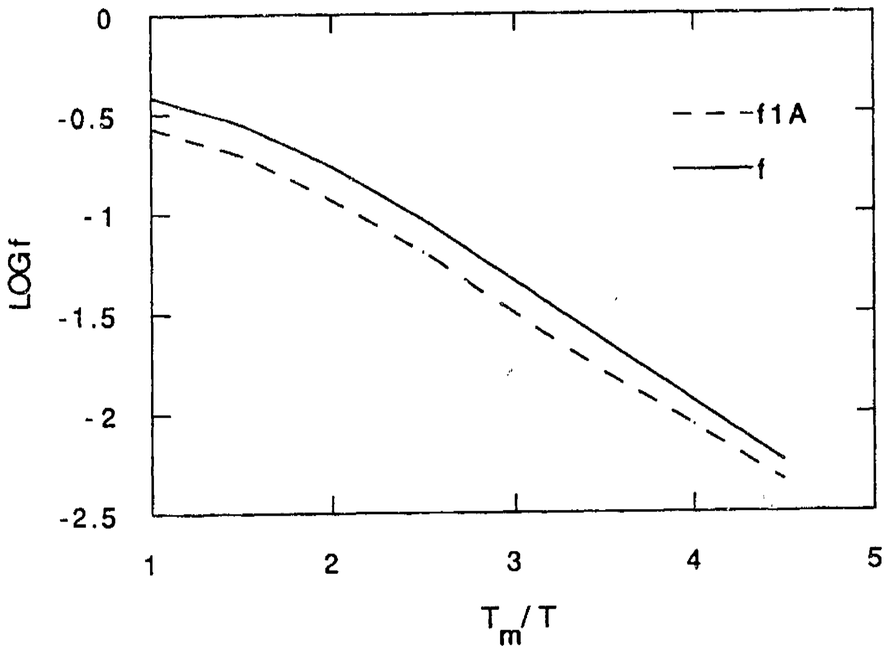

Figure 5-6: Calculated partial and total correlation factors as functions of temperature for the one-dimensional configuration in Fig. 5-3d.

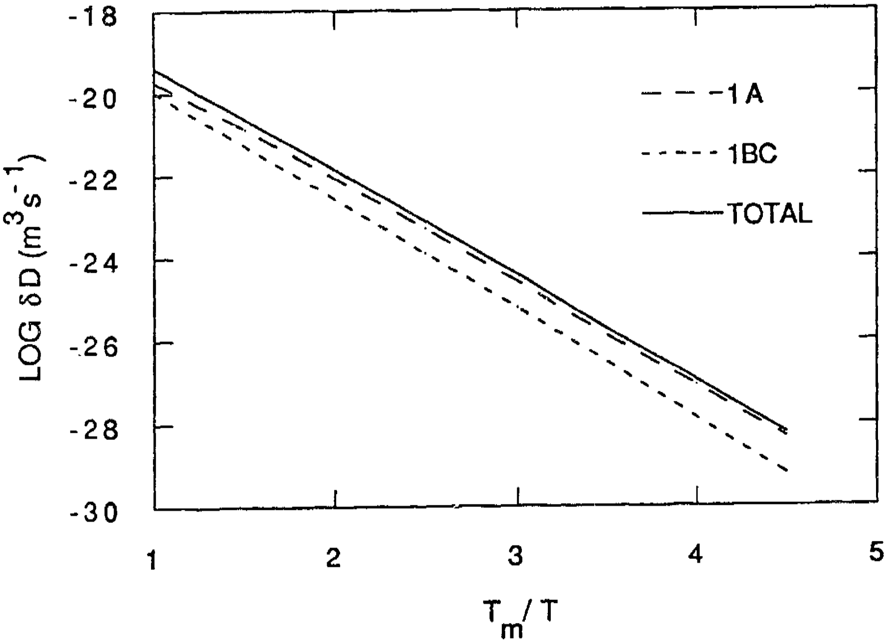

Figure 5-7: Calculated partial and total diffusivities as functions of temperature for the one-dimensional configuration in Fig. 5-3d.

it is found that this energy is 0.2 eV, which is the difference between the activation energy of the isolated path 1A and the adjacent paths 1B and 1C. The physical meaning is then clear: in order for the vacancy to make an effective exchange with the marked atom in the low energy path, it has to escape from the higher energy path to avoid cancellation of the initial exchange.

Fig. 5-7 illustrates the calculated Arrhenius plot for the partial and total diffusivities for the configuration in Fig. 5-3d. It is clear that although the low energy path has a small correlation factor, it remains as the dominant diffusion path. More interestingly, the diffusivities D_{1A} as well as D_M show approximately the activation energy of the higher energy path rather than that of the lower energy path. This means that despite the existence of such low energy paths, they do not show up in the diffusivity measurements. However, combined studies of the correlation factor and the diffusivity will reveal such paths.

From the above calculated results, the following conclusions can be made:

(1) For the uniform slab configuration, the total correlation factor f is close to that in a three-dimensional simple cubic lattice. As expected, f reduces to 0.47, the value for a two-dimensional square lattice as the vacancies are confined to the center atomic layer. It further reduces to ~ 0.2 if the two-dimensional lattice is divided into sets of parallel double paths, which corresponds to a more realistic situation than the previous two configurations as will be seen in Section 5.3.

(2) In the case of an isolated one-dimensional path, f approaches 0 as the energy well deepens, and it has a temperature dependence as if it is associated with an energy which approximately equals the activation energy difference between the isolated path and the coupled next lowest energy path. As a result, the diffusivity, D_M, has a characteristic activation energy corresponding to the coupled next lowest energy path.

(3) Therefore, if the vacancy mechanism is responsible for grain boundary diffusion, the correlation factor should be smaller than 0.3, which is smaller than the experimentally measured value ~ 0.54 by Robinson and Peterson [30]. This is in

contradiction to their argument that a large f implies a vacancy mechanism. In fact, since the correlation factor depends strongly on the grain boundary structure, it is insufficient to use f to determine the grain boundary diffusion mechanism.

(4) At low temperatures, low energy paths have overwhelming dominance. Therefore it is valid to treat the measured diffusivity as completely due to the low energy paths, which then allows a description of the diffusivity by the simple Arrhenius form. However, at high temperatures, vacancies can move back and forth between different paths, and the resulting diffusivities are then complicated linear combinations of the partial diffusivities of each path. To obtain the coefficients of the linear combinations, partial correlation factors are required, which are functions of temperature. As a result, the total diffusivity can not be decomposed into linear combinations of individual Arrhenius terms.

5.3 Grain Boundary Diffusion Mechanism

In order to understand the measured grain boundary diffusion results at the atomic level, computer simulations were performed to obtain realistic grain boundary structures and to explore the possible defect mechanisms and detailed jumping paths. Four boundaries ($\Sigma5\,(310)$, $\Sigma13\,(510)$, $\Sigma5\,(210)$ and $\Sigma13\,(320)$) were chosen for this study for the following reasons: (1) their tilt angles are more or less evenly distributed in the [001] tilt series, so that the general trend of the change in structure and diffusion properties could be established and compared to those observed experimentally; (2) both of the $\Sigma5$ boundaries consist of fast diffusion structural units (B and D), therefore they are especially important; (3) these four boundaries have the shortest periods (lengths of the unit vectors of the corresponding CSL's). It is therefore relatively easy to calculate their structures and defect energies, because the minimum number of atoms required in the sample system for a particular boundary is proportional to the square of the grain boundary period. In the following, the calculation method is briefly described, and then the calculated results are presented and discussed.

5.3.1 Method of Calculation

The Embedded Atom Method (EAM) [66, 67], which is known to generate relatively accurate activation energies for bulk self-diffusion [68], was employed in the calculations. In this method, the interaction among the atoms in a system is described by the standard EAM functions developed by Foiles, Baskes, and Daw [69, 70]. The conjugate gradient method [71, 72] was used to perform the static relaxation to obtain the minimum energy configuration of the relaxed structure.

A program developed by S.M. Foiles [73] was used in this study.

The Embedded Atom Method

By including the effects of many-body interactions, the EAM provides a rather realistic model for the interaction among atoms in metals. The method is based on the density-functional theory, which describes the total electron energy of a system by a functional of the total electron density. The electron density in the vicinity of a given atom is expressed as a sum of the density contributed by this atom and the electron density from all the surrounding atoms. The contribution from the surrounding atoms is assumed to be slowly varying as a function of position, and is approximated by a constant. Therefore, the energy of this atom is the energy associated with its own electron density plus the constant background density, which defines the embedding energy function. In addition, there is an electrostatic energy contribution due to core-core overlap, which is described by a short-range pair potential function. The embedding atom function and the pair potential function were determined by fitting to observed quantities, i.e., equilibrium lattice constant, sublimation energy, bulk modulus, elastic constant and vacancy formation energy in the lattice.

Calculation of Grain Boundary Structure

The tilt grain boundaries were created by generating unrelaxed bicrystals with the desired geometry. The optimal structures of the grain boundaries were determined by relaxing all atoms using molecular statics. Periodic boundary conditions were used in all three directions. The two grains were allowed to translate relative to each other both along the boundary and perpendicular to the boundary to allow full relaxation. The spacing between adjacent grain boundaries (due to periodic boundary conditions in the direction perpendicular to the grain boundary plane) was chosen to be twice the period along the grain boundary plane, so that the interaction between adjacent boundaries (due to the periodic boundary conditions) was negligible[1].

In order to find the global minimum energy configuration, different translation states were tested and in some cases, atoms were systematically added to or removed from the boundary to test the grain boundary stability. The lowest energy configuration represents the equilibrium grain boundary structure.

Calculation of Defect Formation and Migration Energies

Once the optimal grain boundary structures were found, a point defect, i.e., a vacancy or an interstitial was introduced into the system by removing an atom from a grain boundary site or adding an atom at a relatively open position in the grain boundary core (this position will be called an interstitial site) respectively, and then relaxing the entire system. The increase of the grain boundary energy gives the formation energy of the defect ε^f.

To calculate the vacancy migration energy, an atom located near the vacancy was moved by small steps toward the vacancy. After each movement, the atom was allowed to relax in the plane perpendicular to the migration path while all other atoms (except those in the two outermost planes) were allowed to relax in all directions. The difference in the total energy of the system between the equilibrium site and the saddle point is ε^m, the minimum energy required for migration.

It was found that the interstitials in these boundaries could move only by the so-called interstitialcy mechanism. In this process, the interstitial was moved toward a nearby grain boundary site and it simultaneously pushed the atom, which occupied that site, towards another interstitial site. The migration energy was obtained by relaxing the system at each small moving step to find the saddle point for the sequence.

---

[1] The extent of the strain field of a boundary in the lattice is approximately equal to the distance between adjacent grain boundary dislocations (St.Venant's Principle [19]).

By studying all possible defect formation sites and migration paths, the lowest activation energy paths were found for each mechanism in each boundary.

5.3.2 Calculated Results

Grain Boundary Structure

Calculated structures for the $\Sigma5\,(310)$ and $\Sigma13\,(510)$, and $\Sigma5\,(210)$ and $\Sigma13\,(320)$ boundaries are shown in Figs. 5-8 and 5-9 respectively. The grain boundary structures for the symmetric [001] tilt series were investigated previously by Vitek and co-workers [74] using the pair-potential method. They found that for each misorientation, there are two different metastable structures having very similar grain boundary energies.

Our calculated structures for the $\Sigma5\,(310)$, $\Sigma13\,(510)$, $\Sigma5\,(210)$ and $\Sigma13\,(320)$ boundaries correspond to Vitek's $\Sigma5\,(D)$, $\Sigma13\,(CCD)$, $\Sigma5\,(B')$ and $\Sigma13\,(AB')$ structures. Their $\Sigma5\,(D')$, $\Sigma13\,(CCD')$, $\Sigma5\,(B)$ and $\Sigma13\,(AB)$ structures were found to be unstable. The reason our calculation was able to differentiate between the two sets of states and therefore provide more certain results for the grain boundary structures may be that the EAM used in our calculation is more realistic than the pair-potential method used in Vitek's work.

The grain boundary energies as by-products of the calculation are also listed in the figures. They are in excellent agreement with Wolf's results [18].

Vacancy Formation and Migration Energies [2]

Vacancy formation energies and migration energies were calculated comprehensively for both the $\Sigma5\,(310)$ and $\Sigma13\,(510)$ boundaries. The results are shown in Figs. 5-10 and 5-11 and respectively.

For both boundaries, the formation energies of a vacancy in the grain boundary core in one atomic plane of the ABAB... stacking sequence are generally larger than those in the other atomic plane. For example, in Fig. 5-10 the atoms are more closely

---

[2] This part of the study was done in collaboration with J.B. Adams' group at University of Illinois at Urbana.

(a) $\Sigma = 5$ (310) $\gamma_b = 0.614$ J/m^2

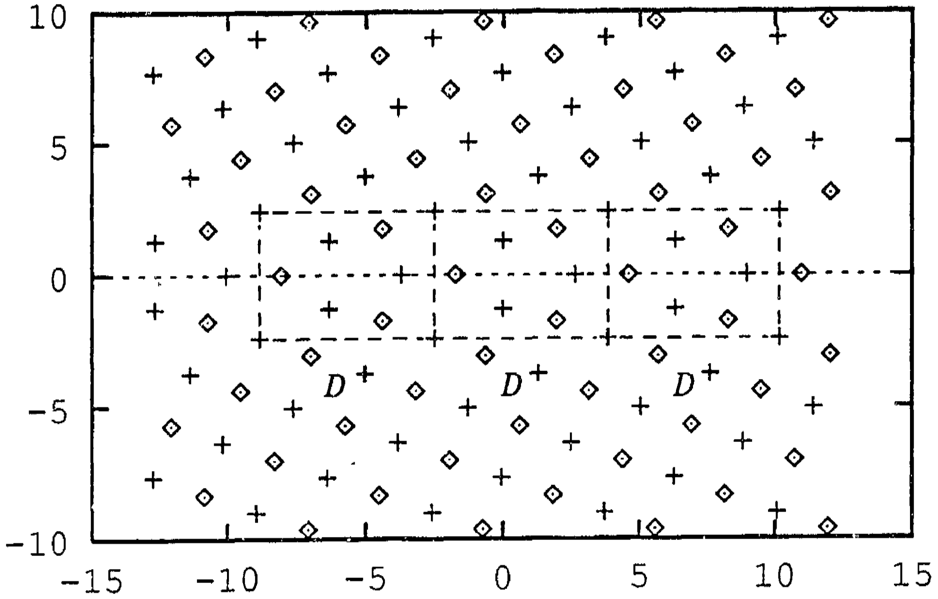

(b) $\Sigma = 13$ (510) $\gamma_b = 0.608$ J/m^2

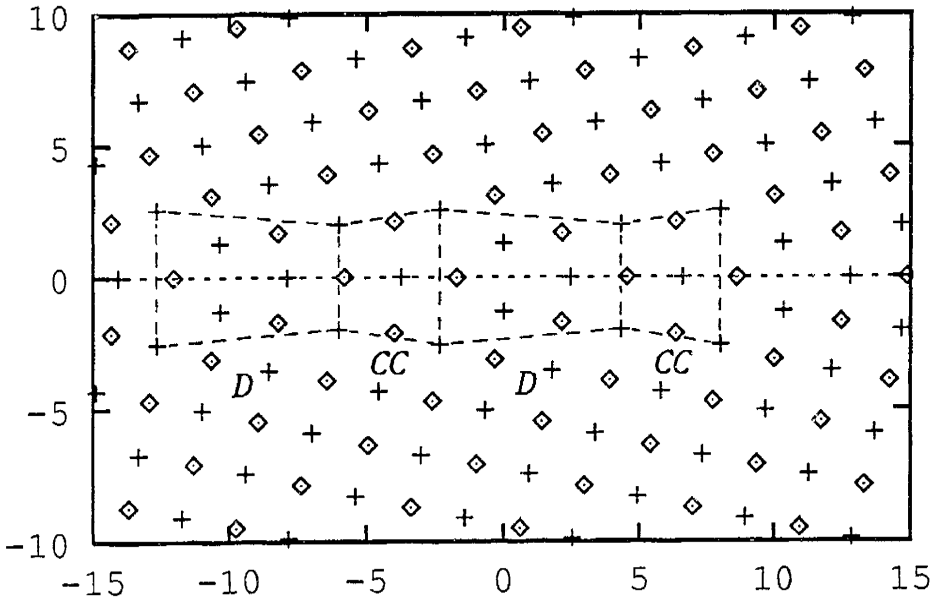

Figure 5-8: Calculated grain boundary structures viewed along [001] for the $\Sigma5(310)$ and $\Sigma13(510)$ boundaries, which consist of structural unit arrays ...*DDD*... and ...*CCDCCD*... respectively. Different symbols indicate ABAB... stacking sequence. The dimensions are in Å.

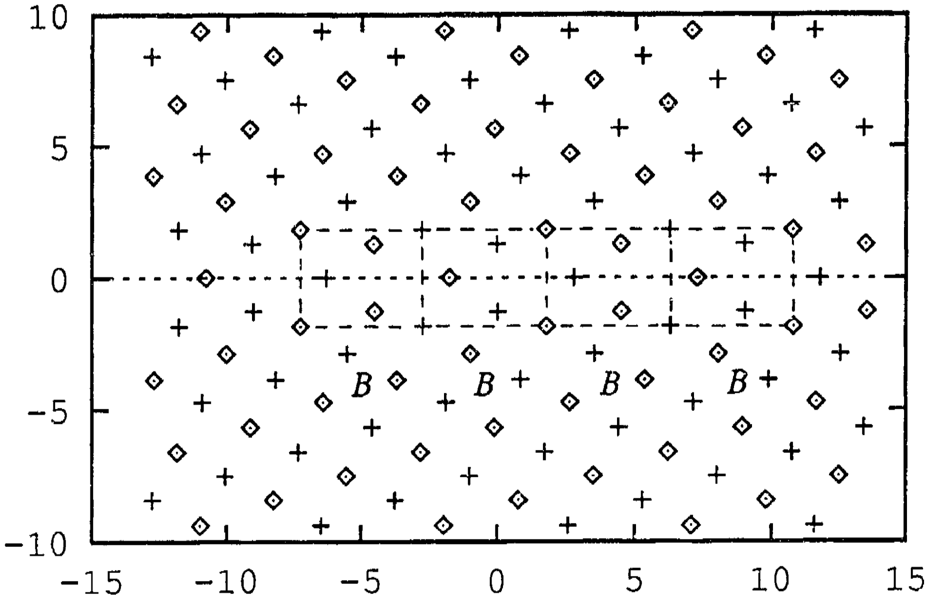
(a) $\Sigma = 5\ (210)$ $\gamma_b = 0.638\ \mathrm{J/m^2}$

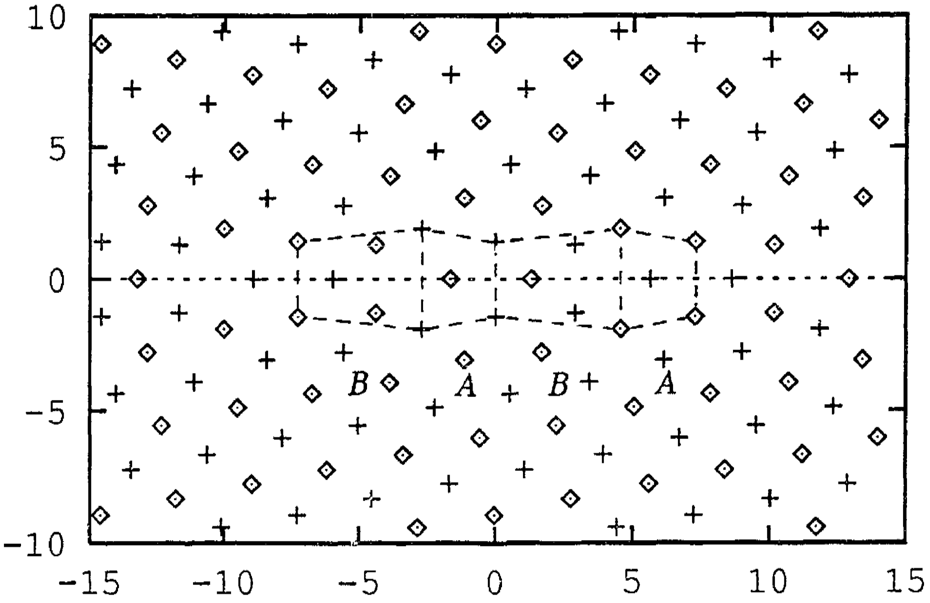
(b) $\Sigma = 13\ (320)$ $\gamma_b = 0.540\ \mathrm{J/m^2}$

Figure 5-9: Calculated grain boundary structures for the $\Sigma 5\,(210)$ and $\Sigma 13\,(320)$ boundaries, which consist of structural unit arrays ...*BBB*... and ...*ABAB*... respectively.

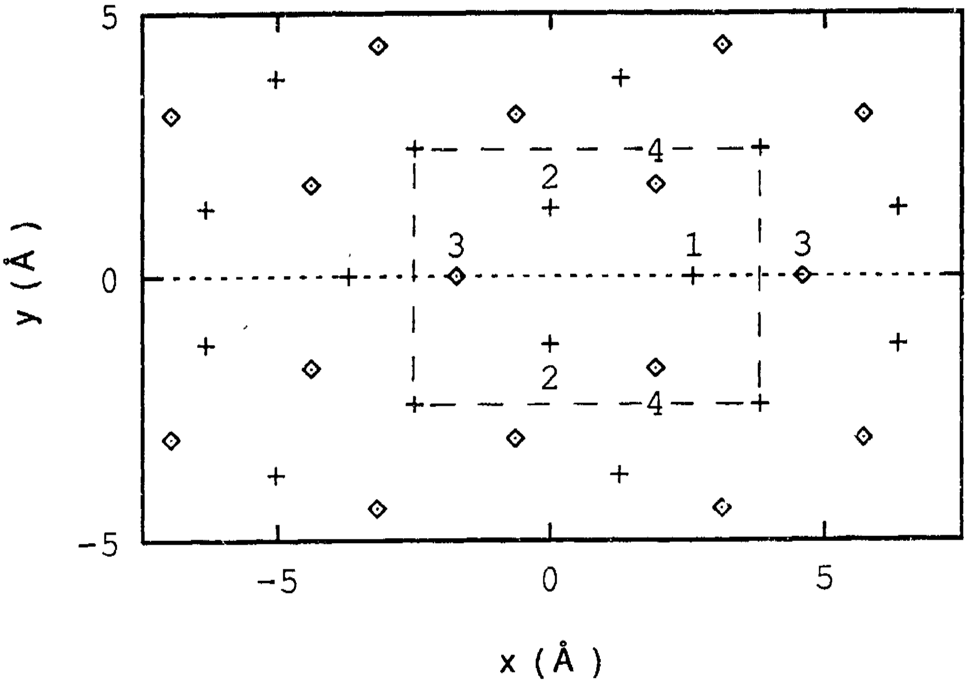

n (SITE No.)	ε^f (eV)	PATH	ε^m (eV)	ε (eV)
1	0.65	2 -- 2'	0.64	1.13
2	0.49	4 -- 4'	0.46	1.24
3	0.79	2 -- 4	0.61	1.39
4	0.78	4 -- 1	0.20	0.98
		1 -- 3	0.43	1.22
		3 -- 2	0.41	1.20

Site n' is the site one period away from site n along the z axis.

Figure 5-10: Calculated vacancy formation, migration and activation energies for various sites and paths in the $\Sigma 5\,(310)$ boundary.

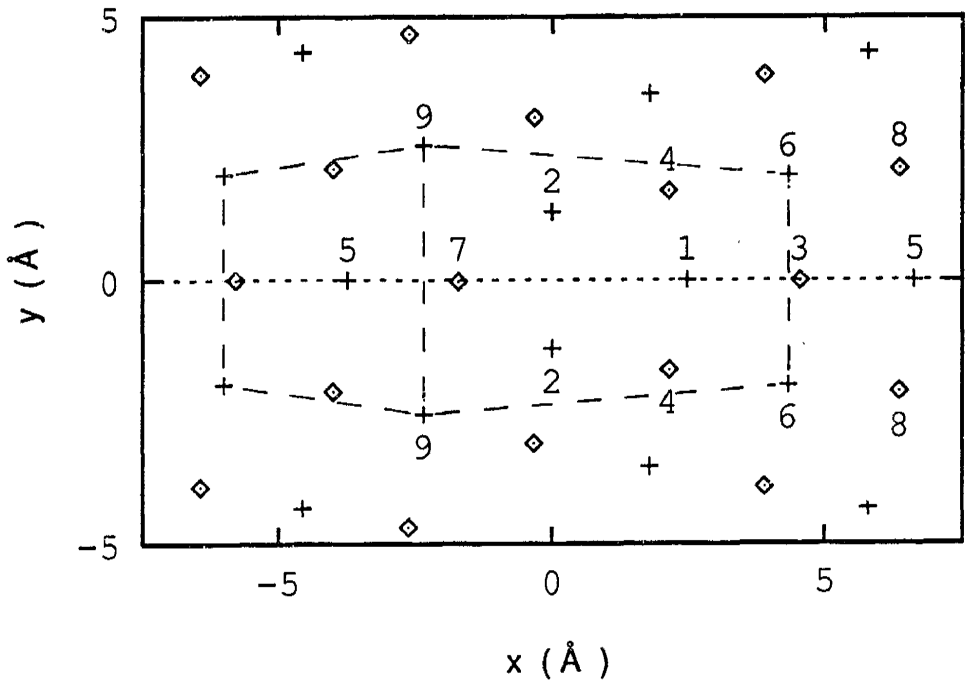

n (SITE No.)	ε^f (eV)	PATH	ε^m (eV)	ε (eV)
1	0.28	2 -- 1	0.46	0.99
2	0.53	2 -- 2'	0.52	1.06
3	1.27	4 -- 1	0.16	0.45
4	0.28*	4 -- 2	0.14	0.67
5	1.43	1 -- 1'	1.31	1.59
6	0.28*	3 -- 3'	1.72	2.99
7	1.31	5 -- 5'	1.18	2.61
8	1.01	7 -- 7'	1.81	3.12
9	0.53**	8 -- 8'	1.42	2.43

* Vacancy at site 9 reverts to site 2;

** Vacancies revert to site 1.

Figure 5-11: Calculated vacancy formation, migration and activation energies for various sites and paths in the $\Sigma 13\,(510)$ boundary.

spaced in the plane indicated by crosses than in the plane indicated by squares. Hence, the vacancy formation energy in the more compressed plane indicated by the crosses is lower. It is also clear that for the $\Sigma 13\,(510)$ boundary, both the formation energies and migration energies within the structural unit D are lower than those in the structural unit C. As a result, the paths within the structural unit D have considerably lower activation energies than those in the structural unit C.

As shown in Fig. 5-10, the lowest activation energy path in the $\Sigma 5\,(310)$ boundary is the split-path 1–4 ($\varepsilon = 0.98$ eV). However, this path is effectively a one-dimensional confinement case as discussed in Section 5.2.2, and therefore its correlation factor approaches 0. The next lowest activation energy path is the 2-2' parallel-path with activation energy 1.12 eV, which, according to the calculation in Section 5.2.2, has a correlation factor close to 0.2. Hence, the effective lowest activation energy path in the $\Sigma 5\,(310)$ boundary is the parallel-path (2-2') with an activation energy $\sim$ 1.12 eV.

The lowest activation energy path in the $\Sigma 13\,(510)$ boundary is the same type split-path 1–4 (0.45 eV) as shown in Fig. 5-11. However, in this case, there is another path 2–4 with higher energy (0.67 eV) coupled with the split-path. According to the discussion in Section 5.2, the coupled path network will then have an effective activation energy of about 0.67 eV, that of the higher energy path. Hence, the effective lowest activation energy path in the $\Sigma 13\,(510)$ boundary is the triple-split-path network with activation energy $\sim$ 0.67 eV.

Preliminary estimates gave values of the activation energies higher than 1.0 eV in both $\Sigma 5\,(210)$ and $\Sigma 13\,(320)$ boundaries.

Interstitialcy Mechanism

Inspecting the calculated grain boundary structures in Fig. 5-8 and 5-9, it is clear that there are rather open positions in the boundary cores, which could be interstitial sites. Fig. 5-12 and Fig. 5-13 show the relaxed structures around these sites after atoms were added to them. The formation energies for these interstitials are also shown in the figures.

Because there are no open channels in the boundaries, the interstitials have to

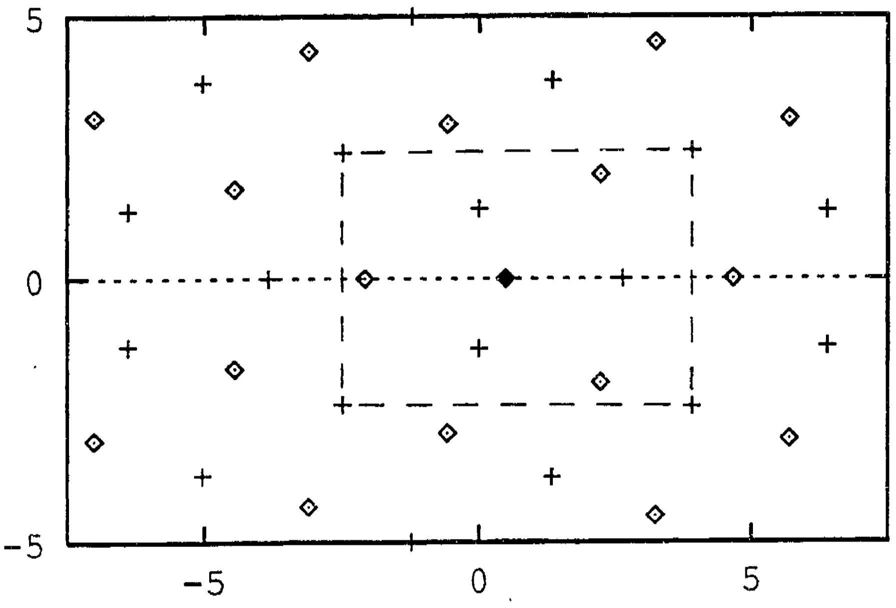

(a) $\Sigma = 5$ (310) $e^f = 0.24$ eV

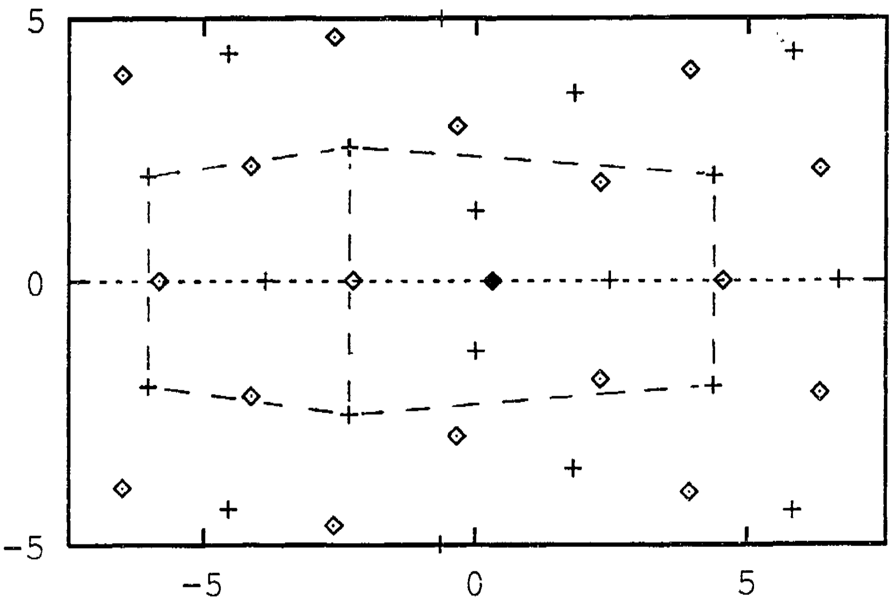

(b) $\Sigma = 13$ (510) $e^f = 0.014$ eV

Figure 5-12: Relaxes structures around interstitial sites for the (a) $\Sigma 5\,(310)$ and (b) $\Sigma 13\,(510)$ boundaries. The interstitial is represented by the solid diamond symbol.

(a) $\Sigma = 5$ (210) $e^f = 0.30$ eV

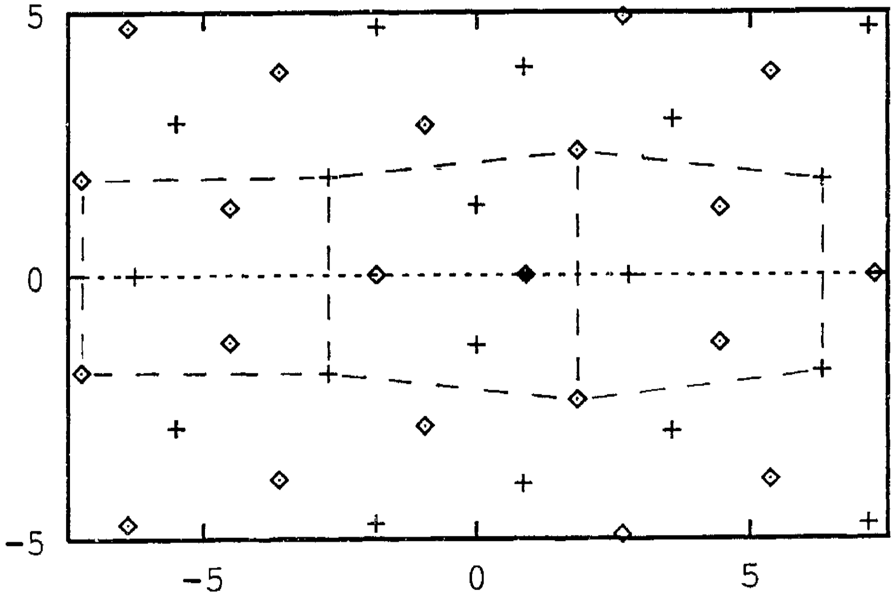

(b) $\Sigma = 13$ (320) $e^f = 0.09$ eV

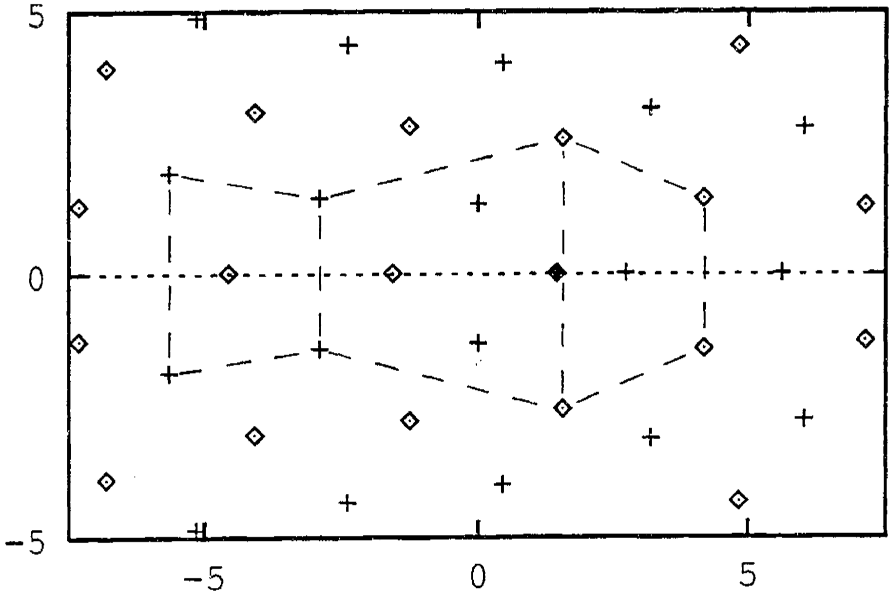

Figure 5-13: Relaxes structures around interstitial sites for the (a) $\Sigma5\,(210)$ and (b) $\Sigma13\,(320)$ boundaries.

move by an interstitialcy mechanism. Fig. 5-14 illustrates the interstitialcy diffusion paths in the $\Sigma5\,(310)$ boundary with a migration energy of 0.29 eV. The diffusion paths are again double-split paths as for the vacancy mechanism. However, in this case, the site at the intersection of the split paths is an interstitial site, so that a marked atom on this site can initiate a jump by itself. Therefore, the correlation factor for the paths is finite (does not approach 0 as in the vacancy mechanism case). In Section 5.4.1, the correlation factors for the interstitialcy mechanism in these boundaries will be analyzed in detail.

The diffusion paths in the $\Sigma13\,(510)$ boundary are essentially the same double-splits as in the $\Sigma5\,(310)$ boundary, but with a migration energy of only 0.12 eV.

Fig. 5-15 shows similar double-split paths in the $\Sigma5\,(210)$ and $\Sigma13\,(320)$ boundaries with migration energies of 0.42 and 0.74 eV respectively. However, in the $\Sigma13\,(320)$ boundary, there is a third parallel split path with a migration energy of 0.52 eV, which is coupled with the double-split paths. This third path, by itself, is a one-dimensional path, and therefore has a correlation factor approaching 0. As will be shown in Section 5.4.1, the effective migration energy of the triple-split-path network is determined by the double-split paths, and has the value 0.74 eV.

In summary, both vacancy and interstitialcy mechanisms were calculated for their activation energies in 4 representative boundaries in the [001] tilt series. The calculated activation energies are plotted together with the measured values in Fig. 5-16.

It is clear that the interstitialcy mechanism is preferred, i.e., it has lower activation energy than the vacancy mechanism in all of the 4 boundaries calculated. The agreement between measured and calculated activation energies for the interstitialcy mechanism is remarkably good except for the $\Sigma13\,(510)$ boundary.

It is also observed that the jumping paths for the interstitialcy mechanism are the same type of split paths in all 4 boundaries, and for both vacancy and interstitialcy mechanisms, the low activation energy paths are in the fast diffusion structural units, i.e., B and D. These observations are consistent with the predictions of the SU model.

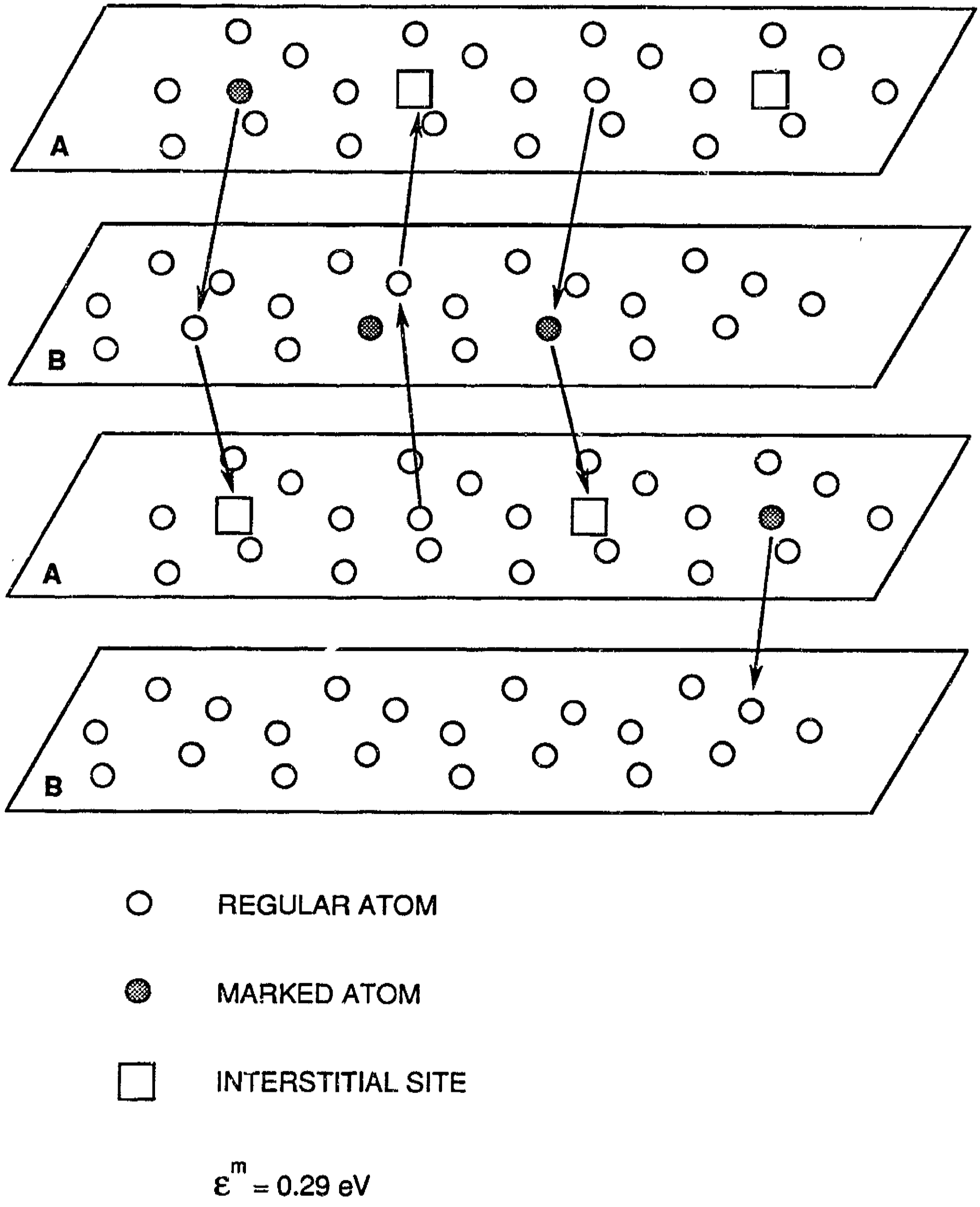

Figure 5-14: Interstitialcy jumping paths in the $\Sigma5\,(310)$ boundary. The sequence from left to right illustrates a marked atom diffusing by the interstitialcy mechanism along the double-split paths.

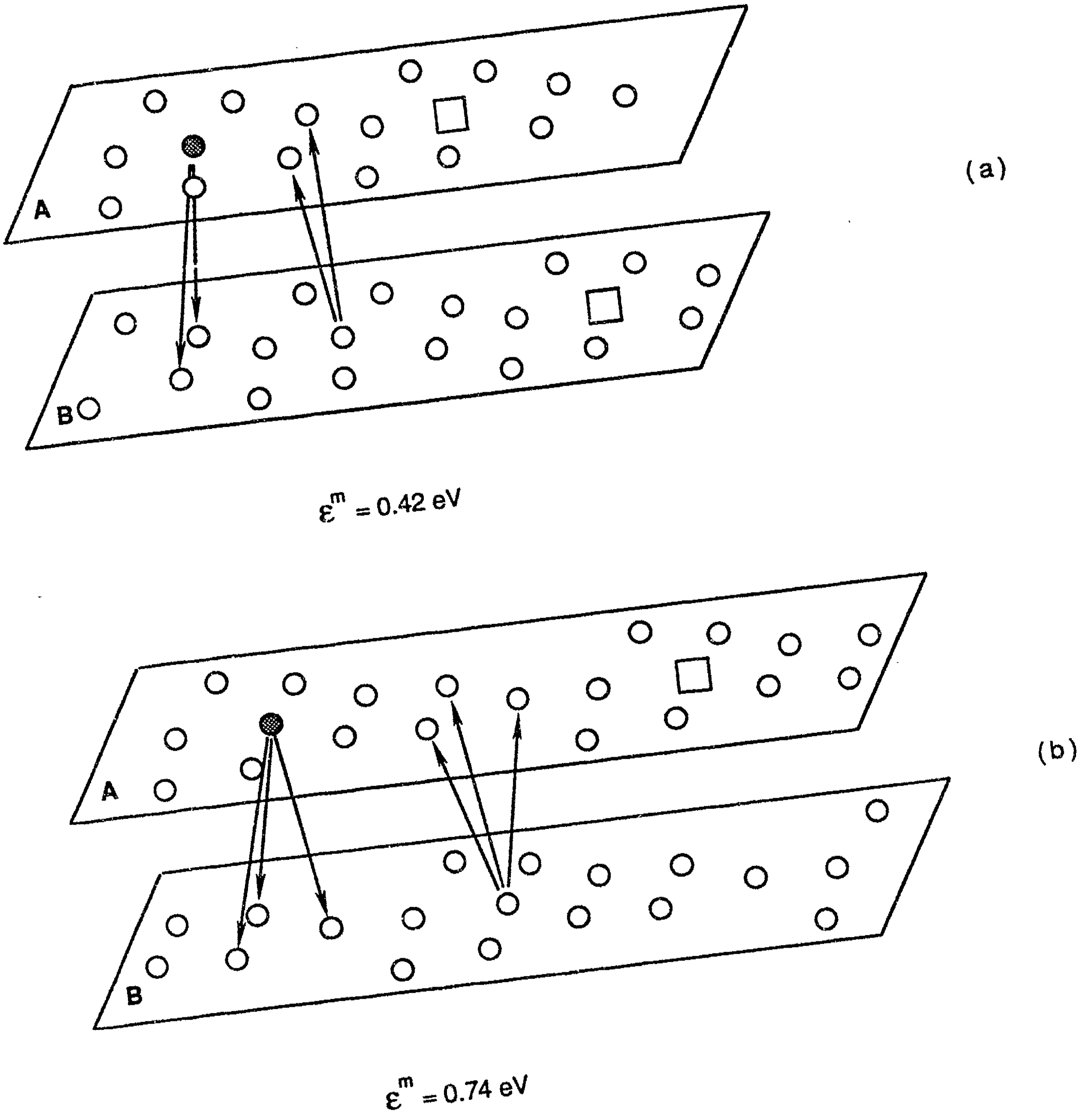

Figure 5-15: (a) The double-split interstitialcy jumping paths in the $\Sigma5\,(210)$ boundary; (b) The triple-split-path network for the interstitialcy mechanism in the $\Sigma13\,(320)$ boundary.

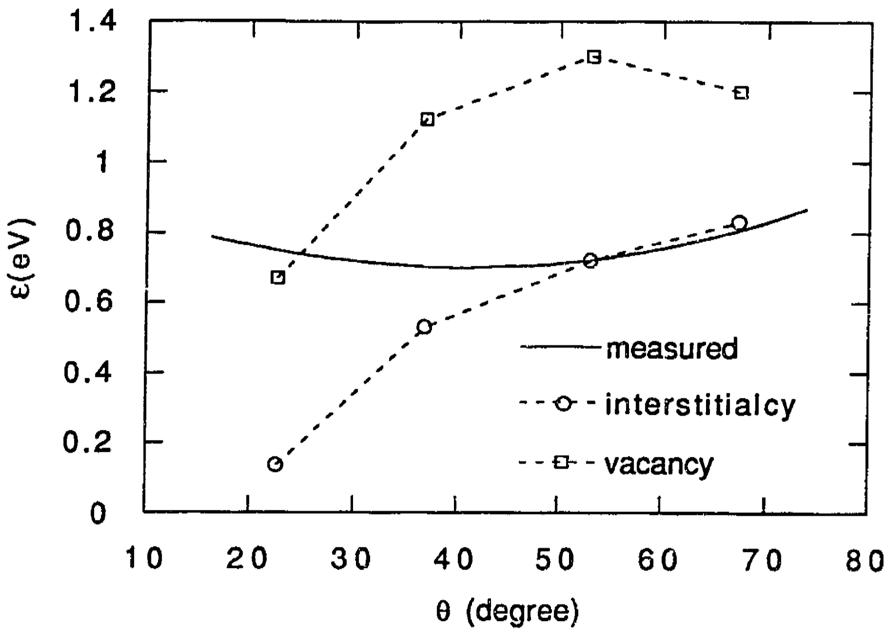

Figure 5-16: Calculated and measured activation energies for the symmetric [001] tilt boundary series.

5.4 The Pre-Exponential Factor

In Section 4.2, the grain boundary diffusion parameters measured in different temperature regions (or different kinetic regimes) were plotted together in an Arrhenius diagram as shown in Fig. 4-6. An interesting observation is that the overall diagram has an upward curvature, so that the D_b^0's measured at high temperatures are several orders of magnitude larger than those measured at low temperatures. In this section, we will first estimate D_b^0's for the symmetric [001] tilt boundaries calculated in the last section, and compare the results with measured D_b^0's. Then we will discuss different possibilities that could lead to the overall curvature.

5.4.1 Estimation of $\delta_b D_b^0$ for [001] Tilt Boundaries

The calculated results in the last section show that the interstitialcy mechanism is responsible for the fast diffusion along [001] tilt boundaries at low temperatures. For the $\Sigma5\,(310)$, $\Sigma13\,(510)$ and $\Sigma5\,(210)$ boundaries, the symmetric double-split paths are the lowest activation energy paths, and for the $\Sigma13\,(320)$ boundary, there is a third split path with a lower activation energy than the symmetric double-split paths.

A triple-split-path network model is used for the calculation of $\delta_b D_b^0$ for the symmetric double-split paths and the third single path. For the $\Sigma5\,(310)$, $\Sigma13\,(510)$ and $\Sigma5\,(210)$ boundaries, let the single path have a higher migration energy, so that its contribution to diffusion is negligible. For the $\Sigma13\,(320)$ boundary, the single path is given a lower migration energy corresponding to the energy calculation results.

The general formulation is provided in section 5.1. From Eq. 5.32, the contribution to diffusion by each type of path can be expressed as

$$\delta_b D_{M\alpha} = \delta_S d_\alpha C^i \Gamma_\alpha^{icy} z_\alpha^2 (f_{\alpha 1} + f_{\alpha 2})/N \ , \tag{5.41}$$

where δ_S is the thickness of an artificial grain boundary slab (see discussion at the end of this section), d_α is the degeneracy of the type-α path ($d_\alpha = 2$ and 1 for the double-split paths and the third path respectively), C^i is the occupation probability of an interstitial site, Γ_α^{icy} is the frequency of an interstitial making interstitialcy jumps along a type-α path, $z_\alpha = 0.5a = 2$ Å is the jumping distance in the tilt axis direction, $f_{\alpha 1}$ is the partial correlation factor of a jump along a type-α path if the marked atom is initially at a grain boundary lattice site, and $f_{\alpha 2}$ is the partial correlation factor if the marked atom is the interstitial that initiates the jump, and N is the total number of grain boundary lattice sites in the artificial grain boundary slab within a unit cell.

According to Boltzmann statistics,

$$C^i = \exp\left(-\frac{g^f}{kT}\right) = \exp\left(-\frac{s^f}{k}\right)\exp\left(-\frac{\varepsilon^f}{kT}\right) \ , \tag{5.42}$$

where g^f, s^f and ε^f are the Gibbs free energy, entropy and energy of interstitial formation. Since adding an atom at the interstitial site causes only very small distortion in the vicinity as seen in Section 5.3, the change of the vibration frequency is small. Therefore, it is reasonable to assume $s^f \sim 0$.

The jumping frequency can be expressed as

$$\Gamma_\alpha^{icy} = \nu_\alpha^0 \exp\left(-\frac{g_\alpha^m}{kT}\right) = \nu_\alpha^0 \exp\left(-\frac{s_\alpha^m}{k}\right)\exp\left(-\frac{\varepsilon_\alpha^m}{kT}\right) \ , \tag{5.43}$$

where g_α^m, s_α^m and ε_α^m are the Gibbs free energy, entropy and energy of interstitial migration by the interstitialcy mechanism. The "attempt" frequency ν_α^0 is approximately equal to the Debye frequency in the lattice. The migration entropy s_α^m is estimated using Zener's formula (Eq. 5.37) with $\beta_z = 0.5$ [3].

The correlation factors can be calculated by using a method similar to that described in Section 5.2, with the difference that in this case, a jump is initiated by an interstitial, which can be the marked atom itself or an ordinary atom.

Fig. 5-17 illustrates the the total correlation factor calculated at $T_m/T = 3.5$ as a function of

$$\Delta\varepsilon^m = \varepsilon_S^m - \varepsilon_D^m$$

where ε_S^m and ε_D^m are the migration energies along the third single path and along the double-split paths respectively. For the $\Sigma5\,(310)$, $\Sigma13\,(510)$ and $\Sigma5\,(210)$ boundaries, the third single path has a considerably higher migration energy, so the total correlation factor f has the value 0.67. As ε_S^m decreases, the total correlation factor gradually increases and reaches a maximum of 0.806 at $\varepsilon_S^m = 0$, which corresponds to the situation of three equivalent paths in the network. When ε_S^m continues to decrease, the diffusion is quickly dominated by the single path. But the cancellation in this path becomes severe, so that the total correlation factor decreases rapidly.

The total correlation factor f and the partial correlation factor of the single path f_S for $\Delta\varepsilon^m = 0.2$ eV are plotted as functions of T_m/T in Fig. 5-18. These functions have the same characteristics as those in the one-dimensional confinement case in Section 5.2, which indicates that the correlated walk for both the vacancy mechanism and the interstitialcy mechanism are similar in nature. The slopes of the lower parts of the f_S and f curves give an energy of about 0.2 eV, which is, as expected, the migration energy difference between the two types of paths.

The lower part of the partial correlation factor f_S curves can be approximately expressed by

$$f_S = f_S^0 \exp\left(-\frac{\Delta\varepsilon^m}{kT}\right) \qquad (5.44)$$

---

[3] See arguments in Section 5.2.

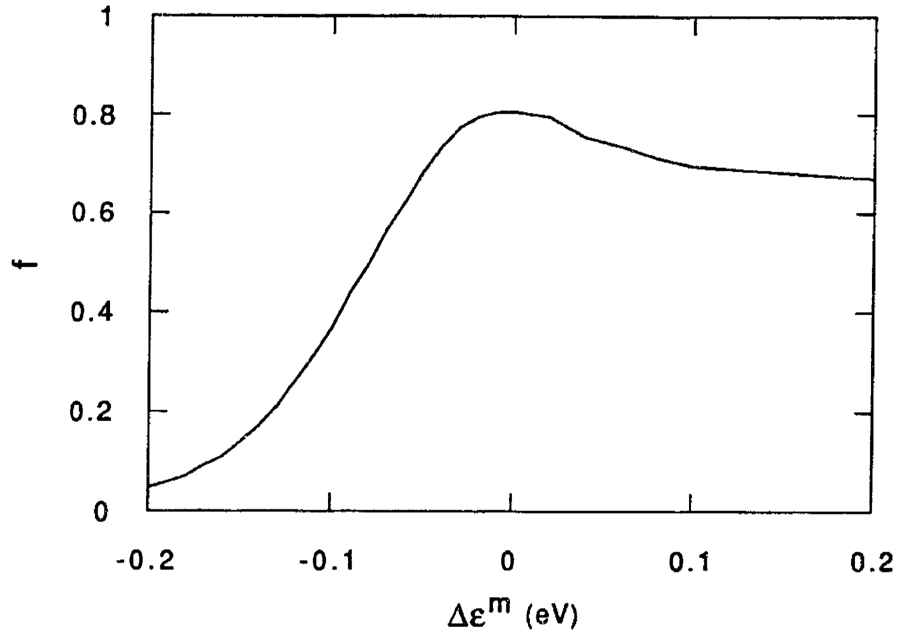

Figure 5-17: Total correlation factor as a function of the migration energy difference between the single path and the double-split paths at $T_m/T = 3.5$.

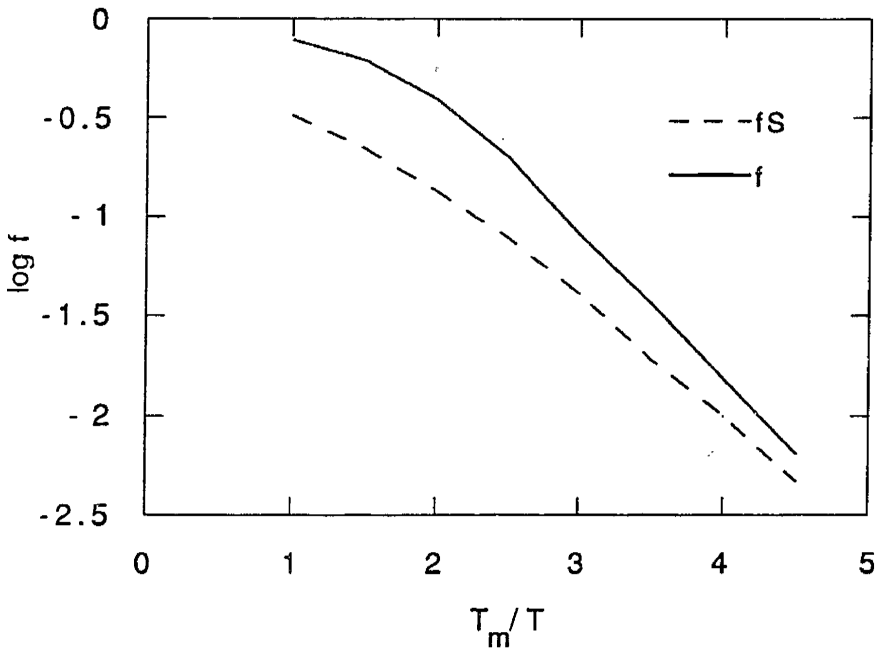

Figure 5-18: Temperature dependence of the total correlation factor f and the partial correlation factor f_S for the $\Sigma 13\,(320)$ boundary with $\Delta\varepsilon^m = 0.2$ eV.

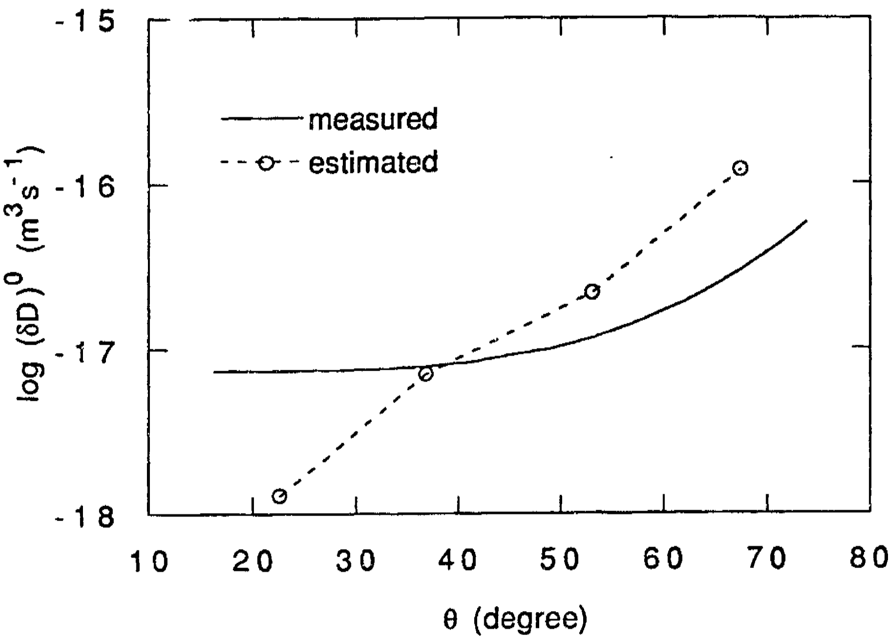

Figure 5-19: Estimated and measured $\delta_b D_b^0$'s for the symmetric [001] tilt boundary series.

with $f_S^0 \approx 1$.

The pre-exponential factors of diffusion parameter can then be estimated by using the parameters listed in Table 5.1 and the following formula:

$$\delta_b D_b^0 = \frac{\delta_S \nu_D a^2}{4N} \exp\left(\frac{s^f}{k}\right) \left[2 \exp\left(\frac{\beta_Z \varepsilon_D^m}{kT_m}\right) f_D + \exp\left(\frac{\beta_Z \varepsilon_S^m}{kT_m}\right) f_S^0\right] . \tag{5.45}$$

The resulting values of $\delta_b D_b^0$ are plotted with the measured values in Fig. 5-19. The agreement between the theoretically estimated values and the experimentally measured values must be regarded as excellent with respect to both the overall magnitude and the trend of the angular dependence. This agreement, together with the agreement of calculated and measured activation energies, implies that our understanding of the atomic transport process in the [001] tilt boundaries is essentially correct with respect to both mechanism and kinetics.

parameter	δ_S (Å)	ν_D (s^{-1})	a (Å)	s^f (k)
value	10	4×10^{12}	4.0	0
parameter	β_Z	T_m K	ε_l^m eV	
value	0.5	1300	1.0	
parameter	Σ5 (310)	Σ13 (510)	Σ5 (210)	Σ5 (320)
ε_D^m (eV)	0.29	0.12	0.42	0.74
ε_S^m (eV)	NA	NA	NA	0.52
N	15	25	10.5	18
f_D	0.67	0.67	0.67	1.0
f_S^0	NA	NA	NA	1.0
n^l	2	2	2	3
n^i	1	1	1	1
$\delta_b D_b^0$ ($m^3 s^{-1}$)	7.0×10^{-18}	1.3×10^{-18}	2.2×10^{-17}	1.2×10^{-16}
δ_b (Å)	2.0	1.2	2.9	2.2

Table 5.1: Parameters used in estimating $\delta_b D_b^0$ and δ_b, and the estimated results.

Grain Boundary Width

It should be noted here that in the above estimation, although $\delta_S = 10$ Å was used, it does not necessarily represent the real physical width δ_b for grain boundary diffusion. In fact, the value of δ_S could be arbitrarily chosen without affecting the results, because the number of grain boundary lattice sites N is proportional to δ_S.

The question of the grain boundary width has always been interesting because the vast majority of the experiments on grain boundary diffusion yield only the product $\delta_b D_b$. Knowledge of δ_b is therefore important for the interpretation of grain boundary diffusion results.

In the past, the values of δ_b were based on structural analyses such as observations by using FIM [75] and TEM [76] and measurements by X-ray diffraction techniques [77], which generated the thickness of grain boundary cores (regions of mismatch) or the extent of the strain fields associated with grain boundaries. The grain boundary widths were found to be in the range of 5 to 10 Å generally. A direct determination of δ_b is possible by using diffusion methods, but it has only been made for NiO with the result $\delta_b = 7$ Å [78] and $3 - 6$ Å [79].

It should be realized that δ_b in oxides may be quite different from that in metals, and the values estimated by structural analyses do not necessarily represent values appropriate for diffusion, because even in the grain boundary core regions, the fast diffusion paths are limited, and the relative contribution of each path to diffusion changes as the temperature changes, as we see in this chapter. It seems more appropriate to define the grain boundary width for diffusion as the fraction of space occupied by the sites that are involved in the dominant diffusion paths, or

$$\delta_b \equiv \delta_S \frac{n_p}{N} , \tag{5.46}$$

where n_p is the number of sites involved in the fast diffusion paths. By using $n_p = n^l + n^i$ (listed in Table 5.1), δ_b is estimated for the 4 boundaries (also listed in Table 5.1). The resulting values suggest that δ_b is close to the thickness of one atomic layer, which is considerably less than 10 Å. It should be mentioned here that these values only represent the low temperature boundary widths. As the temperature rises, more diffusion paths could become important, and therefore the value of δ_b would increase.

5.4.2 Possible Explanations for the Upward Curvature of the Arrhenius Diagram

As indicated in the earlier sections in this chapter, a deviation from a straight-line Arrhenius diagram is expected due to the existence of different atomic jumping paths in the grain boundary (see Eq. 5.13). However, any significant deviation requires that the high activation energy paths dominate the high temperature region, which is possible only if these paths are associated with D_b^0's substantially larger than those of the low activation energy paths which dominate the low temperature region. By applying the simple kinetic theory used in the last section, it is easy to estimate that a diffusion parameter of $\sim 10^{-14}$ m^{3}s^{-1} (from the high temperature diffusion data represented by the dashed line in Fig. 4-6) requires that within a 20 Å thick boundary slab, every possible path has $\varepsilon_b^m = 0.7$ eV ($\varepsilon_b = 1.0$ eV from the high temperature diffusion data), and $f = 1.0$, if other parameters (a, ν_D, s^f and β_Z) are the same as used in estimating D_b^0 at low temperatures (see Table 5.1). Note that both ε_b^m and f are assumed so as to maximize D_b^0. Since it is highly unlikely that all paths in such a thick region will have an activation energy of 1.0 eV [4], it is clear that such a large D_b^0 cannot be explained by using simple kinetics arguments.

In the following, several possible reasons for such a large upward curvature are discussed.

Temperature Dependence of the Activation Parameters

It should be realized that the simple kinetic theory used in Section 5.4.1 to explain the low temperature values of D_b^0 is based on the harmonic approximation of atomic interactions[5], i.e., a point defect is assumed to be in a truncated harmonic energy well. This approximation is expected to fail at high temperatures because in reality, only the bottom of the energy well is approximately harmonic. The resulting anharmonicity which manifests itself, e.g., in thermal expansion, gives rise to an increasing relaxation of the defect with increasing temperature. The reduction of the vibration frequencies associated with this relaxation causes the entropy of defect activation to increase with an increase in temperature. This increase in entropy is coupled with a corresponding increase of the activation enthalpy[6] as required by the following thermodynamic relation:

$$T\left(\frac{\partial s}{\partial T}\right)_p = \left(\frac{\partial h}{\partial T}\right)_p \quad . \qquad (5.47)$$

This model has been proposed by Gilder and Lazarus [80] in order to explain observed non-Arrhenius diffusion behavior of lattice diffusion in metals. By proposing

---

[4] In fact, the calculations in section 5.3 show that only a very limited number of paths have activation energies below 1.0 eV.

[5] Although Zener's theory of D^0 is based on anharmonicity effects, it is limited to the temperature dependence of the elastic modulus only: the activation entropy and enthalpy are assumed to be constant.

[6] In this discussion, activation enthalpy is used instead of activation energy for a more rigorous treatment.

that in metal systems, the thermal coefficient of expansion of an activated vacancy is given by $\beta^v = \frac{1}{V^v}\left(\frac{\partial V^v}{\partial T}\right)_p = 1/T$ (V^v is the activation volume of a vacancy), they derived the following expressions for the activation enthalpy and entropy as functions of temperature:

$$h_l^v(T) = h_l^v(T_0) + \frac{1}{2}\mu_l(T^2 - T_0^2) \ , \tag{5.48}$$

and

$$s_l^v(T) = s_l^v(T_0) + \mu_l(T - T_0) \ , \tag{5.49}$$

where $\mu_l = \frac{1}{T}(\frac{\partial h_l^v}{\partial T})_p$ is the coefficient of the vacancy specific heat. Therefore, the temperature dependence of the diffusivity is given by

$$D_l = D_l^0(T) \exp\left[-\frac{h_l^v(T)}{kT}\right] \ , \tag{5.50}$$

where

$$D_l^0(T) = gf\nu_0 a^2 \exp\left[\frac{s_l^v(T)}{k}\right] \ . \tag{5.51}$$

If we assume that the above relations are valid for grain boundary diffusion, and use $h_b(T = 400K) = 0.7$ eV and $h_b(T = 800 \text{ K}) = 1.0$ eV, from Eq. 5.48 ,we have

$$\mu_b \sim 10^{-6} \text{ eV K}^{-2} \ ,$$

which, through Eq. 5.49 and 5.51, gives

$$\delta_b D_b^0 (T = 800 \text{ K}) \sim 10^{-14} \text{ m}^3\text{s}^{-1} \ ,$$

where $\delta_b = 5$ Å is used for the evaluation. However, the value of μ_b obtained above is considerably larger than that obtained for lattice diffusion ($\mu_l = 10^{-9} - 10^{-10}$ eV K^{-2}), which raises the question about the physical feasibility of the above argument for grain boundary diffusion. According to Gilder and Lazarus [80],

$$\mu = 2\beta^v \gamma c_v \Delta V/\Omega \ , \tag{5.52}$$

where γ is the Gruneisen constant, c_v is the specific heat at constant volume per atom without vacancies, ΔV is the volume change of the system due to introduction of a vacancy and Ω is the volume occupied by one atom. None of the above quantities for grain boundary can differ greatly from those of lattices, therefore, it is unlikely that μ_b can have a value which is orders of magnitude larger than μ_l, although qualitatively a larger μ_b is consistent with the fact that the energy wells in the grain boundaries are shallower and usually of lower symmetry resulting in larger anharmonicity effects. Therefore, the anharmonicity effect must have contributed to the non-Arrhenius behavior of grain boundary diffusion, but it alone is probably not enough to produce the observed large magnitude of the upward curvature.

Multiple Diffusion Mechanisms

The curvatures of the Arrhenius diagrams for lattice diffusion could also be attributed to the simultaneous contribution of mono- and divacancies to the diffusivity. The diffusion coefficient is then given by

$$D_l = D_l^{1v} + D_l^{2v} , \tag{5.53}$$

where D_l^{1v} and D_l^{2v} denote the mono- and divacancy contributions, respectively. Since the monovacancy mechanism has a lower activation enthalpy than the divacancy mechanism, it will always dominate at low temperatures. With increasing temperature, the relative contribution of divacancies increases and therefore causes an upward curvature of the Arrhenius diagram. This model is supported by evidence accumulated from quenched-in defect studies [81] and isotope effect measurements [82].

In a grain boundary, the formation energies for various defects are considerably lower than in the lattices, which implies that the probabilities of thermal excitation of various types of defect-complexes are much higher. These defect-complexes give rise to longer range relaxations in their neighborhoods. Therefore, they are associated with a significantly larger formation and migration entropy, which leads to larger pre-exponential factors. Consequently, these defects with larger pre-exponential factors could contribute significantly, or even dominate at high temperatures, causing a large curvature of the Arrhenius diagram. Clearly, the multi-mechanism effects should be much stronger in grain boundaries than in the lattice.

The molecular statics calculations in Section 5.3 indicate that the interstitialcy mechanism is favored over the vacancy mechanism due to its lower activation energy, and that it therefore dominates the low temperature diffusion process. However, at high temperatures, due to possible large pre-exponential factors, the vacancy mechanism (or mechanisms involving defect-complexes), such as divacancies and vacancy-interstitial pairs could become important. Fig. 5-20 illustrates a possible vacancy-interstitial pair mechanism: First, a vacancy-interstitial pair is excited from the initial defect free grain boundary structure. Then the vacancy jumps to the same level of the interstitial. This jump is facilitated by the presence of the interstitial, which reduces the formation energy of vacancy at a nearby site. Next, the vacancy makes another jump to a lower level. Finally, the interstitial annihilates the vacancy at two levels below the original position.

It is noted that the phenomena discussed above are complementary. In a real system, both anharmonic effects and multi-mechanism effects must co-exist. Large anharmonic effects make the excitation of defects easier, therefore helping the existence of multiple defect mechanisms. Defect complexes possess more complicated structures, and therefore are more severely affected by anharmonic effects. It is observed [1] that grain boundary diffusion data extrapolate approximately to the diffusivity in the liquid state at T_m. This suggests that the grain boundary structure and diffusion properties gradually approach that of the liquid state as the temperature approaches T_m. However, it is also observed (Hsieh and Balluffi [85]) that true grain boundary melting does not occur until T_m is reached. Theses results suggest that the boundary structure at elevated temperatures, while not yet completely liquid-like, is indeed highly defected and possess considerable anharmonicity. It seems possible that the observed upward curvature of the Arrhenius diagram is consistent with the development of such a relative disordered structure at high temperatures.

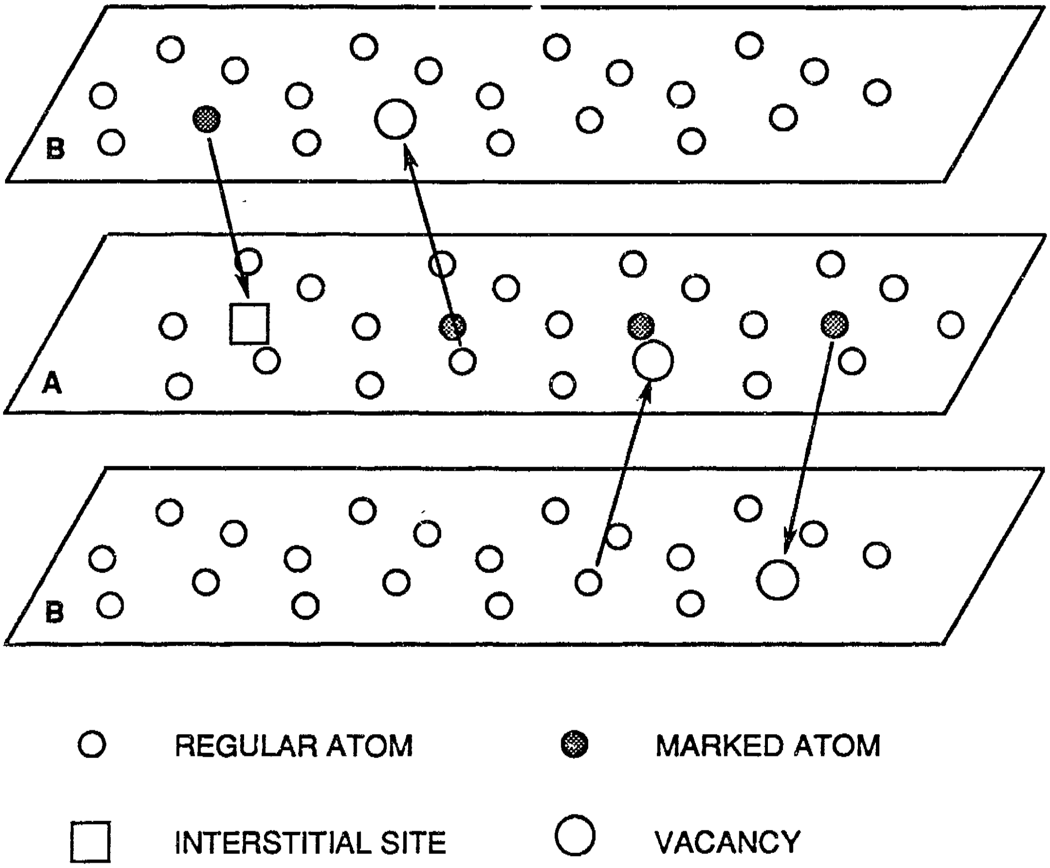

Figure 5-20: Illustration of a possible vacancy-interstitial pair mechanism. A jumping sequence is shown in several steps from the left to the right.

Chapter 6

Conclusions

6.1 Methodology

- The newly developed multi-crystal surface accumulation method has proven capable of measuring grain boundary diffusivities with a high degree of consistency.
- This method is also highly sensitive to grain boundary diffusion at low temperatures. Therefore it enabled, for the first time, a study of structural effects in the type-C kinetics regime.
- It significantly improved the reliability of grain boundary diffusivity measurements by eliminating possible chemical effects due to segregation and DIGM, and by allowing direct examination of the grain boundary quality.
- Finally, this method also allows repeated usage of each diffusion specimen, and therefore permitted a comprehensive study of a series of 16 different grain boundary structures over a considerable range of temperatures.

6.2 Structural Effects

- Grain boundary diffusivities determined for a series of boundaries including low-Σ boundaries as well as more general boundaries showed a monotonic relationship between the grain boundary diffusion parameter $\delta_b D_b$ and the tilt angle θ, which could be successfully described by the SU model.

- The temperature dependence of the measured grain boundary diffusivities gave well defined activation energies of $\sim 0.7-0.85$ eV, which were smaller than the average value of ~ 1.0 eV, obtained at high temperatures in previous studies.
- Correspondingly, the measured pre-exponential factors were ~ 3 orders of magnitude smaller than those obtained at high temperatures.
- The smooth variation of activation energy as a function of θ implies that the distortion of structural units in the grain boundary core with respect to θ is gradual and relatively small.
- Low-Σ boundaries did not exhibit special diffusion properties such as cusped minima. This indicates that the elastic strain field of secondary dislocations, which produces the cusps on grain boundary energy versus misorientation angle curves, has no evident effect on grain boundary diffusion, and thus its effect on the structural units is weak.
- It was also suggested that previous observations of deep cusps in $s_b \delta_b D_b$ curves at low-Σ misorientations for chemical diffusion may have been due to grain boundary segregation or DIGM effects.
- Calculated results showed that for both vacancy and interstitialcy mechanisms, the low activation energy atomic jumping paths were within the structural units B or D as predicted by the SU model. Further, for the interstitialcy mechanism, the same type of jumping paths were responsible for the fast diffusion for all boundaries calculated, which revealed the spirit of the SU model at the atomic level.

6.3 Diffusion Mechanism and Kinetics

- In all of the four representative grain boundaries investigated by computer simulation, the activation energies for the interstitialcy mechanism were found to be considerably lower than those for the vacancy mechanism. Therefore, the interstitialcy mechanism is believed to dominate the grain boundary diffusion in [001] tilt boundaries at low temperatures.

- The calculated activation energies for interstitialcy mechanism were in very good agreement with those measured for 3 of the 4 boundaries. This agreement further strengthens the conclusion that the interstitialcy mechanism is responsible for the measured fast diffusion.

- Studies of correlated walks by computer simulation in both idealized and realistic grain boundaries revealed that there exist several possible confinements for a correlated grain boundary walk:

  1. If a boundary consists of a slab of three identical atomic layers, the correlation factor for diffusion along the boundary will be close to that in the corresponding three-dimensional lattice. If all of the jumps in only one of the atomic layers in the slab have uniformly lower activation energies, the correlated walk will have the characteristics of the corresponding two-dimensional lattice, especially at low temperatures.

  2. If a boundary consists of a set of separate coupled atomic jumping paths with relatively low activation energy, the characteristics of the correlated walk along the paths will be similar to that of the two-dimensional lattice with the correlation factor reduced by about a factor of 2.

  3. If a boundary consists of a set of individually isolated low energy atomic jumping paths, the correlation factor approaches 0 (characteristic of a one-dimensional lattice) as the temperature decreases. This temperature dependence is approximately associated with an energy which is the activation energy difference between the isolated path and the coupled next

lowest energy path. As a result, the grain boundary diffusivity has a characteristic activation energy corresponding to the coupled next lowest energy path.

- The above results indicate that the correlation factor for grain boundary diffusion depends on not only the diffusion mechanism but also the detailed grain boundary structure. As a result, it is insufficient to use the measured grain boundary correlation factor alone to determine the grain boundary diffusion mechanism.
- Excellent agreement was found between the measured $\delta_b D_b^0$'s and the estimates from simple kinetic theory for both the general magnitude and the trend of the structural dependence. The results also suggest that the effective grain boundary width for grain boundary diffusion at low temperatures is close to the average interatomic distance.
- It was suggested that the overall upward curvature of the Arrhenius diagram over a wide temperature range for grain boundary diffusivities was due to anharmonicity and multiple defect mechanisms which became increasingly important as the temperature was raised.

Bibliography

[1] I. Kaur and W. Gust. *Fundamentals of Grain and Interphase Boundary Diffusion.* Ziegler Press, Stuttgart, West Germany, 2nd edition, 1989.

[2] R.W. Balluffi and A. Brokman. Simple structural unit model for core-dependent properties of symmetrical tilt boundaries. *Scripta Met.*, 17:1027–1030, 1983.

[3] A.P. Sutton and V. Vitek. On the structure of tilt grain boundaries in cubic metals. I. Symmetrical tilt boundaries. *Phil. Trans. Roy. Soc. London*, A309:1–36, March 1983.

[4] A.P. Sutton and V. Vitek. On the structure of tilt grain boundaries in cubic metals. II. Asymmetrical tilt boundaries. *Phil. Trans. Roy. Soc. London*, A309:37–54, March 1983.

[5] A.P. Sutton and V. Vitek. On the structure of tilt grain boundaries in cubic metals. III. Generalizations of the structural study and implications for the properties of grain boundaries. *Phil. Trans. Roy. Soc. London*, A309:55–68, March 1983.

[6] A.N. Aleshin, B.S. Bokshtein, and L.S. Shvindlerman. Diffusion of zinc along [100] tilt boundaries in aluminium. *Sov. Phys. Solid State*, 19(12):2051–2054, December 1977.

[7] A.N. Aleshin, S.I. Prokofjev, and L.S. Shvindlerman. Diffusion parameters, grain boundary structure and diffusion mechanism in the vicinity of the $\Sigma 5$ coincidence misorientation in copper. *Defect and Diffusion Forum*, 66-69:861–868, 1989.

[8] R.W. Balluffi. Grain boundary structure and segregation. In W.C. Johnson and J.M. Blakely, editors, *Interfacial Segregation*, Metals Park, 1979. ASM.

[9] R.W. Balluffi, T.Kwok, P.D. Bristowe, A. Brokman, P.S. Ho, and S. Yip. Determination of vacancy mechanism for grain boundary self-diffusion by computer simulation. *Scripta Met.*, 15:951, 1981.

[10] T. Kwok, P.S. Ho, S. Yip, R.W. Balluffi, P.D. Bristowe, and A. Brokman. Evidence for vacancy mechanism in grain boundary diffusion in bcc iron: A molecular-dynamics study. *Phys. Rev. Lett.*, 47:1148–51, 1981.

[11] A. Brokman and R.W. Balluffi. Coincidence lattice model for the structure and energy of grain boundaries. *Acta Metall.*, 29:1703–1719, 1981.

[12] R.W. Balluffi, A. Brokman, and A.H. King. CSL/DSC lattice model for general crystal–crystal boundaries and their line defects. *Acta Metall.*, 30:1453–1470, 1982.

[13] R.W. Balluffi and P.D. Bristowe. On the structural unit/grain boundary dislocation model for grain boundary structure. *Surf. Sci.*, 144:28–43, 1984.

[14] W.A. Bollmann. *Crystal defects and crystalline interfaces.* Springer-Verlag, Berlin, New York, 1970.

[15] A. Otsuki and M. Mizuno. Proc. Symp. on Grain Boundary Structure and Related Phenomena. *Trans. Japan Inst. Metals, Suppl.*, 27:789, 1986.

[16] S.W. Chan and R. W. Balluffi. Study of energy versus misorientation for grain boundaries in gold by crystallite rotation method. II. Tilt boundaries and mixed boundaries. *Acta Metall.*, 34:2191, 1986.

[17] G.C. Hasson and C. Goux. Interfacial energies of tilt boundaries in aluminium. Experimental and theoretical determination. *Scripta. Metall.*, 5:889–894, 1971.

[18] D. Wolf. Structure-energy correlation for grain boundaries in FCC metals. III. symmetrical tilt boundaries. *Acta Metall.*, 38(5):781–790, 1990.

[19] J.P. Hirth and J. Lothe. *Theory of Dislocations.* John Wiley & Sons Ltd., 2nd edition, 1982.

[20] J.C. Fisher. Calculation of diffusion penetration curves for surface and grain boundary diffusion. *J. Appl. Phys.*, 22(1):74, Jan. 1951.

[21] L.G. Harrison. Influence of dislocations on diffusion kinetics in solids with particular reference to alkali halides. *Trans. Faraday Soc.*, 57:1191–1199, 1961.

[22] R.T.P. Whipple. Concentration contours in grain boundary diffusion. *Phil. Mag.*, 45:1225, 1954.

[23] T. Suzuoka. Lattice and grain boundary diffusion in polycrystals. *Trans. Jap. Inst. Metals*, 2(1):25–33, Jan. 1961.

[24] T. Suzuoka. *J. Phys. Soc. Japan*, 19:839, 1964.

[25] J.C.M. Hwang and R.W. Balluffi. Measurement of grain-boundary diffusion at low temperatures by the surface-accumulation method. I. Method and analysis. *J. Appl. Phys.*, 50(3):1339–1348, 1979.

[26] P.H. Holloway and G.E. McGuire. *J. Electrochem. Soc.*, 125:2070, 1978.

[27] R.W. Balluffi. Grain boundary diffusion mechanisms in metals. *Met. Trans.*, 13B:527–553, December 1982.

[28] G. Martin, D.A. Blackburn, and Y. Adda. Autodiffusion au joint de grains de bicristaux d'argent soumis a une pression hydrostatique. *Phys. Stat. Solidi.*, 23:223–228, 1967.

[29] G. Erdelyi, W. Lojkowski, D.L. Beke, I. Godeny, and F.J. Kedves. The pressure dependence of grain-boundary diffusion of ^{65}Zn in polycrystalline aluminium. *Phil. Mag. A*, 56(5):673–680, 1987.

[30] J.T. Robinson and N.L. Peterson. Correlation effects in grain boundary diffusion. *Surf. Sci.*, 31:586–616, 1972.

[31] A. Brokman, P.D. Bristowe, and R.W. Balluffi. Computer simulation study of the structure of vacancies in grain boundaries. *J. Appl. Phys.*, 52:6116, 1981.

[32] B.S. Bokshtein, I.A. Magidson, and I.L. Svetlov. On diffusion in volume and along grain boundaries. *Phys. Met. Metallogr.*, 6(6):81–95, 1958.

[33] F.J.A. Den Broeder. Interface reaction and a special form of grain boundary diffusion in the Cr-W system. *Acta Metall.*, 20:319–332, March 1972.

[34] A.H. King. Diffusion induced grain boundary migration. *Int. Mat. Rev.*, 32(4):173–189, 1987.

[35] D. Turnbull and R.E. Hoffman. The effect of relative crystal and boundary orientations on grain goundary diffusion rates. *Acta. Metall.*, 2:419–426, May 1954.

[36] S. Yukawa and M.J. Sinnott. Grain boundary diffusion of nickel into copper. *Trans. Am. Inst. Min. Metall. Pet. Eng.*, 203:996–1002, Sept. 1955.

[37] W.R. Upthegrove and M.J. Sinnott. Grain boundary self-diffusion of nickel. *Trans. Am. Soc. Met.*, 50:1031–1046, 1958.

[38] R.F. Canon and J.P. Stark. Analysis of penetration data from grain boundary diffusion experiments. *J. Appl. Phys.*, 40(11):4361, Oct. 1969.

[39] R.E. Hoffman. Anisotropy of grain boundary self-diffusion. *Acta Metall.*, 4:97–98, 1956.

[40] I. Herbeuval and M. Biscondi. Diffusion du zinc dans les joints de flexion symetrigues de l'aluminium. *Canad. Met. Quart.*, 13:171–175, 1974.

[41] J. Sommer, Chr. Herzig, S. Mayer, and W. Gust. Grain boundary self-diffusion in silver bicrystals. *Defect and Diffusion Forum*, 66-69:843–848, 1989.

[42] B.B. Straumal, L.M. Klinger, and L.S. Shvindlerman. The effect of crystallographic parameters of interphase boundaries on their surface tension and parameters of the boundary diffusion. *Acta Metall.*, 32(9):1355–1364, 1984.

[43] I. Kaur, W. Gust, and L. Kozma. *Handbook of Grain and Interphase Boundary Diffusion Data*, volume 1. Ziegler Press, Stuttgart, West Germany, 1989.

[44] I. Kaur, W. Gust, and L. Kozma. *Handbook of Grain and Interphase Boundary Diffusion Data*, volume 2. Ziegler Press, Stuttgart, West Germany, 1989.

[45] J.C.M. Hwang, J.D. Pan, and R.W. Balluffi. Measurement of grain-boundary diffusion at low temperatures by the surface-accumulation method. II. Results for gold-silver system. *J. Appl. Phys.*, 50(3):1349–1359, March 1979.

[46] C.A. Counterman. *Calculations of the Effects of Solute Segregation on Grain Boundary Structure and X-Ray Structure Factors in Gold Alloys.* PhD thesis, M.I.T., June 1991.

[47] S.M. Foiles. Calculation of the surface segregation of Ni-Cu alloys with the use of the embedded-atom method. *Physical Review B*, 32(12):7685–7693, 15 December 1985.

[48] J.W. Cahn. The kinetics of cellular segregation reactions. *Acta metall.*, 7(12):18–28, Jan. 1959.

[49] J.D. Pan and R.W. Balluffi. Diffusion induced grain boundary migration in Au/Cu and Au/Ag thin films. *Acta Metall.*, 30:861, 1982.

[50] T. Schober and R.W. Balluffi. Quantitative observation of misfit dislocation arrays in low and high angle twist grain boundaries. *Phil. Mag.*, 21:109–126, 1970.

[51] KTI Chem. Inc. *KTI-825 Positive Resist Processing*, 1988.

[52] H.I. Smith. Ion beam etching. In *Etching for Pattern Definition.* The Electochemical Society, 1976.

[53] Physical Electronics Industries Inc. *Handbook of Auger Electron Spectroscopy.* 1976.

[54] P.W. Palmberg and T.N. Rhodin. Auger electron spectroscopy of fcc metal surfaces. *J. Appl. Phys.*, 39(5):2425–2432, April 1968.

[55] S.H. Overbury and G.A. Somorjai. The surface composition of the silver-gold system by Auger electron spectroscopy. *Surf. Sci.*, 55:209–226, 1976.

[56] K. Meinel, M. Klaua, CH. Ammer, and H. Bethge. AES investigations on low-temperature interdiffusion in thin Au films on Ag (111) substrates. *Phys. Stat. Sol. (a)*, 106:493–507, 1988.

[57] D. Briggs and M.P. Seah. *Practical Surface Analysis by Auger and X-ray Photoelecton Spectroscopy.* John Wiley & Sons Ltd., 1984.

[58] V.T. Borisov, V.M. Golikov, and G.V. Scherbedinsky. Relation between diffusion coefficients and grain boundary energy. *Fiz. Met. Metall.*, 17(6):881–885, 1964.

[59] R.E. Howard. Random-walk method for calculating correlation factors: tracer diffusion by divacancy and impurity-vacacy pairs in cubic crystals. *Phys. Rev.*, 144(2):650–661, April 1966.

[60] J.T. Robinson and N.L. Peterson. Calculation of correlation effects for grain-boundary and dislocation-pipe self-diffusion. *Acta metall.*, 21:1181–1187, August 1973.

[61] J.R. Manning and J.P. Stark. Complete-path matrix equations for tracer diffusion coefficients and correlation factors. *Phys. Rev. B*, 12(6):2075–2079, Sept. 1975.

[62] J.P. Stark. Correlation factor for diffusion in an edge dislocation in a simple cubic crystal. *J. Appl. Phys.*, 57(6):1869–1871, March 1985.

[63] G. Clark and J.P. Stark. Isotope separation during diffusion along an edge dislocation in a simple cubic crystal. *J. Appl. Phys.*, 61(1):438–439, Jan. 1987.

[64] J.P. Stark, D.Y. Lee, and Leslie Vaughn. Diffusion in three different dislocations in an fcc crystal. *J. Appl. Phys.*, 64(9):4491–4493, Nov. 1988.

[65] C. Zener. Theory of D_0 for atomic diffusion in metals. *J. Appl. Phys.*, 22(4):372-375, April 1951.

[66] M.S. Daw and M.I. Baskes. Semiempirical, quantum mechanical calculation of hydrogen embrittlement in metals. *Phys. Rev. Lett.*, 50(17):1285–1288, 25 April 1983.

[67] M.S. Daw and M.I. Baskes. Embedded-atom method: Derivation and application to impurities, surfaces, and other defects in metals. *Phys. Rev. B*, 29(12):6443-6453, 15 June 1984.

[68] J.B. Adams, S.M. Foiles, and W.G. Wolfer. Self-diffusion and impurity diffusion of fcc metals using the five-frequency model and the embedded atom method. *J. Mat. Res.*, 4(1):102, Jan./Feb. 1989.

[69] S.M. Foiles, M.I. Baskes, and M.S. Daw. Embedded-atom-method functions for the fcc metals Cu, Ag, Au, Ni, Pd, Pt, and their alloys. *Phys. Rev. B*, 33(12):7983–7991, June 1986.

[70] S.M. Foiles, M.I. Baskes, and M.S. Daw. Erratum: Embedded-atom-method functions for the fcc metals Cu, Ag, Au, Ni, Pd, Pt, and their alloys. *Phys. Rev. B*, 37(17):10378, 15 June 1988.

[71] R. Fletcher and C.M. Reeves. Function minimization by conjugate gradients. *Computer Journal*, 7(2):149–154, July 1964.

[72] J.E. Sinclair and R. Fletcher. A new method of saddle-point location for the calculation of defect migration energies. *J. Phys. C*, 7(5):864–870, 7 March 1974.

[73] S.M. Foiles. Calculation of the atomic structure of the $\Sigma = 13(\theta = 22.6°)[001]$ twist boundary in gold. *Acta Metall.*, 37(10):2815–2821, 1989.

[74] G.J. Wang, A.P. Sutton, and V. Vitek. A computer simulation study of [001] and [111] tilt boundaries: The multiplicity of structures. *Acta Metall.*, 32(7):1093-1104, 1984.

[75] D.G. Brandon, B. Ralph, S. Ranganathan, and M.S. Wald. A field ion microscope study of atomic configuration at grain boundaries. *Acta Metall.*, 12:813–821, July 1964.

[76] R. Gronsky. Direct imaging of grain boundaries. In R.W. Balluffi, editor, *Grain Boundary Structure and Kinetics*, page 45. American Society for Metals, 1980.

[77] S.L. Sass and P.D. Bristow. Diffraction studies of the atomic structure of grain boundaries. In R.W. Balluffi, editor, *Grain Boundary Structure and Kinetics*, page 71. American Society for Metals, 1980.

[78] A. Atkinson and R.I. Taylor. The diffusion of ^{63}Ni along grain boundaries in nickel oxide. *Phil. Mag. A*, 43(4):979–998, 1981.

[79] A. Moosa, S.J. Rothman, and L.J. Nowicki. *Oxid. Met.*, 24:115, 1985.

[80] H.M. Gilder and D. Lazarus. Role of vacancy anharmonicity on non-Arrhenius diffusional behavior. *Phys. Rev. B*, 11(12):4916–4926, 1975.

[81] R.P. Sahu, K.C. Jain, and R.W. Siegel. Vacancy properties in gold. *J. Nuclear Mat.*, 69 & 70:264–276, 1978.

[82] N.L. Peterson. Self-diffusion in pure metals. *J. Nuclear Mat.*, 69 & 70:3–37, 1978.

[83] G.E. Rhead. On surface diffusion and the existence of "two-dimensional" liquids. *Surf. Sci.*, 15:353–357, 1969.

[84] Vu Thien Binh and P. Melinon. On viscous mechanism for surface diffusion at high temperatures ($T/T_m > 0.75$) due to formation of a 2D dense fluid on metallic surfaces. *Surf. Sci.*, 161:234–244, 1985.

[85] T.E. Hsieh and R.W. Balluffi. Experimental study of grain boundary melting in aluminum. *Acta Metall.*, 37:1637, 1989.